

TECHNISCHE UNIVERSITÄT MÜNCHEN
FAKULTÄT FÜR PHYSIK

**Anti-Ferromagnetic Coupling of
Anti-Phase Domains**

Ulrike Zweck

Vollständiger Abdruck der von der Fakultät für Physik der Technischen Universität
München zur Erlangung des akademischen Grades einer

Doktorin der Naturwissenschaften (Dr. rer. nat.)

genehmigten Dissertation.

Vorsitzender: Prof. Dr. Frank Pollmann

Prüfer der Dissertation:

1. Prof. Dr. Winfried Petry
2. Prof. Dr. Rudolf Gross

.....

Die Dissertation wurde am 18.05.2022 bei der Technischen Universität München ein-
gereicht und durch die Fakultät für Physik am 04.07.2022 angenommen.

I confirm that this thesis is my own work and I have documented all sources and material used.

Garching b. München, 18.05.2022

Signature

To my mother, Silvia

Abstract

In Ni_2MnZ Heusler compounds, the atomic order of the austenite phase influences a variety of material properties, as for example the magnetic properties and martensitic transformations. Accessing the full potential of these materials requires a comprehensive understanding of the interdependence of the structural order and magnetic properties.

This thesis deals with the correlation of the atomic microstructure and the magnetic properties of Ni_2MnZ Heusler alloys by applying neutron diffraction techniques. The interpretation of the experimental observations is supported by theoretical models and computer simulations. Specifically, the coarsening process of anti-phase domains in order-disorder transitions is investigated via Monte-Carlo simulations. A general model describing the real-space correlation function and the reciprocal-space structure factor is developed. Further, the size of the structural L_{21} ordered domains is examined in $\text{Ni}_2\text{MnAl}_{0.5}\text{Ga}_{0.5}$ and Ni_2MnAl alloys via neutron powder diffraction measurements. The obtained structural domain size is found to be identical with the size of the magnetic domains, which is investigated via small-angle neutron scattering measurements. These observations indicate the atomic domain configuration to coincide with the magnetic domain configuration. Finally, the coupling between these magnetic domains is studied as a function of temperature and magnetic field strength via small-angle neutron scattering measurements under external magnetic fields. Here, a behaviour similar to a Heisenberg anti-ferromagnet is observed, demonstrating the magnetic domains to couple anti-ferromagnetically.

Zusammenfassung

Die atomare Ordnung der Austenit Phase in Ni_2MnZ Heusler Legierungen beeinflusst eine Vielfalt an Materialeigenschaften, wie beispielsweise die magnetischen Eigenschaften und die martensitische Transformation. Ein umfassendes Verständnis der wechselseitigen Abhängigkeit der strukturellen Ordnung und der magnetischen Eigenschaften ist der Schlüssel um das volle Potential dieser Materialien nutzen zu können.

In dieser Arbeit wird die Korrelation der strukturellen Mikrostruktur und den magnetischen Eigenschaften in Ni_2MnZ Heusler Legierungen experimentell mit Neutronendiffraktionsmessungen untersucht. Die Interpretation der experimentell beobachteten Ergebnissen wird durch theoretische Überlegungen und Computersimulationen gestützt. Im Speziellen wird der Vergrößerungsprozess von Antiphasendomänen, die sich während eines strukturellen Ordnungsüberganges bilden, mittels Monte-Carlo Simulationen untersucht und ein allgemeines Modell zur Beschreibung der Paarkorrelationsfunktion im Realraum und des entsprechenden Strukturfaktor im Reziprokraum entwickelt. Die Größe der Antiphasendomänen, die eine $L2_1$ Ordnung aufweisen, wird in $\text{Ni}_2\text{MnAl}_{0.5}\text{Ga}_{0.5}$ und Ni_2MnAl Verbindungen mittels Neutronenpulverdiffraktion untersucht und mit den magnetischen Domänen, die durch Neutronenkleinwinkelstreuung erforscht werden, verglichen. Hierbei wird beobachtet, dass beide Skalen ähnlich groß sind, was auf ein Zusammenfallen der atomaren und magnetischen Mikrostruktur hinweist. Abschließend werden Kleinwinkelmessungen mit einem externen magnetischen Feld vorgestellt, mittels derer die magnetische Kopplung der magnetischen Domänen als Funktion der Temperatur und der magnetischen Feldstärke erforscht wird. Es wird ein Verhalten ähnlich zu einem Heisenberg Antiferromagneten beobachtet, was zeigt, dass die magnetischen Domänen antiferromagnetisch zueinander koppeln.

Acknowledgements

First and foremost, I would like to thank Prof. Dr. Winfried Petry for the opportunity to work on this fascinating topic and for motivating me throughout my thesis. I am especially grateful to my advisor, Dr. Michael Leitner, for his scientific input and constant assistance. I learnt a lot from you in these past years, physics, programming, life and am grateful that I had this opportunity.

I also want to thank my mentor Dr. Thomas Böhm for giving me a new perspective to my programming problems as well as proof-reading all my first drafts.

I am particularly grateful for the assistance given by Sebastian Mühlbauer concerning measurements at SANS-1 and Bob Cubitt and Michel Bonnaud for their support during the beam time at ILL.

I would like to thank the NEPOMUC group, for taking me in, all the fruitful discussions, the well-needed coffee breaks and Laborbesprechungen as well as memorable hiking trips. I am particularly thankful to all my proof-readers Vassily Burwitz, Lucian Mathes and Josef Ketels.

I also want to thank all my friends who studied alongside me and without whom my studies would have been only half as fun. Especially Wolfgang Enzi, for letting me use his Grammarly as well as proof-reading various parts of my thesis, and Martina Karl for all the hot chocolate breaks and handing in all her theses at the same time with me.

My gratitude to my family goes way beyond and before this thesis, for being the support I needed, for never feeling alone, for letting me being me and loving me despite of it.

Last I want to thank Mario Zweck for being there when I needed you, especially during the last year. Thanks to you I never lost hope and got through this!

Acknowledgements

Contents

1	Acronyms and Glossary	1
2	Motivation	5
3	Modeling the Coarsening Process of Anti-Phase Domains	9
3.1	Introduction	9
3.2	Systems	12
3.2.1	Microscopic Models	12
3.2.2	Abstract Models: q -State Potts Model	15
3.2.3	Implementation and Dynamics	15
3.2.4	Equilibrium Properties	17
3.3	Domain Coarsening	20
3.3.1	Simulation Temperature and Exchange Interaction	21
3.3.2	Dynamical Scaling	25
3.4	The Scaling Function	28
3.4.1	Phenomenological Ansatz	28
3.4.2	Fitting the Scaling Function	30
3.5	Growth of the Anti-Phase Domains	34
3.5.1	Kinetics	34
3.5.2	Temperature Dependence	36
3.5.3	Measures of Domain Size	38
3.6	Conclusion	40
4	Correlation of Structural and Magnetic Domains	43
4.1	Influence of Structural Order on the Magnetic Properties of Ni_2MnZ Heusler Alloys	43
4.2	Sample Preparation	46
4.3	Neutron Powder Diffraction	49

4.3.1	The Time-of-Flight Spectrometer POWGEN	49
4.3.2	Neutron Scattering Theory	51
4.3.3	Intensity in Time-of-Flight Neutron Powder Diffractometers .	56
4.3.4	Determination of the Structural Domain Size	58
4.4	Small-Angle Neutron Scattering	64
4.4.1	Neutron Scattering of Large Structures	65
4.4.2	Magnetic Domains in Ni_2MnZ Compounds	66
4.5	Conclusion	75
5	Anti-Ferromagnetic Coupling of Anti-Phase Domains	77
5.1	Introduction	77
5.2	Isothermal Measurements Under High Magnetic Fields	81
5.3	Temperature-Dependent Measurements	87
5.4	Conclusion	94
6	Summary	95
A	Considerations of the IRF for TOF Powder Diffractometers	97
B	Calibration of the SANS Signal	103

Chapter 1

Acronyms and Glossary

Anti-phase domain (APD)	Domains of the same ordered phase form during an ordering transition in compounds, where the lattice of a priori equivalent sites decays into sublattices with preferred occupations by different elements. As the superstructures nucleate at independent regions in the crystal, they do not necessarily fit together.
Anti-phase domain boundary (APB)	An interface between two domains of the same ordered phase.
\bar{D}	The real-space scale of an anti-phase domain (APD) determined from the diffraction-peak's width Δk via the Scherrer equation
Degeneracy	An energy level is degenerate if there are two or more states which give the same energy value.
Differential Scanning Calorimetry (DSC)	A measurement technique which determines the specific heat of a sample undergoing a physical or chemical change.
Energy-Dispersive X-Ray Spectroscopy (EDS)	An analytical technique to identify and quantify elemental compositions in any given material.

Full-Width at Half Maximum (FWHM)	The width of a spectrum curve at half of its maximum amplitude.
Heusler Compound (X_2YZ)	An intermetallic compound, where X and Y are transition metals and Z is a main group element. Its prototypical crystal structure is $L2_1$ order at room temperature.
Instrumental Resolution Function (IRF)	A function describing the peak shape of a spectrum curve measured at a diffraction instrument. Its parameters are determined from the calibration measurements.
k	In Chap. 3 it is defined as an independent variable in the Fourier transformed space. In Chap. 4 and Chap. 5 k denotes the wavevector of a particle or wave.
κ	The reduced element in Fourier space, which is defined in Chap. 3 as a function of k in Eq. (3.13).
Microscopic Model	This model is used to describe the ordering process in binary alloys in which the order parameter is conserved. The spin states σ are either -1 or 1 . The ground state of the investigated systems is degenerate with multiplicity q depending on the symmetry of the system. Hence during the ordering process q anti-phase domains are present in the system with a perfectly ordered state corresponding to a configuration of unlike nearest neighbour pairs.

q, Q

In Chap. 3 q denotes the multiplicity of a degenerate ground state. In the ferromagnetic q -state Potts model it is the number of possible spin states, while for the microscopic model it corresponds to the number of anti-phase domains present in the system. In Chap. 4 and Chap. 5 Q denotes the wavevector transfer of a particle or wave in a scattering event.

q -state Potts Model

This model is used to describe ferromagnetic domains in which the order parameter is not conserved. q is the number of possible spin states σ present in the system with ($q \in \{2, 3, 4, \dots\}$) and $\sigma \in \{0, 1, \dots, (q - 1)\}$. A perfectly ordered state would correspond to only one spin state being present in the system.

Pair-Correlation Function
 $g'(r)$

In an ordering transition with q anti-phase domains present $g'(r)$ denotes the radially averaged real-space pair-correlation function of the ordered domains. It decays from 1 at small distances to $1/q$ at infinity.

Rescaled Pair-Correlation Function $g(r)$

The rescaled radially averaged real-space pair-correlation function of anti-phase domains decays from 1 at small distances to 0 at infinity. It is given as $g(r) = (qg'(r) - 1)/(q - 1)$.

Spatially Scaled Pair-Correlation Function
 $g(\rho)$

The rescaled radially averaged real-space pair-correlation function of structurally ordered domains is scaled by the time-dependent scaling factor $L(t)$. With $\tilde{L}(t) = L(t)(q - 1)/q$ the spatially scaled pair-correlation function is given as $g(\rho) = g(r/\tilde{L}(t))$. It takes values from 1 at small distances to 0 at infinity.

\mathbf{r}	The distance between two atoms or positions in real space.
ρ	The reduced distance in real space given as a transformed function of \mathbf{r} in Eq. (3.12).
Small-Angle Neutron Scattering (SANS)	An experimental technique which measures the coherent scattering and is sensitive to structures of the mesoscopic length scale. Due to the neutron's magnetic moment, which couples to the local internal magnetic field from the magnetic atoms in the sample, the contrast between local magnetic fields can be probed and the corresponding magnetic microstructure can be investigated via SANS experiments.
Structure Factor $S(k)$	The radially averaged reciprocal-space structure factor which corresponds to the three dimensional Fourier transform of the pair-correlation function $g(r)$.
Spatially Scaled Structure Factor $S(\kappa)$	The spatially scaled structure factor with $S(\kappa) = S(k\tilde{L}(t))/\tilde{L}(t)^3$. The factor $1/\tilde{L}(t)^3$ is due to $S(\kappa)$ being the three-dimensional Fourier transform of $g(\rho)$.
Time-of-Flight Diffractometer (TOF)	An experimental technique which measures the scattering intensity as a function of time a neutron takes to travel from its source to the detector.

Chapter 2

Motivation

Heusler alloys have attracted a considerable amount of attention due to their fascinating functional properties such as thermoelectricity (Sakurada and Shutoh, 2005), superconductivity (Wernick et al., 1983), the magneto-caloric effect (Hu, Shen, and Sun, 2000; Planes, Mañosa, and Acet, 2009) as well as the ferromagnetic shape memory effect (Ullakko et al., 1996; Murray et al., 2000). Heusler compounds are defined as intermetallic XYZ (half-Heusler) and X_2YZ (full-Heusler) compounds, where X and Y are transition metals and Z is a main group element. Friedrich Heusler (Heusler, 1903) discovered the principle Heusler compound (Cu_2MnAl), while studying the intermetallic compound Cu_2Mn . He observed that the addition of a main group element (Al, In, Sn, Sb or Bi) led to a ferromagnetic alloy, even though none of the constituents are ferromagnetic. Its crystal structure was studied using X-ray scattering by Bradley, Rodgers, and Bragg (1934), and was determined to be $L2_1$ order at room temperature, depicted in Fig. 2.1.

Upon the discovery of a new class of materials, the half-metallic ferromagnets, in the half-Heusler alloy $NiMnSb$ (Groot et al., 1983) and the observation of the ferromagnetic shape memory effect in the full-Heusler alloy Ni_2MnGa (Webster et al., 1984), $NiMn$ -based Heusler compounds have been the subject of tremendous experimental (Planes, Mañosa, and Acet, 2009; Neibecker et al., 2014; Umetsu, Xu, and Kainuma, 2016; Neibecker et al., 2017) as well as theoretical interest (Pierre et al., 1997; Miura, Nagao, and Shirai, 2004). Their functional properties show a strong dependence on structural order (Neibecker et al., 2017), thus understanding the relation between them is key to access the full potential of $NiMn$ -Heusler compounds. Typically these alloys undergo two phase ordering transitions when cooling from the melt to room temperature. For Ni_2MnAl the fully disordered body centred phase ($A2$ order) is

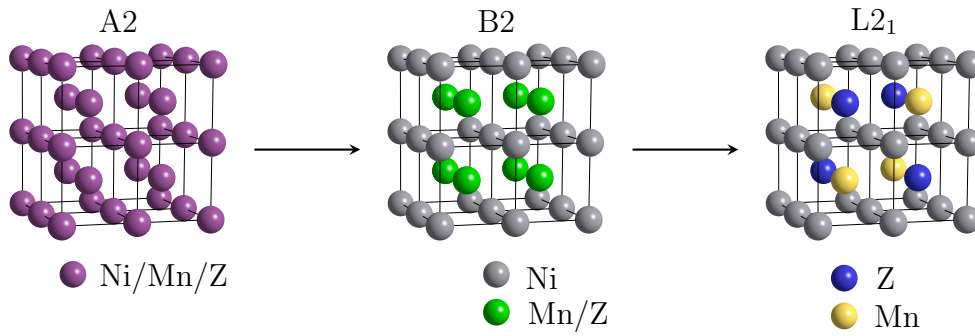


Figure 2.1: Schematic representations of the ordering states of Ni_2MnZ on the bcc lattice: In the A2 structure all atom species are distributed randomly over the lattice sites. B2 order can be described by two sc sublattices, with Ni atoms occupying one sublattice while Mn and Z atoms occupy in disorder the other one. In the L_{21} structure further ordering occurs on the later sublattice.

transformed into a partially ordered structure (B2 order) at 1220 K (Soltys, 1981). This CsCl type crystal structure is depicted in the middle of Fig. 2.1 and corresponds to two nested simple cubic (sc) lattices, with one being occupied by Ni atoms, while the other one is occupied by a random distribution of Mn and Al atoms. At 990 K (Soltys, 1981) the partially ordered phase undergoes further ordering on the Mn and Al sublattice and the full-Heusler structure (L_{21} order) is formed. This superstructure on the body-centred cubic (bcc) lattice can be described by four nested face-centred cubic (fcc) lattices, with each atom occupying one sublattice as depicted on the right in Fig. 2.1. The order-disorder transition from B2 to L_{21} order is a second-order phase transition and is accompanied by a reduction in the translational symmetry as well as a change in the magnetic properties of the material (Neibecker et al., 2014; Neibecker et al., 2017).

Spontaneous symmetry breaking associated with phase ordering in a compound has a great influence on structural as well as functional properties (Stoloff, 1984; Pollock and Tin, 2006; Neibecker et al., 2017), e.g. the yield strength or magnetism. The order-disorder transition results in a loss of symmetry with a superstructure being formed during the ordering process. The superstructure nucleates at independent regions in the crystal, which do not necessarily fit together. With time this ordered phase covers the whole crystal leading to a division of the crystal into so called APDs. The interface is correspondingly called anti-phase domain boundary (APB). During the transition these domains begin to coarsen in order to reduce the excess free energy of the domain walls. Due to the formation of the superstructure a unit dislocation in the disordered state becomes a partial dislocation in the superlattice which is attached to

the APB (Stoloff and Davies, 1968). Moving this so-called superdislocation requires very high stress, as it will destroy the order across its slip plane completely. Thereby the yield strength of a compound in its ordered state is increased compared to its disordered one (Vidoz, Lazarević, and Cahn, 1963). A prominent example for the influence of atomic order are superalloys such as Ni_3Al and Fe_3Al or the lightest intermetallic ordered compound Al_3Li . In their ordered state, a L1_2 superstructure on the fcc lattice, they display remarkable mechanical strength at a low density (Stoloff, 1984; Pollock and Tin, 2006). Describing the atomic ordering process as well as its kinetics accurately is crucial for understanding the relation between structural order and system properties.

Specifically, in the development of magnetic properties, structural order plays a crucial role, as for example, in most ferromagnetic materials, such as iron or nickel: While a well-ordered iron sample with a low defect concentration is a perfect example for a soft magnet, which can easily be magnetized and demagnetized, the same sample can become a hard magnet when being heavily deformed. This change of the magnetic properties is due to the pinning of the magnetic domains at local defects in the sample, which leads to an increase of its coercivity with an increasing degree of disorder. In Ni_2MnZ Heusler compounds, the atomic order of the austenite phase plays a crucial role in their magnetic properties. As is the case for many other compounds with a sufficiently high concentration of Mn (Acet et al., 2002; Kwiatkowski et al., 2007), the magnetic moments are mainly carried by the Mn atoms, whose exchange interaction depends strongly on the distance between them. To study this interplay of structural and magnetic order, we used neutron scattering. Via this method we can access not only the atomic microstructure of the sample, but due to the neutron's magnetic moment, which couples to the local internal magnetic field from the magnetic atoms in the sample, we can also investigate its magnetic microstructure.

The outline of this thesis is the following: In chapter 3 the coarsening of APDs in compounds is investigated via Monte-Carlo simulations. A detailed description of the general process is given as well as a derivation of a model to describe the real-space correlation functions. Chapter 4 reports on the scale of structural and magnetic domains using a combination of neutron powder diffraction and small angle neutron scattering. In chapter 5 the coupling of magnetic domains is investigated using small angle neutron scattering under magnetic fields as well as neutron powder diffraction at low temperatures.

Chapter 3

Modeling the Coarsening Process of Anti-Phase Domains

3.1 Introduction

The ordering process in binary alloys, which follows the quench from a disordered state, greatly influences system properties, such as magnetism or hardness. A prominent example of atomic order's influence on functional properties is superalloys such as Ni_3Al , Fe_3Al or the lightest intermetallic ordered compound Al_3Li . In their ordered state, an L_{12} superstructure on the fcc lattice, these alloys display remarkable mechanical strength at a low density (Stoloff, 1984; Pollock and Tin, 2006). In Heusler alloys, structural order is known to have a strong influence on the system properties, e.g. changing the electronic band structure (Graf, Felser, and Parkin, 2011) or increasing the magnetic transition temperature with increased chemical order (Neibecker et al., 2014). Specifically, the transition from B2 order to the full-Heusler structure (L_{21} order) is accompanied by a change in the magnetic properties for Ni_2MnZ compounds (Neibecker et al., 2014; Neibecker et al., 2017). To understand this strong relation between structural order and functional properties, it is crucial to describe the atomic ordering process and its kinetics accurately.

The order-disorder transition results in a loss of symmetry, where the lattice of a priori equivalent sites decays into sublattices with preferred occupations by different elements. This superstructure nucleates in independent regions of the crystal, where the ordered domains subsequently grow, leading to a division of the crystal in so-called APDs. An example for the two-fold degenerate ground state, an AB alloy

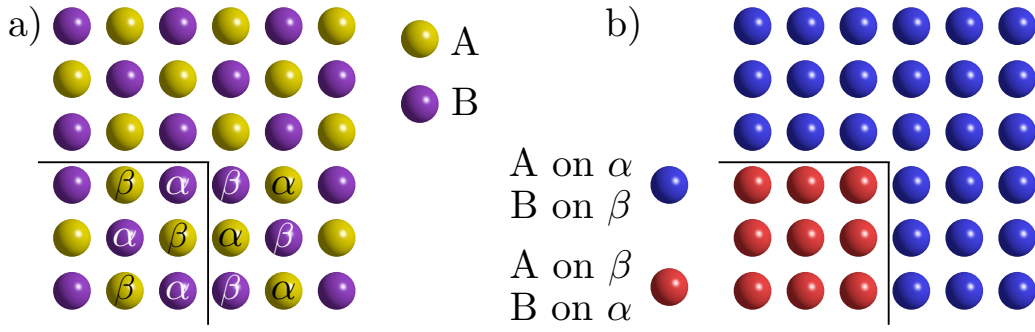


Figure 3.1: Atomic configuration with two anti-phase domains illustrated as a) ordered atoms and b) atoms assigned to domains, according to A and B occupying the α and β or β and α sublattice, respectively. The anti-phase domain boundary is sketched as a black line.

on a quadratic lattice, is sketched in Fig. 3.1. The atomic order of the crystal plane shows that both occupations (A on the α and B on the β sublattice and its respective complement) lead to an ordered structure. Assigning every site a domain according to the occupied sublattice of each atom kind leads to the domain configuration depicted in Fig. 3.1 b). The domains are separated by an APB, sketched as a black line in both pictures. As time goes on, the domains begin to coarsen, as they grow to minimize the area of the domain walls that separate the phases.

Experimentally the kinetics of an ordering transition is investigated by measuring the size of the APDs with annealing time either by real-space methods, e.g. electron microscopy, or via diffraction methods in reciprocal space. In microscopy the length scale of the APDs is commonly (Rogers, Flower, and Rawlings, 1975; Suzuki, Takeyama, and Matsuo, 2002; Brenker, Müller, and Brey, 2003) determined via the linear intercept method. Here the characteristic length scale of the APDs is defined as the mean distance between APD intersections on a line segment of random direction (Smith and Guttman, 1953).

In diffraction experiments, the finite correlation length of the superstructure, which is confined by the APD size, results in the broadening of the respective Bragg peaks. This broadening is best described by the full-width at half maximum (FWHM) or the integral breadth B_I which is defined as the quotient of the peak area to the peak height. In the easiest approach, the APD size is inversely proportional to the peak broadening $\bar{D} = 2\pi K / \Delta k$ (Scherrer, 1918). This relation is known as the Scherrer equation, where K is a phenomenological constant of the order of unity, the Scherrer constant, and Δk is a parameter to describe the broadening of the Bragg peak. In more elaborate analysis methods, the shape function is Fourier transformed, weighted with

the size distribution function and modelled to the powder pattern (Scardi and Leoni, 2002; Scardi and Leoni, 2005). In both evaluation methods, the shape of the domains has to be taken into account, either in the form of the Scherrer constant or the model for the whole powder pattern fit. Since APDs have no closed form, assumptions made about their shape will therefore always yield an insufficient description of their fundamental intrinsic properties. The determined length scale parameters are specific to the analysis method and the used assumptions. Specifically, length scales obtained via diffraction methods can commonly not be related to particular real-space features of APDs (Sakai and Mikkola, 1971; Morris, Besag, and Smallman, 1974; Morris et al., 1976).

In the absence of atomic disorder and discreteness, the evolution of the domain growth with coarsening time is deterministic and driven by its interface curvature according to the classical Allen-Cahn treatment (Allen and Cahn, 1979). In a late stage of the coarsening process, the statistical properties of a domain configuration $\sigma_1(r)$ are identical to the statistical properties of a domain configuration at an earlier ordering time $\sigma_2(r)$, when being scaled by a time-dependent spatial scaling factor $L(t)$. Hence, for time scales, where this scaling hypothesis (Bray, 2002) is valid, the domain structure is in a statistical sense independent of the coarsening time when being scaled by a single characteristic length scale $L(t)$. In the case of a curvature-driven coarsening process of non-conserved fields (Bray, 2002), the time-dependence of $L(t)$ can typically be described by a power-law dependence with an exponent of $\nu = 1/2$, $L(t) \propto t^{1/2}$.

There have been numerous attempts to give a general description of the statistical properties of the domain structure, such as the pair-correlation function $g(r)$ or the respective structure factor $S(k)$, within the scaling regime (Kawasaki, Yalabik, and Gunton, 1978; Ohta, Jasnow, and Kawasaki, 1982; Mazenko, 1990; Liu and Mazenko, 1991; Toyoki, 1992; Bray, 2002). Computer simulations prove to be an important tool to investigate this process in detail (Phani et al., 1980; Frontera, Vives, and Planes, 1994; Simak et al., 1998; Kessler, Dieterich, and Majhofer, 2003a).

Since for Ni_2MnZ compounds the development of their functional properties is strongly dependent on the structural order process, an accurate description of the coarsening process of the APDs as well as its kinetics is crucial to understand their strong relation. This chapter investigates the coarsening process of anti-phase domains via Monte-Carlo simulations. We consider three-dimensional systems with up to four inequivalent domains present during the order-disorder transition. Using

the abstract Potts as well as microscopically realistic models, we performed large-scale simulations of APD coarsening for in total of six systems. Finally, we give a phenomenological model to describe the statistical properties of atomic order configuration, such as the general form of the real-space pair-correlation function and the reciprocal-space structure factor. The results of this chapter were partially published in Zweck and Leitner (2021).

3.2 Systems

3.2.1 Microscopic Models

For the microscopic models, we consider the Hamiltonian given by

$$H = -J_{nn} \sum_{\langle i,j \rangle} \sigma_i \sigma_j - J_{nnn} \sum_{\langle i,j \rangle'} \sigma_i \sigma_j. \quad (3.1)$$

with $\sigma = \pm 1$ for A and B atoms, respectively. The summation over all nearest neighbour pairs of sites is denoted by $\langle i, j \rangle$, while the next-nearest neighbours are considered by $\langle i, j \rangle'$. Each pair is counted once. J_{nn} and J_{nnn} are the nearest neighbour and the next-nearest neighbour exchange interaction constants, respectively. Choosing the exchange interaction constant $J_{nn} = -1$ leads to a preference of a configuration of unlike nearest neighbour pairs.

For the ordering process on the sc lattice with an equal concentration of the two kinds of atoms we consider only the nearest neighbour exchange interactions, hence $J_{nnn} = 0$. This Hamiltonian compares to the standard three-dimensional nearest neighbour anti-ferromagnetic Ising model, which is thermodynamically equivalent to the ferromagnetic Ising model. The ground state of this system is degenerated with a multiplicity $q = 2$ and corresponds to B1 order (NaCl), which can be described by two nested fcc lattices, occupied by A and B atoms, respectively. It has the space group 225 ($Fm\bar{3}m$) with A and B atoms on the Wyckoff positions (4a) and (4b). Due to the symmetry of the system as well as the equal concentration of the two atom kinds, there are two APDs present in the system and hence there exists only one APB. The nearest neighbour bonds between the lattice sites across the APB give rise to a bipartite graph, as well as no segregation to the boundaries. Due to the simplicity of this system, it is arguably the most popular to study APD structures theoretically (Phani et al., 1980; Vetter and Baal, 1990). Note that considering the same Hamiltonian on a bcc lattice, the corresponding ground state is B2 order (also

known as the CsCl structure), which is qualitatively equivalent to the B1 case. Due to its applicability to the ordering process of intermetallic compounds such as FeAl or NiAl (Bradley, Jay, and Bragg, 1932; Bradley, Taylor, and Bragg, 1938), this case has been the subject of numerous experimental studies (Bradley, Jay, and Bragg, 1932; Allen and Cahn, 1975; Pochet et al., 1995).

We study the prototypical cases of a three and four-fold ground state degeneracy on the fcc lattice. Here we investigate the atomic ordering process of two binary alloys, AB_2 and AB_3 , of concentrations in accord with their stoichiometry. The four-fold degenerate ground state on an fcc lattice is an $L1_2$ ordered structure (Cu_3Au). It is assigned to the space group 221 ($Pm\bar{3}m$) with the minority atom kind A and the majority atom kind B atoms on the Wyckoff position (1a) and (3c), respectively. The ordered lattice can be described by four nested sc lattices, α , β , γ and δ , as shown in the top panel of Fig. 3.2. The respective $L1_2$ order ground states are depicted in the middle panel of Fig. 3.2. In contrast to the sc lattice, considering solely nn interactions leads on an fcc lattice to varying energy costs of an APB depending on the type of neighbouring domain. Any domain can form APBs parallel to the $\{100\}$ plane families to one of the remaining domains without any additional energy cost (Sakai and Mikkola, 1971). As a result, the APDs are faceted strongly in these directions up to the transition temperature (T_c). This observation agrees with the results from Monte Carlo simulations by Frontera et al. (1997) for the AB_3 alloy. An evaluation of the energy costs of APBs for different lattice structures is presented in section 3.3.1.1. Since the coarsening of domains is a curvature driven process, the domain growth is slowed down. Instead of the predicted (Allen and Cahn, 1979) and experimentally obtained (Nagler et al., 1988) growth exponent of $\nu \sim \frac{1}{2}$, an effective exponent of $\nu \sim \frac{1}{4}$ is observed by Frontera et al. (1997) and Kessler, Dieterich, and Majhofer (2003b). For the APDs to grow isotropically on the fcc lattice it is necessary to consider not only nearest but also next-nearest neighbour ($J_{nnn} \neq 0$) exchange interactions. We found that setting $J_{nnn} = 1$ results in a suppression of this behaviour with the configurations being practically isotropic, which agrees with Kessler, Dieterich, and Majhofer (2003a). Experimentally, the full range from strong (Sakai and Mikkola, 1971; Morris, Besag, and Smallman, 1974) to absent (Morris et al., 1976) anisotropies is evidenced, depending on the system.

Next, we consider the ordering of an AB_2 alloy on the faces of an $L1_2$ ordered structure. An example of this ordering process is the composition Cu_2NiZn (see Simak et al. (1998) and the references given therein). This alloy orders, when cooling it down from the melt, first in an $L1_2$ structure (Simak et al., 1998) with Ni and Cu atoms in disorder

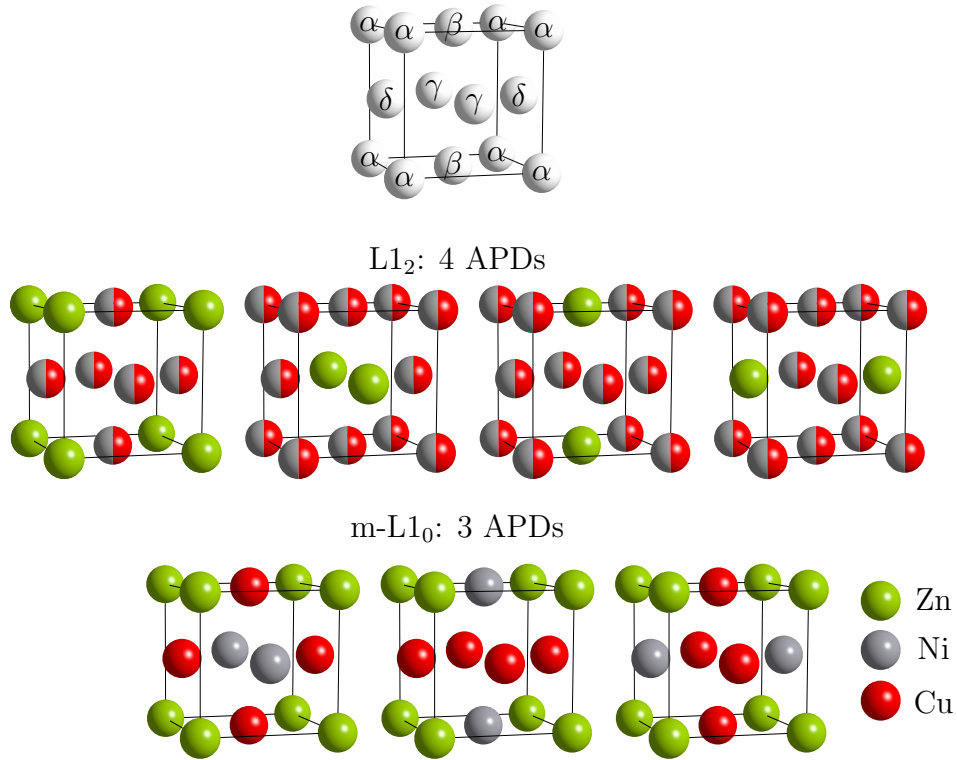


Figure 3.2: An fcc lattice with its four sc sublattices α , β , γ and δ . The two microscopic models as superstructures on the fcc lattice for the Cu_2NiZn compound: $L1_2$ (mid) and $m-L1_0$ (bottom). In $L1_2$ order the green minority atom can choose one of four sublattices, corresponding to a four-fold degenerate ground-state (4 APDs, $q = 4$). Further ordering on the three remaining sublattices, occupied by Cu and Ni, forms the $m-L1_0$ structure, which is a three-fold degenerate ground-state (3 APDs, $q = 3$).

on the faces of the fcc lattice, as shown in Fig. 3.2. Its structure undergoes further ordering on the Cu/Ni sublattices decreasing the temperature, with the Ni atoms congregating on one of the three sublattices. The resulting structure of tetragonal symmetry can equally be seen as a superstructure on $L1_0$. Thus it is denoted as “modified” $L1_0$ structure ($m-L1_0$), with its three equal ground state structures being illustrated in the bottom panel of Fig. 3.2. It has space group 123 ($P4/mmm$) with Zn on Wyckoff position (1a), Ni on (1c), and Cu on (2e). At this transition, the Zn atoms are unaffected, and in our model, we disregard the static Zn atoms. The situation for the anisotropy of the APD boundary energy is analogous to the $L1_2$ -case, and also here, we use $J_{\text{nnn}} = 1$ to get approximately isotropic interfacial energies.

3.2.2 Abstract Models: q -State Potts Model

In the standard q -state Potts model (Potts, 1952), with q being the number of possible spin states ($q \in (2, 3, 4, \dots)$), the Hamiltonian is given by

$$H = -J \sum_{\langle i,j \rangle} \delta_{\sigma_i, \sigma_j}, \quad (3.2)$$

where $J > 0$ is the exchange interaction constant, σ_i can be a value between 0 and $q - 1$ and $\delta_{\sigma_i, \sigma_j}$ corresponds to the Kronecker-Delta. Solely the nearest neighbour exchange interaction is considered. Generally, this model is used to study ferromagnetic domains in which the order parameter is not conserved. We performed simulations of the ordering process using this model by investigating the assignment of unit cells to q APDs, rather than the movement of atoms (as in microscopic models).

3.2.3 Implementation and Dynamics

We model the ordering process of the microscopic B1 and the Potts cases on cubic $N \times N \times N$ lattices. We consider $N/2 \times N/2 \times N/2$ four-site conventional cubic cells for the microscopic L1₂ and m-L1₀ instances since they are superstructures on the fcc lattice. In all cases, N is 1024 unless stated otherwise. Our algorithms use random numbers generated by a permuted congruential generator (PCG) (O'Neill, 2014). If not explicitly stated, the domain configurations are initialized from a completely disordered random state while fixing the exact stoichiometry in the Ising case.

We investigate the ordering process in our microscopic model by applying the Metropolis algorithm (Metropolis et al., 1953) to the diffusion of a non-interacting vacancy through the system. At each step of the vacancy, one of its nearest neighbours is randomly selected. The bonds between equal and unequal atoms on the nearest and next-to nearest neighbours are counted and used as an index for a precomputed two-dimensional table of exchange probabilities. The exchange probabilities are given by the usual Metropolis probability $p(\Delta H)$

$$p(\Delta H) = \begin{cases} 1 & \Delta H < 0 \\ \exp\left(-\frac{\Delta H}{k_B T}\right) & \Delta H \geq 0 \end{cases} \quad (3.3)$$

where ΔH is the difference in the system's energy before and after the proposed exchange. The exchange is accepted if its probability is larger than another random number uniformly drawn between 0 and 1. In case of the L1₂ and m-L1₀ systems

the vacancy interacts with the other atoms as if it was a majority atom. Hence a proposed exchange between the vacancy and a majority atom will always happen. This updating strategy avoids trapping the vacancy in a locally optimal configuration. Additionally, it is more physically realistic and computationally efficient to consider only the nearest neighbours of the vacancy for exchanges instead of random sites in the lattice as in the so-called Kawasaki dynamics (Kawasaki, 1966; Bortz et al., 1974). Due to the cache architecture of modern CPUs, the good data locality of the nearest neighbour exchanges has a clear advantage over the random-exchange-site-update, where the nearest as well as next-nearest neighbours of the unpredictable locations have to be accessed in the main memory. Hence, if the efficiency is measured in CPU cycles per attempted site occupation exchange, the latter method is significantly slower, particularly for large systems.

In the case of the q -state Potts model, sites are updated via the heat bath algorithm (Creutz, 1980): The chosen site is reassigned to one of q APDs, independently of their former value. To determine its new APD value, the domain representation in its nearest neighbours is counted. For each kind of APD a probability p_i is computed

$$p_i = \exp(N_i/k_B T) \quad (3.4)$$

with N_i being the count of domain i in the nearest neighbours of the chosen position and $i \in [1, q]$. We sum these q probabilities and multiply the sum with a uniform random number $\eta \in [0, 1]$. We then successively subtract the probabilities p_i from the resulting value until it decreases below 0. The value of the domain i , whose probability p_i was subtracted last, is then assigned to the position. Sequential updating of sites leads to dynamical and, thus, potentially structural anisotropies, as the nearest neighbour of an updated site would be updated next and hence influenced by the new domain assignment of the updated site. Instead we can exploit the bipartite nature of the sc lattice: We cover the system by a three-dimensional checkerboard pattern and update the white and black sites in an alternating fashion. This approach is valid since sites of the same colour on the checkerboard can not interact directly with each other, as in the Potts model, exclusively nearest neighbour interactions are considered ($J_{nnn}=0$).

We define the unit of time, i.e. Monte Carlo step (MCS), for the microscopic cases as the trial of as many vacancy-atom exchanges as sites in the system. For the Potts model, one Monte Carlos step is defined as the reassignment of N^3 positions on an $N \times N \times N$ lattice, which corresponds to two checkerboard updates. During

the coarsening simulations, we followed the evolution of the configurations over 7500 MCS.

The simulations were performed on a workstation with four processor threads. We exploited the possibility of parallel execution for the Potts cases by splitting our checkerboard updates on the four threads. To this end, we divided the set of white or black sites along one dimension into eight slices and updated the even-numbered slices followed by the odd-numbered ones concurrently. For computing the reciprocal space scattering functions as well as the real space correlation functions, FFTW (Frigo and Johnson, 2005) was used. Due to the large system size, these quantities necessitates to a large data volume. To be able to handle them still, we reduced these three-dimensional quantities to one-dimensional radial averages on the fly during the simulation. We performed 40 to 80 of these coarsening simulations for each system. The correlation functions and scattering functions shown in the following sections are the averages over these independent configurations. The reported expected values of the derived parameters were also obtained from these averages. The estimated errors are derived via the bootstrap method (Efron and Tibshirani, 1994), that is, by repeatedly generating synthetic samples of configurations with the same number of elements by sampling with replacement from the simulations, performing the analysis on the corresponding averaged correlation or scattering functions, and computing the standard deviation thereof.

3.2.4 Equilibrium Properties

To confirm our implementations' validity as well as to determine the simulation temperatures of the m-L1₀ and L1₂ systems, we computed the temperature-dependent long-range order parameter $M(T)$ of our systems, determined the respective transition temperatures and compared them to well-known results of the q -state Potts model. In the case of the microscopic model, the stoichiometric concentrations are constant, and the long-range order parameter can be evaluated by the atom concentration on the sublattices

$$M(T) = c_{\alpha}^A - c_{\beta}^A = c_{\beta}^B - c_{\alpha}^B. \quad (3.5)$$

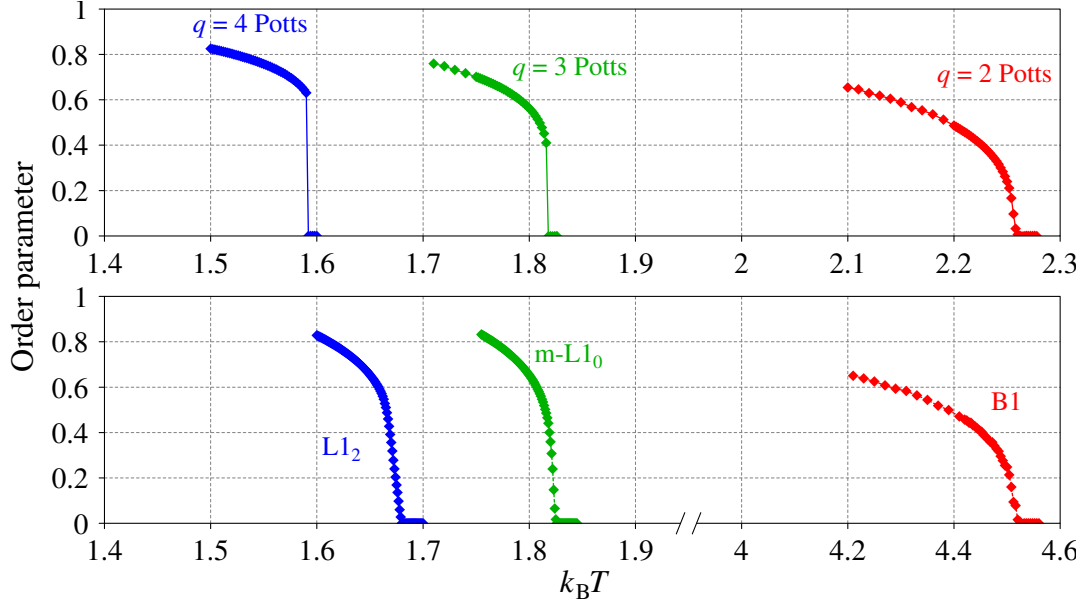


Figure 3.3: Temperature-dependent order parameters $M(k_B T)$ of the Potts (top) and microscopic systems (bottom).

For the q -state Potts model $M(T)$ is proportional to the proportion of the majority domain x in the system and is given as

$$M(T) = \frac{qx - 1}{q - 1}. \quad (3.6)$$

Both expressions of the long-range order parameter range from 0 (total disorder) to 1 (perfect order). The thermal evolution of $M(T)$ is displayed in Fig. 3.3, with the upper panel showing the simulation results of the Potts systems. In contrast, the ones of the microscopic systems are shown in the lower panel.

First, we discuss the evolution of the order parameter for the 2-state Potts model: Starting from a perfectly ordered state at low temperatures, we observe a continuous decrease from unity to 0 in $M(T)$ with increasing temperature, indicating a second-order transition. This thermal evolution of the equilibrium state is consistent with the well-known behaviour of the three-dimensional ferromagnetic $q = 2$ Potts case. With the order parameter reaching zero at about $k_B T_c = 2.255(2)$, our transition temperature agrees well with the currently best-known value of $k_B T_c = 2.25576163(5)$ (Ferrenberg, Xu, and Landau, 2018), which was obtained by methods much more efficient for second-order transitions than our simple local Monte Carlo updates. The microscopic B1 case becomes thermodynamically equivalent to the 2-state Potts system if we consider the B1 system under the conditions that the sign of the exchange

interaction constant J and the occupation of the sites of one colour in the three-dimensional checkerboard decomposition was flipped. The order parameter curves of both models coincide perfectly if a factor of 2 scales the temperature due to the spin units in the microscopic system being -1 and 1 instead of 1 and 0 as in the $q = 2$ Potts system. The corresponding transition temperature of the microscopic system is $k_B T_c = 4.510(2)$ which is consistent with the Potts value.

In case of the simulations for the 3 and 4-state Potts systems, we observe a discontinuous transition of the order parameter. Due to this discontinuity, simply increasing the ordering temperature on a perfectly ordered system would lead to inaccurate values of the transition temperature: In particular, one expects to observe the transition at a higher temperature (where the system is overheated) because the disordered phase has to nucleate in the ordered system first. For the opposite case, when starting from a disordered state, continuously decreasing the temperature would shift the transition to lower temperatures due to the necessary nucleation of the ordered phase, undercooling the system. Hence we determined the transition temperature by starting with an inhomogeneous system consisting of an ordered and a disordered part and adjusted the simulation temperature until the two phases were seemingly in equilibrium, which was indicated by the order parameter showing a purely stochastic evolution with simulation time. The presented curves are derived from heating and cooling simulations, spliced together at the critical temperature obtained as detailed above. We observe a transition at $k_B T_c = 1.8164(1)$ and $1.5907(1)$ for the 3- and 4-state Potts model, respectively. This result reproduces their well known behaviour (Wu, 1982) and our values of the transition temperatures are consistent with the most precise reported values of $k_B T_c = 1.816315(20)$ and $1.590816(9)$ (Bazavov, Berg, and Dubey, 2008).

Superficially, the evolution of the order parameters for the microscopic $q = 3$ and $q = 4$ cases seem to display a similar discontinuous behaviour as the respective Potts systems. More rigorous considerations show an approximately linear decrease in the simulations for both microscopic systems over the regions $k_B T \in (1.814, 1.830)$ in case of $q = 3$ and $k_B T \in (1.668, 1.680)$ in the $q = 4$ case. This linear decrease arises from the stoichiometric concentrations being constant in the microscopic model. It results from the coexistence of an ordered and a disordered phase close to the transition temperature in the cases of $q > 2$. In this coexistence region, there is with increasing temperature a gradual shift from the ordered to the disordered phase. This coexistence represents the equilibrium behaviour of this system and is familiar from binary alloy phase diagrams, where two-phase regions typically separate different

phases. In the $q = 2$ model, the symmetry of the system leads to a congruent transition fixed at stoichiometry.

3.3 Domain Coarsening

During the disorder-order transition, ordered domains nucleate and grow, leading to a division of the crystal in APDs. In an actual experimental sample or a simulation, each realization of a configuration will have a different arrangement of these APDs. However, all arrangements result from the same growth and coarsening dynamics and therefore possess the same statistical properties, which can be discussed and compared. A typical statistical summary for this purpose is the pair-correlation function of the APD, $g'(\mathbf{r})$, which characterizes the probability of two positions to share the same domain when they are separated by a vector \mathbf{r} . In the q -state Potts model, sites are assigned to domains, allowing the direct computation of the conventional pair-correlation function. In the microscopic model computing the conventional pair-correlation function directly from the atomic configuration results in an attenuated oscillation, as depicted in the panel on the right of Fig. 3.4. To obtain the pair-correlation function of the respective domain assigned configuration, shown in the intermediate panel of Fig. 3.4, we used the following definitions: For the B1 case, we covered the system by a three-dimensional checkerboard pattern, exchanged the atom value σ of the white sites by its opposite and computed the conventional pair-correlation function. In the case of the m-L1₀ and L1₂ systems, the crystal structures can be described by three or four interpenetrating sc sublattices. For each sublattice the pair-correlation function of the minority atoms is considered separately. Summing over the respective contributions gives us the pair-correlation function of the whole system, with the smallest accessible distance corresponding to the cubic lattice constant. A given unit cell can belong to zero, if all sites are occupied by majority atoms, one, if only the site i is occupied by a minority atom and all other sites by the majority atoms, or more domains, if the specific unit cell is occupied by more than one minority atom.

In order to be able to compare the pair-correlation functions for different q , here we will use a rescaled version that decays from 1 at small distances to 0 at infinity. Specifically, our rescaled correlation function $g(\mathbf{r})$ is defined as

$$g(\mathbf{r}) = (qg'(\mathbf{r}) - 1) / (q - 1). \quad (3.7)$$

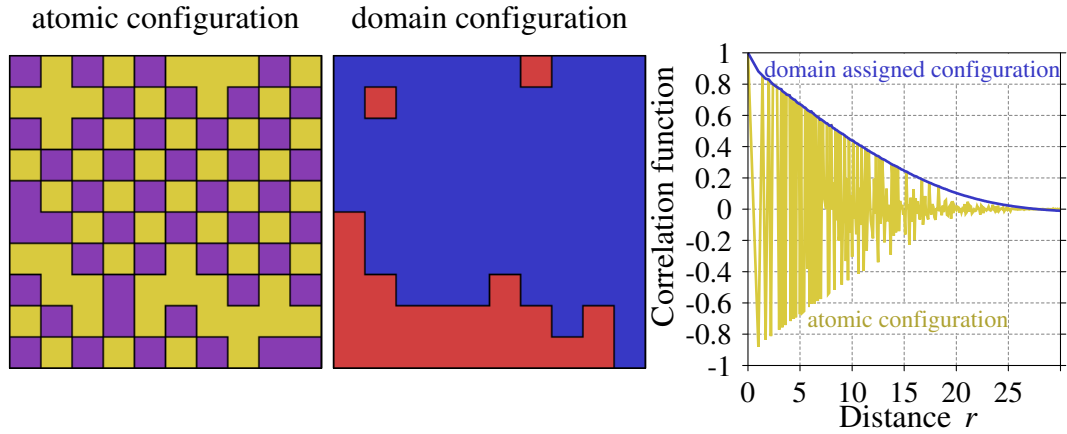


Figure 3.4: Atomic configuration of the B1 model for a system size $N = 100$. The respective domain assigned configuration is obtained by multiplying the atomic configuration with the 3D-checkerboard construct. The corresponding radially averaged pair-correlation functions are shown on the right.

3.3.1 Simulation Temperature and Exchange Interaction

To compare the microscopic and Potts systems qualitatively, independent of the underlying crystal structure or number of APDs present in the systems, we investigate the spherically averaged pair-correlation function. Hence the domains have to grow isotropically in all our systems, which depends strongly on the exchange interaction and the simulation temperature. The effects of ordering at low temperatures and considering for the $L1_2$ case exclusively nearest neighbour interactions are discussed in the next section, while the consequences of ordering at high temperatures are considered in Sec. 3.3.1.2

3.3.1.1 Faceting

The curvature of the domains as well as the thickness and direction of the APB are strongly dependent on the ordering temperature and the crystal structure. The energetically favourable close-packed directions in the $L1_2$ system can be taken from Fig. 3.5, with exclusively nearest neighbour interactions ($J_{\text{nnn}} = 0$) being considered. As mentioned in Sec. 3.2.1, for the microscopic m- $L1_0$ and $L1_2$ cases we observed for this exchange interaction the APDs to be strongly faceted in the $\{100\}$ planes (Frontera et al., 1997), as it is possible to build energy-free APBs between the domains.

In order to test for anisotropy in the statistical properties of the APD configurations, we performed dedicated coarsening simulations on smaller systems (N up to 240)

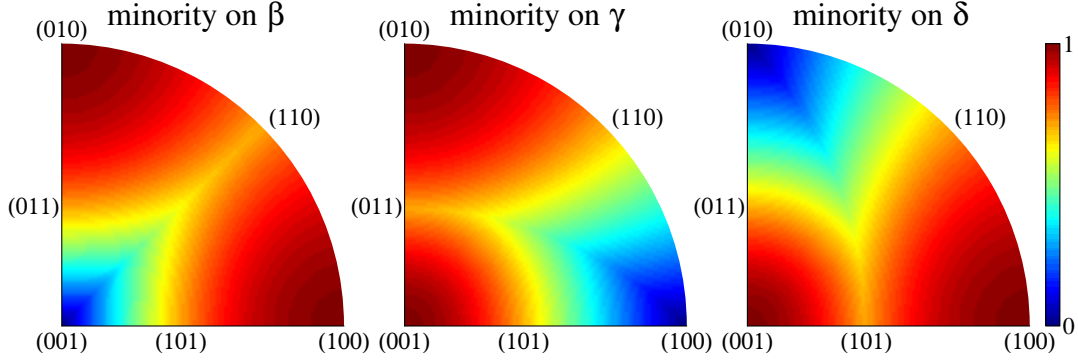


Figure 3.5: Stereographic projection of the energy per APB for a domain in the $L1_2$ system, with the minority atoms occupying the α sublattice. We consider exclusively nearest neighbour interactions ($J_{\text{nnn}} = 0$): the neighbouring domains have the minority atoms occupying the β , γ and δ sublattice, respectively. For each of these neighbouring domains it is possible to build an energy-free APB between them.

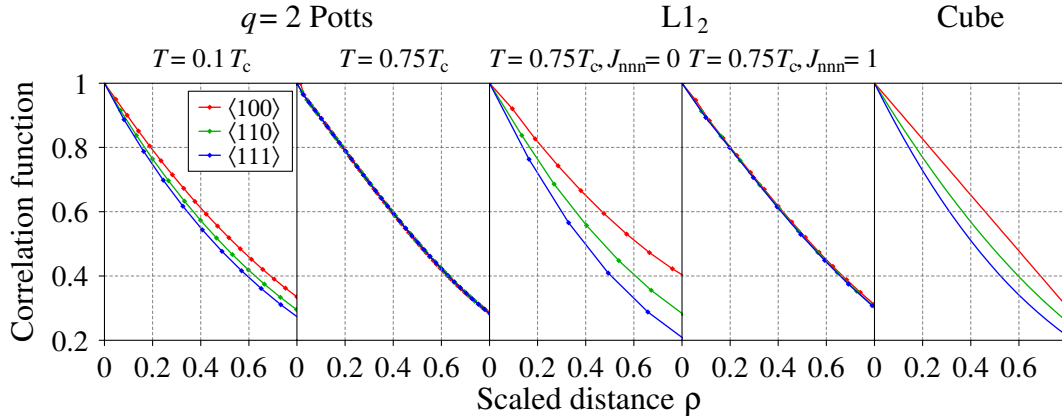


Figure 3.6: Direction-dependent pair-correlation functions: $q = 2$ Potts system at $k_B T = 0.1 T_c$ and $0.75 T_c$, $L1_2$ system with $J_{\text{nnn}} = 0$ and $J_{\text{nnn}} = 1$, all after 1500 MCS apart from $L1_2$ system with $J_{\text{nnn}} = 0$, which due to its slow coarsening was simulated for 30 000 MCS, compared with the pair-correlation function of a cube.

and evaluated directionally dependent correlation functions in $\langle 100 \rangle$, $\langle 110 \rangle$ and $\langle 111 \rangle$ directions as reported in Fig. 3.6.

When ordering at the low simulation temperature of $0.1T_c$, we observe the expected directional differences of $\sim 10\%$ in the correlation functions for the $q = 2$ Potts case. The initial decay of the correlation function is the steepest in the $\langle 111 \rangle$ directions, followed by the $\langle 110 \rangle$ directions. However, ordering at $0.75T_c$ leads to visually vanishing differences, i.e. the correlation functions in the $\langle 100 \rangle$, $\langle 110 \rangle$ and $\langle 111 \rangle$ directions differing less than 3%.

The microscopic $L1_2$ case shows a strong anisotropy even at simulation temperatures close to the transition temperature $T = 0.75T_c$, when considering only next neighbour interactions $J_{nnn} = 0$. The respective transition temperature is taken from Kessler, Dieterich, and Majhofer (2003b). We observe the steepest decay in the $\langle 111 \rangle$ directions, as seen before for the low-temperature $q = 2$ Potts case. However, when the next-nearest neighbour interactions, $J_{nnn} = 1$, are considered, the differences between the directionally dependent correlation functions are not noticeable by the eye.

In both anisotropic cases considered here, the observed behaviour of the directionally dependent correlation functions is consistent with the preference of building APBs parallel to the $\{100\}$ planes. These planes are the energetically preferred ones for the sc and fcc lattices when considering exclusive nearest neighbour interactions, as indicated in Fig. 3.5. The anisotropy of the systems is as distinctive as possible under cubic symmetry, which becomes clear when considering the following extreme case: Let us consider an APD configuration on a lattice of cubes, with the volume enclosed by a given cube being assigned to a random APD. The resulting correlation function can be calculated analytically as the auto-correlation function of a single cube-shaped domain

$$g(\rho) = \begin{cases} \max(0, 1 - \rho) & \text{along } \langle 100 \rangle \\ \max(0, 1 - \rho/\sqrt{2})^2 & \text{along } \langle 110 \rangle \\ \max(0, 1 - \rho/\sqrt{3})^3 & \text{along } \langle 111 \rangle. \end{cases} \quad (3.8)$$

Fig. 3.6 shows that an $L1_2$ -system with exclusively nearest neighbour interactions gives anisotropies as pronounced as this most extreme model of cubic APDs. For the sake of simplicity, in the following sections we will report only radially averaged correlation functions $g(r)$, since we can safely assume the APD configuration to be isotropic under the following two conditions: First, when the ordering process happens at the simulation temperature $0.75 T_c$, which we use in the remainder in this

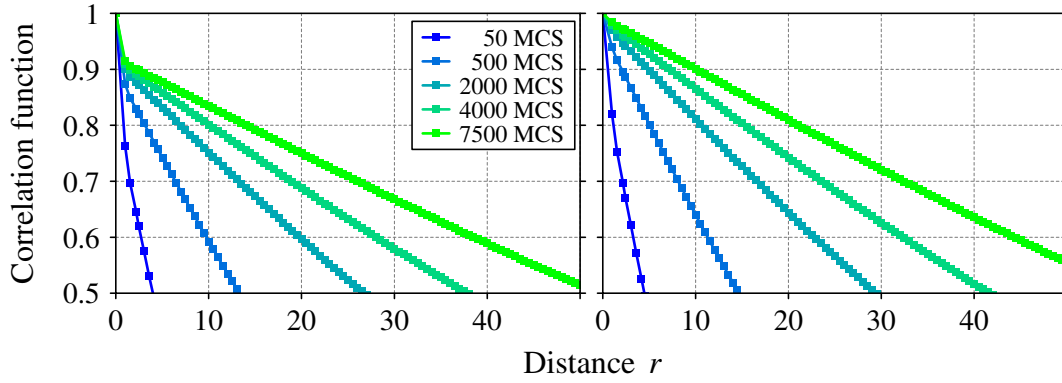


Figure 3.7: APD correlation functions of the $q = 4$ Potts model in the fully uncorrected version (left), and corrected for disorder according to Eq. (3.11) (right).

work. Secondly, we need to consider second-nearest neighbour interactions for the microscopic m-L1₀ and L1₂ cases.

3.3.1.2 Correcting For Disorder

In case of a perfectly ordered system the correlation function is unity at all distances r . However diffuse APBs that show approximately isotropic configurations require a high ordering temperature which leads to having a significant concentrations of point defects also away from the APBs. To give an accurate description and model of the correlation functions we need to correct for the effects of local disorder inside of the domains as well as at the APBs and obtain the correlation function $g'(r)$ of the idealized APD configuration unaffected by thermal disorder. We start with the effect due to a finite long-range order parameter, giving point defects inside the domain. Without correction for thermal disorder we obtain the apparent APD correlation function $f'(r)$ determined as detailed in Sec. 3.3, which is reduced compared to $g'(r)$ due to thermal disorder.

In equilibrium one domain dominates while the other domains contribute equally as point defects. If $p(r)$ is the probability that two points separated by a distance r are assigned to the same domain in equilibrium, we can write the uncorrected APD correlation function in a coarsening simulation as

$$f'(r) = g'(r)p(r) + \frac{(1 - g'(r))(1 - p(r))}{q - 1}. \quad (3.9)$$

Here we made the approximation that the correlations of point defects as quantified by $p(r)$ behave across APD boundaries as they do within a domain, which will be exactly fulfilled in the limit of vanishing point defect correlations, that is, at large

distances. Solving for $g'(r)$ gives

$$g'(r) = \frac{(q-1)f'(r) - 1 + p(r)}{qp(r) - 1}. \quad (3.10)$$

Hence our rescaled pair-correlation function $g(r)$ is given according to Eq. 3.7 as

$$g(r) = \frac{qf'(r) - 1}{qp(r) - 1}. \quad (3.11)$$

For simplicity, and justified by the fact that in fitting we anyway consider the correlation functions only for $r \geq 10$ in order to avoid effects due to short-range order of defects, we replace $p(r)$ by its long-distance limit, given by the concentration of point defects in equilibrium as determined in dedicated simulations.

Fig. 3.7 illustrates the effect of the correction for thermal point defects. While the improvement is obvious, a close look shows that the expected behaviour of an extrapolation to exactly 1 as $r \rightarrow 0$ is still not fulfilled. This behaviour arises from the depression of order close to the APB, where the introduction of a point defect is less costly than in the inside of the domains. In the simplest approach, we can model the APBs as having a finite width c , within which the order is completely lost. As the specific interface area, in the sense of interface area per unit volume, is defined by ξ , the extrapolation of the correlation function to $r = 0$ will correspondingly decrease from 1 to $1 - c\xi$. Due to the correlation function's derivative of $-\xi$ at 0, we correct this effect by shifting the distance scale r by c . The fitted values for c with increasing q are 0.75, 0.62 and 0.51 for the Potts cases, and 0.76, 0.71 and 0.57 for the microscopic systems.

Hence, to have approximately isotropic APD configurations without introducing too much atomic-scale disorder, we use consistently temperatures of about 75% of the phase transition temperature T_c for our coarsening simulations. Specifically, we use $k_B T$ of 1.7296, 1.4, and 1.2 for the q -state Potts cases of $q = 2$, $q = 3$, and $q = 4$. For the microscopic B1, m-L1₀ and L1₂ cases we assume $k_B T = 3.4592$, 1.36275, and 1.26.

3.3.2 Dynamical Scaling

Fig. 3.8 depicts the general evolution of the ordering process for the q -state Potts models by showing the domain assigned configurations at several time steps. With increasing ordering time the APDs coarsen, and their surface energy decreases. In the

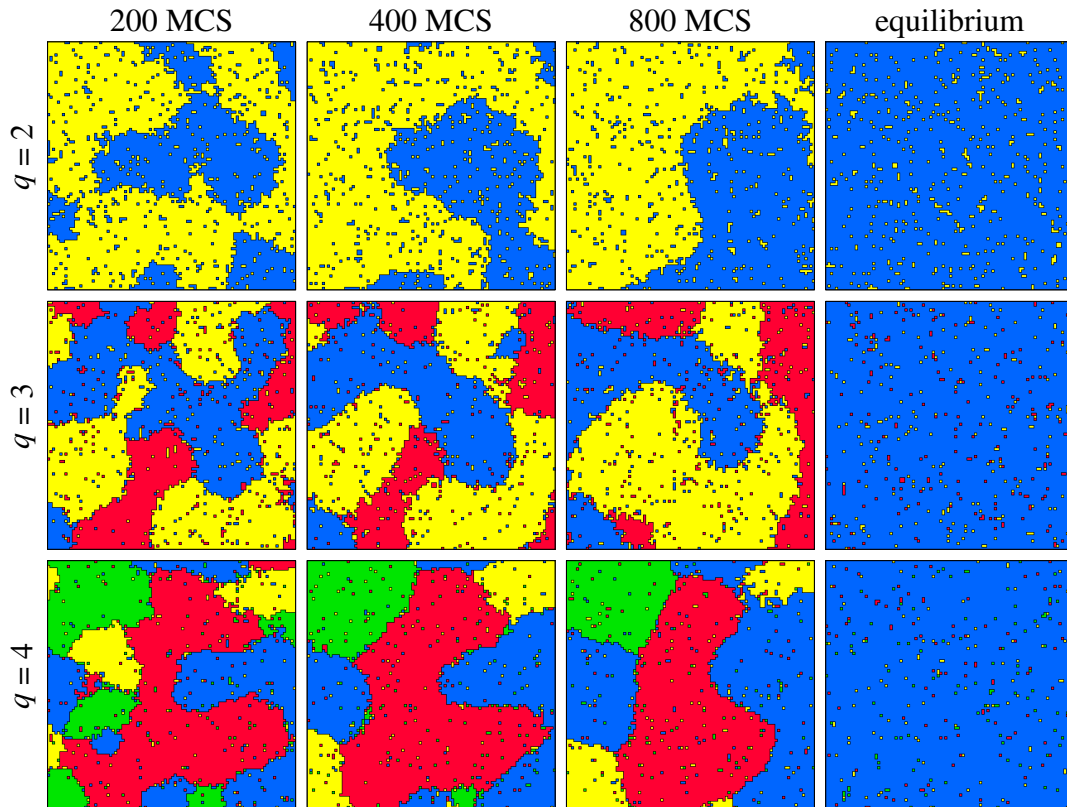


Figure 3.8: Coarsening configurations for the three Potts models at various stages, together with final configuration of a single domain with isolated point defects. Shown are sections of 100 sites edge length of two-dimensional slices, while the three-dimensional simulation box is considerably larger. The equilibrium configurations were obtained after 1000 MCS starting from a perfectly ordered configuration.

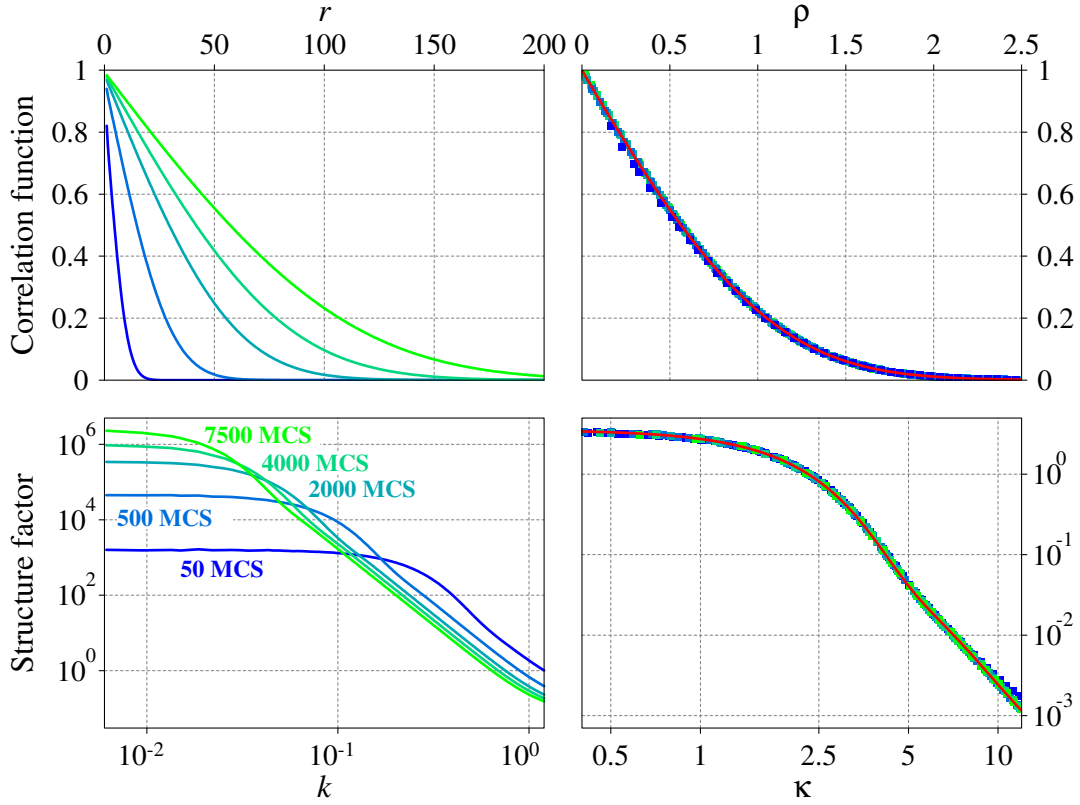


Figure 3.9: Simulated radially averaged real-space correlation functions (top left) and reciprocal-space structure factors (bottom left) of $q = 4$ Potts model at various coarsening stages. In the right column, the data are replotted on the scaled coordinates together with the scaling functions in red, demonstrating the universal shape in the scaling regime. Note that only a subset of simulated points is plotted for being able to distinguish the data sets.

final equilibrium state, a single domain dominates, and only local disorder remains in the system.

The pair-correlation functions $g(r)$ of the $q = 4$ Potts system are depicted in the upper panel of Fig. 3.9 for various coarsening times t . As the domains grow, the correlation length increases and the APB density ξ decreases. Since for small distances r the unscaled correlation function can be approximated by $g'(r) \propto (1 - \xi r)$, the decay of $g(r)$ is slowed down with increasing domain size.

The lower panel of Fig. 3.9 illustrates the respective Fourier transforms of $g(r)$, the structure factor $S(k)$. With increasing ordering time, we observe a redistribution of intensity to lower k , indicating increased long-range order. This shift in intensity converts to the growth of large structures, such as APDs. We observe this general

evolution of order in all investigated systems, independent of the number of APDs or crystal structures.

According to the scaling hypothesis, the pair-correlation functions and their Fourier transforms can be scaled on top of each other for late ordering times. This is fulfilled in our simulations as illustrated in Fig. 3.9 b) and d) for the $q = 4$ Potts case. A single scaling parameter $L(t)$ can match both real-space correlation functions and reciprocal-space structure factors with high accuracy and precision. The transformed functions are given by

$$\rho = rq/L(t)(q - 1) \quad \text{and} \quad (3.12)$$

$$\kappa = kL(t)(q - 1)/q, \quad (3.13)$$

respectively. The newly introduced term $q/(q - 1)$ will be explained in more detail within Sect. 3.5.3. For short ordering times, the scaling factor becomes so small that it reaches the lower limit of the fundamental discretization of space, the nearest neighbour distance. Due to the overlap of this lower limit and the features due to the APD configuration, we observe deviations from scaling at small ρ and large κ , respectively.

3.4 The Scaling Function

3.4.1 Phenomenological Ansatz

In order to describe the general form of the scaling function in real as well as reciprocal space by an analytic expression, we use a combination of an exponential decay and Gaussian functions as an *ansatz*. We found that our scaled correlation functions are satisfactorily described by a linear combination of an exponential decay and two Gaussian functions

$$g(\rho) = b \exp(-\rho/b) + \sum_{i=1}^2 a_i \exp(-\rho^2/2\sigma_i^2). \quad (3.14)$$

The first general restriction of this scaling function is the unity condition $g(0) = 1$, which is necessary for all correlation functions. It is fulfilled by setting $b = 1 - a_1 - a_2$. The derivative of the pair-correlation function gives the second condition: As mentioned before, for small distances the unscaled correlation function $g'(r)$ can be approximated by a linear decrease via the specific interface area ξ , which is defined

as the average area of interface per unit volume, $(g'(r) \propto 1 - \xi r)$. By construction the derivative of our scaling function is -1 at $\rho = 0$. Hence this condition allows us to define the spatial scale of a simulated APD configuration via the scaling factor $L(t)$. In order for the scaling function to fit on the simulated correlation function at coarsening time t , it needs to be scaled by the factor $L(t)$ via Eq. (3.12). The scaling factor is proportional to the inverse of the specific interface area of the configuration, $L(t) = 2/\xi$, which will be discussed in detail in Sect. 3.5.3. The behaviour of $L(t)$ as a function of the coarsening time t is investigated and discussed below in section 3.5.1.

Since the scaling function is a radial symmetric function in real space, its corresponding three-dimensional Fourier transform can be obtained using the following theorem by Iosevich and Liflyand (2014)

$$(\mathcal{F}(f))(\kappa) = 4\pi \int_0^\infty d\rho \frac{\sin(\kappa\rho)}{\kappa} f(\rho)\rho. \quad (3.15)$$

The expression for the respective structure factor is

$$S(\kappa) = \frac{8\pi}{(\kappa^2 + 1/b^2)^2} + \sqrt{8\pi^3} \sum_{i=1}^2 a_i \sigma_i^3 \exp(-\kappa^2 \sigma_i^2/2). \quad (3.16)$$

Further, integrating this three-dimensional radially symmetric function over two perpendicular dimensions gives the expression corresponding to the peak profile in powder diffractometry

$$S'(\kappa_x) = \frac{8\pi^2}{\kappa_x^2 + 1/b^2} + \sqrt{32\pi^5} \sum_{i=1}^2 a_i \sigma_i \exp(-\kappa_x^2 \sigma_i^2/2), \quad (3.17)$$

which is remarkably similar to the phenomenological pseudo-Voigt profiles typically used for this purpose.

The exponential decay at large ρ of this expression in real space conflicts with the expected super-exponential decay due to diffusive interaction (Bray, 2002), but we want to note that the asymptotic real-space behaviour is practically accessible neither in simulations nor in experiments. In reciprocal space, our expression for the structure factor gives the correct asymptotic behaviour both for small and large κ .

	$q = 2$		$q = 3$		$q = 4$	
	Potts	B1	Potts	m-L1 ₀	Potts	L1 ₂
a_1	0.0557(106)	0.0428(60)	0.0419(67)	0.0609(62)	0.0450(37)	0.0551(42)
a_2	0.6296(242)	0.5805(139)	0.5506(172)	0.5634(161)	0.5253(90)	0.5129(98)
σ_1	0.2841(47)	0.2905(71)	0.2930(59)	0.3170(57)	0.3126(30)	0.3713(50)
σ_2	0.6280(27)	0.6240(34)	0.6609(31)	0.6499(65)	0.6860(21)	0.6954(55)

Table 3.1: Parameters of the scaling function given in equation Eq. (3.14) for all systems.

3.4.2 Fitting the Scaling Function

For all our six systems, we determine the four parameters of Eq. (3.14) via least-squares fitting of the scaled pair-correlation functions at successive coarsening time steps in real space. To minimize the effects of short-range order, we consider only values of the spatially unscaled correlation function $g(r)$ at distances $r \geq 10$ in units of the simple-cubic lattice constant. We modelled the scaling function to the scaled correlation functions by minimizing the weighted squared deviations using weights in time and space. The spatial weights are given by splitting the spatial range of $0.1 \leq \rho \leq 5$ into 20 *logarithmically* equidistant bins, with each interval contributing according to its width in logarithmic units. The weights for the coarsening time are considered analogously in the range $25 \text{ MCS} \leq t \leq 7500 \text{ MCS}$. In our view, this is the most efficient way to use the available information in the simulations: As we will discuss in Sec. 3.5.1, $L(t)$ shows a power-law behaviour in coarsening time t (Allen and Cahn, 1979). Hence, for a given logarithmic increment in t , the scale parameter L of the newly attained configuration has increased by a given factor. The parameters are obtained iteratively, by fitting first the scaling factor $L(t)$ to rescale the correlation functions onto the model function and then the parameters a_1 , a_2 , σ_1 , and σ_2 of the common model function.

The parameters of the scaling function of each system are listed in table 3.1. For convenience, we also give the full widths at half maximum B_{FWHM} and the integral breadth B_{I} of the corresponding powder diffractometry peak profiles in Tab. 3.2. The estimated statistical errors were obtained by bootstrap sampling (Efron and Tibshirani, 1994).

For the $q = 4$ Potts case, the scaled correlation functions are plotted together with their real-space scaling function in the upper panel of Fig. 3.9, while the corresponding results for the reciprocal space are shown in the lower panel. The agreement is in

	$q = 2$		$q = 3$		$q = 4$	
	Potts	B1	Potts	m-L1 ₀	Potts	L1 ₂
B_{FWHM}	4.058(16)	4.064(17)	3.852(25)	3.952(44)	3.726(17)	3.699(35)
B_{I}	5.113(20)	5.137(17)	4.928(24)	5.033(45)	4.804(17)	4.765(35)

Table 3.2: The full width at half maximum B_{FWHM} and integral breadth B_{I} of the powder-diffraction intensity given in equation (3.17).

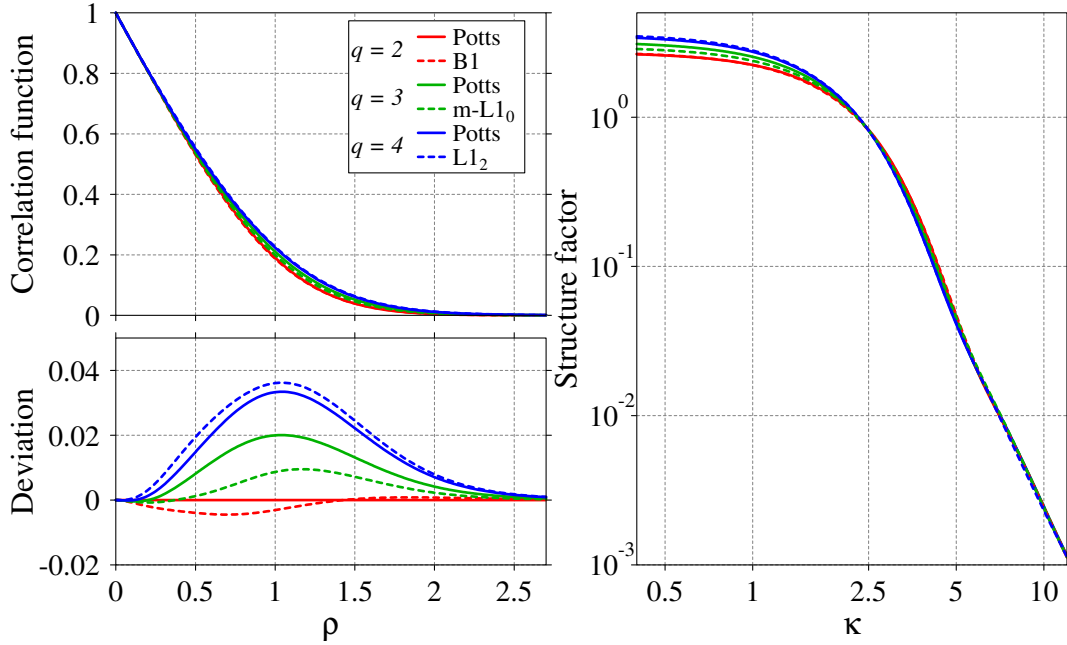


Figure 3.10: Scaling functions for the real-space correlation functions (left) and reciprocal-space structure factors (right), comparing our phenomenological functions according to Eqs. (3.14) and (3.16) for the Potts and microscopic systems for various q . To highlight the differences between the systems, the lower panel shows the deviations with respect to our $q = 2$ Potts correlation function.

real and in reciprocal space very good, even though only the real-space correlation functions are used to determine the parameters of the scaling function.

The obtained scaling functions of all systems are depicted in Fig. 3.10 in real as well as reciprocal space. Even though the systems qualitatively differ on the microscopic scale, the resulting rescaled correlation functions and the respective structure factors match to a high degree. However, a detailed visual inspection shows that minute differences exist specifically between curves of different q , while the curves that correspond to the microscopic and q -state Potts models for the same q can hardly be distinguished by eye. The respective deviations between the real-space scaling functions, depicted in the lower panel of Fig. 3.10, support these observations. An

		$q = 2$		$q = 3$		$q = 4$	
		Potts	B1	Potts	m-L1 ₀	Potts	L1 ₂
$q = 2$	Potts	0	0.0036(19)	0.0181(28)	0.0081(36)	0.0306(23)	0.0341(39)
	B1	-	0	0.0207(27)	0.0103(43)	0.0331(22)	0.0368(39)
$q = 3$	Potts	-	-	0	0.0104(46)	0.0125(27)	0.0162(41)
	m-L1 ₀	-	-	-	0	0.0229(45)	0.0265(55)
$q = 4$	Potts	-	-	-	-	0	0.0040(25)
	L1 ₂	-	-	-	-	-	0

Table 3.3: The L^2 -distance between the real-space correlation functions of the different systems, along with estimated statistical errors.

exception is the case $q = 3$, where the m-L1₀ scaling function is about half-way between the $q = 3$ Potts and both $q = 2$ cases.

With increasing q the decay from $g(\rho = 0) = 1$ to $g(\rho \rightarrow \infty) = 0$ decreases at intermediate distances. We attribute this behaviour to the increasing number of domains whose boundaries meet at a single point. On an sc lattice with exclusive nearest neighbour interaction, the highest degeneracy of a border junction is fourfold, going from edges present for $q \leq 3$ to corners for $q \geq 4$. To understand the implication of this APB degeneracy better, let us consider the following construct: Imagine a three-dimensional space which is divided into a large number of randomly arranged compact regions. We construct a q -state APD configuration by randomly assigning a state from 1 to q to each region. Due to this random assignment the correlation function is independent of q . However, allowing the domains to coarsen leads for the $q = 2$ case quickly to evolve smooth boundaries, thereby decreasing the interfacial area ξ and leading, due to $g(\rho) \approx 1 - \xi\rho$, to increased correlations at small ρ . For larger q edges and corners will evolve, giving a comparatively smaller increase at small ρ .

To substantiate the statement that systems with the same q bear a significantly closer similarity than systems of different q , we report the L^2 -distances between the scaling functions of the different systems in Tab. 3.3. Their estimated statistical error was obtained by bootstrap sampling. Indeed, these values show that the discrepancies between microscopic and q -state Potts models for the same q are, in most cases, much smaller than the differences between models for different q . The deviations between systems for the same q are also typically a factor two larger than the corresponding expected errors. The above-noted $q = 3$ case is no exception from this observation, but only shows a larger estimated error. Hence, our simulations are still consistent with the hypothesis of universal scaling functions for given q . Further, the values

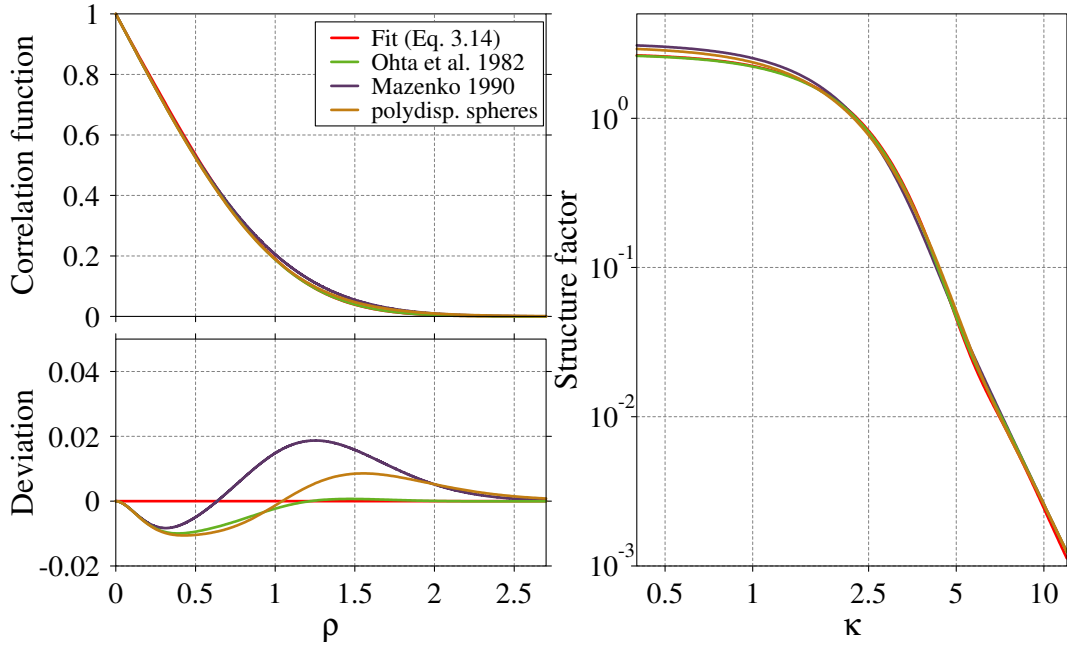


Figure 3.11: Scaling functions for the real-space correlation functions (left) and reciprocal-space structure factors (right), comparing our phenomenological functions according to Eqs. (3.14) and (3.16) for the $q = 2$ Potts function to various theoretical predictions for $q = 2$. To highlight the differences between the theories, the lower panel shows the deviations with respect to our $q = 2$ Potts correlation function.

imply that the progression of the scaling function with q is essentially along a line in high-dimensional space. In particular, the distance between $q = 2$ and $q = 4$ in the microscopic as well as in the q -state Potts models is equal to the sum of the distances between $q = 2$ and $q = 3$ and between $q = 3$ and $q = 4$, which is not so obvious from a direct comparison of the model parameters due to their correlations.

Ohta, Jasnow, and Kawasaki (1982) and Mazenko (1990) gave analytic predictions for the form of the scaling function in the $q = 2$ case: the OJK model and the Mazenko theory, respectively. In Fig. 3.11 our scaling function of the $q = 2$ Potts system is depicted together with the correspondingly scaled predictions of the OJK and Mazenko theories. Given the fact that, as discussed, system properties, such as q , have only a small effect on the correlation function, the OJK theory displays a markedly better agreement with the simulations than the Mazenko expression. For example, the L^2 -distance between our scaling function and the OJK theory is 7.1×10^{-3} in comparison to a value 16.3×10^{-3} for the Mazenko one. The latter seems to represent the $q = 3$ case more than the actually considered $q = 2$ one.

Finally, we investigate the similarities of our scaling function to the correlation function of spatially uncorrelated polydisperse spheres, a common approximation

of the structure factor in small angle experiments. Using Eq. (3.15) we obtain the Fourier transform of the squared form factor of Gaussian distributed polydisperse spheres whose radii are log-normal distributed. Its parameters, the mean μ and the standard deviation σ , fulfill the condition $\mu = -5/2\sigma^2 + \log(3/4)$, which is needed for the derivation being -1 at $\rho = 0$, with $\sigma = 0.3$. For this value of σ we observe the closest agreement of the approximation and our scaling function, with a L^2 -distance of 10.5×10^{-3} . A systematic effect common to all theoretical expressions is an underestimation of the simulated correlation function at small distances ρ , as can be seen in the deviation plot (on the lower left in Fig. 3.11). As far as we know, there have not been any theoretical predictions for the correlation functions for $q > 2$.

3.5 Growth of the Anti-Phase Domains

3.5.1 Kinetics

To investigate the growth of APDs, we study the time-dependent behaviour of the scaling factor $L(t)$. Figure 3.12 depicts the temporal evolution of $L(t)$ for the q -state Potts and microscopic systems. For the simple Ising model, the increase of the APD size should follow the predicted power-law dependence on time with an exponent of $\nu = 1/2$ (Allen and Cahn, 1979). The same power-law dependence should be observed for the Potts cases (Rutenberg and Bray, 1995). Since we start each simulation from a completely random state, the length scale with which the simulation enters the scaling regime is not necessarily consistent with the time it does so according to the scaling relation. Hence, the absolute zero of time has to be regarded as a free parameter. We shifted the data in time, typically by positive values of a few MCS, to obtain a small- t behaviour as systematic as possible.

At first sight, the growth of the APDs in the Potts systems seems to follow the expected square root behaviour $t^{1/2}$ (Rutenberg and Bray, 1995) quite well. However, a detailed inspection shows that the temporal evolution of the scaling factor is best described when the exponent ν is reduced to $\nu = 0.48$. (Grest, Anderson, and Srolovitz, 1988) and (Blundell and Bray, 1994) already reported such behaviour and suggested that either pinning of defects on the lattice or the asymptotic regime having not yet been reached (Blundell and Bray, 1994) explain this reduction of the expected exponent. Since we performed simulations on much larger lattices and longer simulation times than the ones used in (Grest, Anderson, and Srolovitz, 1988; Blundell and Bray, 1994), we can safely dismiss the latter option. Having simulated all Potts case on an sc

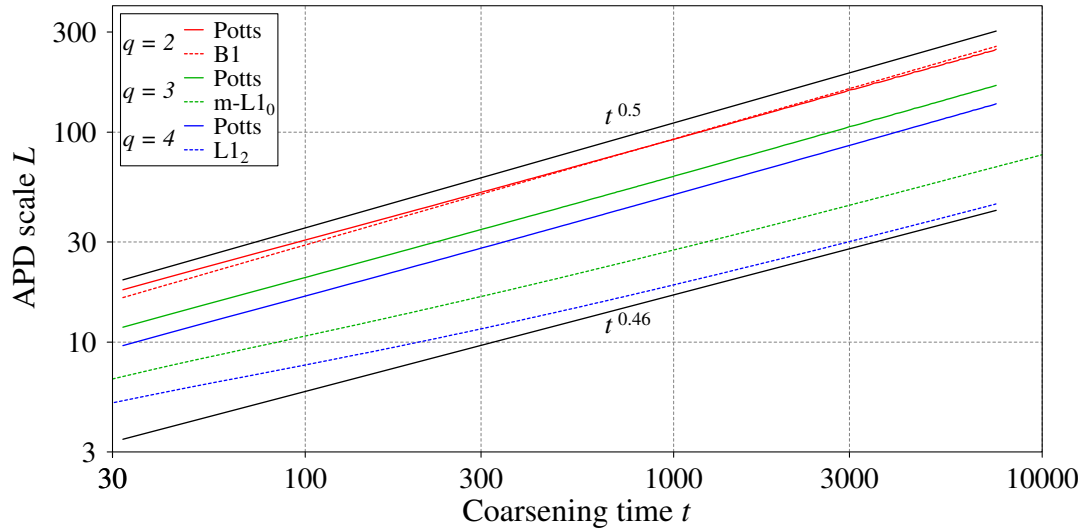


Figure 3.12: Growth of the scaling factor $L(t)$ with the coarsening time t for all considered systems. The black solid lines represent the behaviour $L(t) \propto t^{0.5}$ and $L(t) \propto t^{0.46}$

lattice by using the same updating method the evolution of the spatial length scale differs between the Potts cases only in q . Hence we can directly compare their kinetic behaviour and observe that with increasing q , domain coarsening slows down. This deceleration is due to the increasing number of neighbouring domains to a given domain, as we observed before when comparing the respective correlation functions: the appearance of APD boundary edges (at $q = 3$) and corners (at $q = 4$), and thus a reduction of the mean boundary curvature at given domain scale, are the dominant effects for this behaviour.

For the microscopic model, we observe a different behaviour. For the B1 case, the temporal evolution of the spatial scale is best described by a power-law dependence with a growth exponent of about 0.505. This value is slightly but significantly higher than the expected 0.5 growth exponent. We attribute this behaviour to the attraction of the vacancy to the domain boundaries, where it is more effective for the coarsening process (Fratzl and Penrose, 1994). With increasing domain size, the proportion of the interface area in the system decreases. Hence, as the simulation time goes on, the vacancy concentration increases preferentially within the boundary rather than the ordered domain. This results in an acceleration of the coarsening process (Vives and Planes, 1992; Frontera, Vives, and Planes, 1994).

The APDs in the m-L1₀ and L1₂ systems show a significantly slower evolution with simulation time than the expected power-law dependence. Instead of following a power law with a fixed exponent of 0.5, we observe a monotonously increasing

exponent with a maximum value of 0.46 in the final stages of the simulations. We think this is due to the conservation laws in the microscopic systems. Due to the asymmetric stoichiometry in these systems, unlike in the B1 case, the concentration of minority to majority atoms in an APB is not the same as inside a domain. With having one atom type occupying positions rather inside the boundary region than inside the APD for the domain to grow, the APB containing segregated atoms has to move, thereby slowing the growth of the domain down. Due to these microscopic differences the definitions of the domain scales can not be compared for the microscopic models, unlike in the Potts cases. Hence the qualitative similar behaviour of the growth kinetics being slowed down with increasing q , which we observed for the Potts cases, should be regarded as fortuitous.

3.5.2 Temperature Dependence

Next we study the temperature-dependence of the APD growth. Due to the above-mentioned evolution of the spatial length scale for the microscopic models, we investigated the temperature-dependent behaviour solely in the Potts systems on a smaller lattice size with $N = 250$ with coarsening times t of up to 2000 MCS. We expect to find the temporal evolution of the scaling factor to follow the power-law dependence $L(t) \propto B(T)t^\nu$ where $B(T)$ denotes the temperature-dependent growth rate. Since the Metropolis probability (Eq. (3.3)) to accept an energetically unfavourable exchange depends exponentially on temperature, $p(\Delta H) = \exp(-\Delta H/k_B T)$, the growth rate decreases with decreasing temperature, showing an Arrhenius-type behaviour of $-\ln(B(T)) \propto T_c/T$ (Allen and Cahn, 1979; Weinkamer et al., 1998; Kessler, Dieterich, and Majhofer, 2003b).

We investigated the thermal evolution of the growth rate $B(T)$ in a temperature range between $0.1 T_c$ and $0.95 T_c$. For each temperature and system, we performed up to 40 coarsening simulations. Even though we observe at such low ordering temperatures the APDs to be slightly faceted, as shown in Sec. 3.3.1.1, radially averaging the pair-correlation function corrects for these anisotropies. The averaged pair-correlation functions of these simulation temperatures show a good agreement with their respective scaling functions, as displayed in Fig. 3.13 for the $q = 4$ -state Potts system at $0.5T_c$. The temperature-dependent growth rates of the system are shown in the right panel of Fig. 3.13. We observe the same power-law dependence of the scaling factor $L(t)$ as discussed before for all temperatures. With decreasing temperature, the coarsening process slows down, which agrees with Allen and Cahn (1979), Weinkamer et al. (1998), and Kessler, Dieterich, and Majhofer (2003b). The obtained growth rates

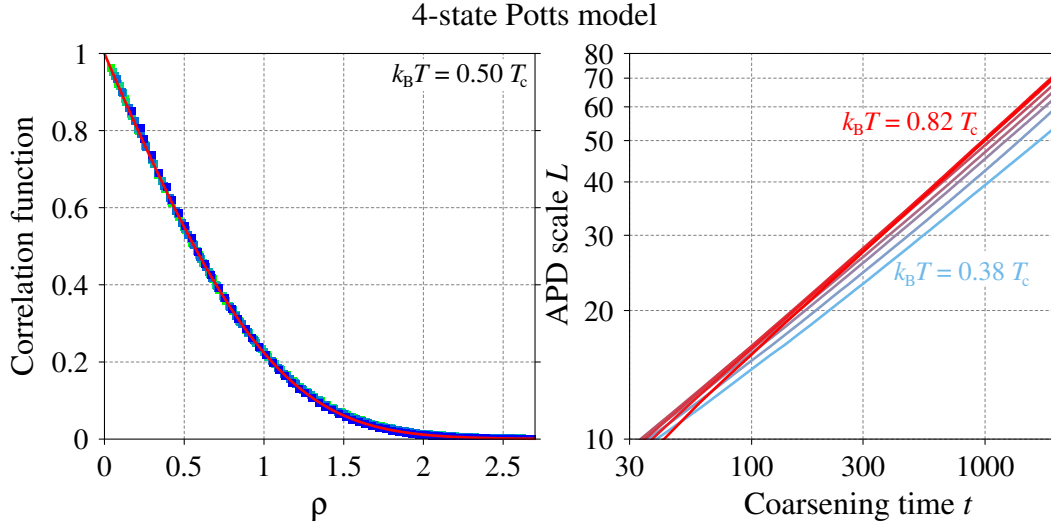


Figure 3.13: The scaled real-space correlation function of the 4-state Potts model at a simulation temperature of $0.5T_c$ at 100 MCS, 600 MCS, 800 MCS, 1200 MCS and 2000 MCS, plotted together with the respective scaling function (in red). The size of the system is $N = 250$. On the right the growth of the characteristic length scales L with time for various simulation temperatures are shown.

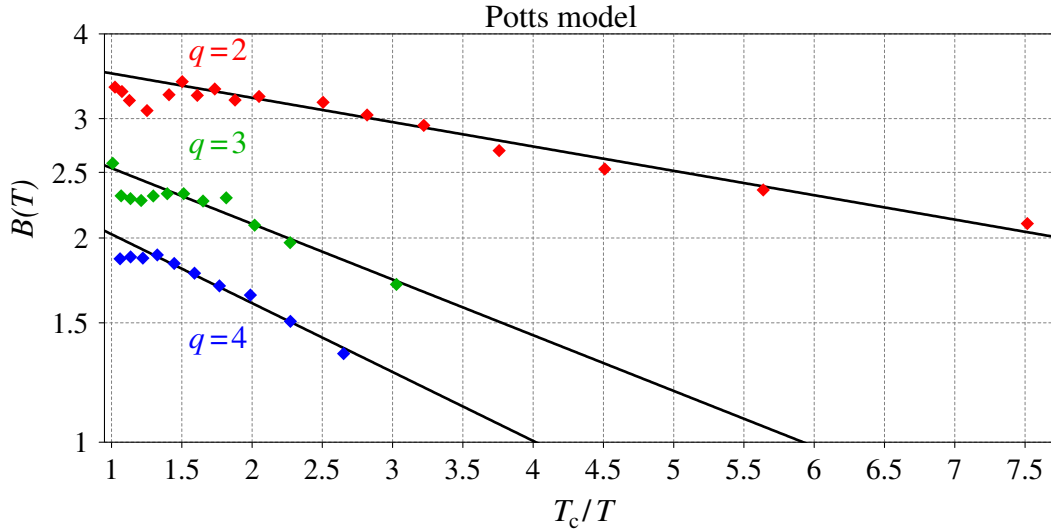


Figure 3.14: Growth rates $B(T)$ of the characteristic length scales L with time for the q -state Potts model at various simulation temperatures, plotted together with lines indicating the Arrhenius behaviours $-\ln(B(T)) \propto T_c/T$.

are shown for all Potts systems in Fig. 3.14. The thermal evolution of $B(T)$ follows for all q -state Potts models the expected Arrhenius-type behaviour. However, with increasing q , the influence of the simulation temperature on the coarsening process increases, which can be best observed when comparing the temperature-dependence of the $q = 4$ to the $q = 2$ Potts system. This behaviour can be explained by considering, once again, the increasing number of neighbouring domains: as mentioned before, the APBs forms corners for the $q \geq 4$ Pott system. At low temperatures, the probability of an unfavourable exchange is small, hence at a corner, with three favourable and three unfavourable bonds (on sc lattice), the coarsening process becomes very slow since there is no favourable exchange. In contrast, the coarsening process slows down the $q = 2$ Potts system due to the decreased probability of exchange but can not become stuck. Hence, we observe for the $q = 2$ only a small decrease of the growth rate over a large temperature range.

3.5.3 Measures of Domain Size

The size of an APD is ill-defined when it is percolating in three dimensions and, thereby, has an infinite volume. As such behaviour becomes relevant for not too large values of q , more appropriate descriptions of APD scales are required. In this chapter we consider the specific interface area (interfacial density) which determines the average area of interface per unit volume.

In the following, we derive what measure of real-space APD scale the respective scaling parameter L corresponds to under the assumption of large domains and small distances. Our definition of the scaling function implies that its derivative approaches -1 for small distances. To understand the implications of this assumption, we consider the following scenario: in a three dimensional APD configuration with a specific interfacial area ξ we consider two points A and B, which are randomly located in three dimensional space and separated by a distance r . In case of large domains and small distances the interface separating two domains can be regarded as flat. If these interfaces were oriented perfectly perpendicular to the vector connecting A to B (corresponding to the one dimensional scenario of an APD configuration), then the probability of this vector to pass through one interface would be equal to ξr in the limit of small r . In case of an arbitrary direction of \mathbf{r} in three dimensional space, the two points A and B are located at random positions in space. Hence the projection of their connecting vector \mathbf{r} along the boundary plane direction vector is needed. The mean absolute value of a randomly oriented three dimensional unit vector's projection along a given direction corresponds to the value $1/2$. Thus, in this limit,

the probability for A and B to be in the same domain, which is nothing else than the (unscaled) correlation function $g'(r)$, is given by

$$g'(r) \approx 1 - \xi r/2. \quad (3.18)$$

As a consequence, with Eqs. (3.7) and (3.12) the scaling parameter L that leads to $g(\rho)$ having a derivative of -1 at $\rho = 0$ fulfills

$$L = 2/\xi. \quad (3.19)$$

Per definition, our APD scale L is exactly equivalent to the measure obtained via the linear intercept method (Smith and Guttman, 1953). This analysis technique is commonly used in real space methods like Transmission Electron Spectroscopy (TEM) (Rogers, Flower, and Rawlings, 1975; Suzuki, Takeyama, and Matsuo, 2002; Brenker, Müller, and Brey, 2003). As mentioned in the introduction of this chapter, here, the APD scale is determined by counting the number of intersections N_i along a line segment of random direction with length l in the image plane. The mean distance between the intersection N_i/l is related to the APB density S/V , when assuming isotropic APD configurations (Smith and Guttman, 1953), analogously to our scale.

When studying the APD scale via reciprocal-space methods, like powder diffraction, the finite correlation length of the superstructure, whose correspondingly ordered domains we assume to scatter coherently, results in a broadening of the respective Bragg peaks. The most basic approach to obtain the APD scale is the Scherrer equation (Scherrer, 1918). It relates the diffraction-peak's width Δk in units of the wave-vector transfer to the scale \bar{D} of real-space features and is defined as

$$\bar{D} = \frac{2\pi K}{\Delta k}. \quad (3.20)$$

In this simple form, contributions to the broadening such as strain or instrument broadening are neglected. K is the so-called Scherrer constant and is influenced by the shape of the real-space features, the crystallographic direction, the shape of the diffraction peak profile, the definition of the profile width and the size distribution of the domains (Langford and Wilson, 1978). Due to this complexity, the observation that the Scherrer constant is usually close to unity and the fact that, in most cases, the actual domain shape is either unknown or ill-defined, it has become common practice to use an "overall average" shape factor, which is set to unity (e.g., Ref. Gilles et al. (2010)). In particular, assuming monodisperse spherical domains of the volume \bar{D}^3 in

real space, which is the most basic choice for the case of powders or polycrystals, and determining Δk as the FWHM of the peak implies $K_{\text{FWHM}} \approx 0.8920$ (Patterson, 1939). However, if instead the integral breadth is used to determine \bar{D} , one has to consider $K_{\text{I}} = \sqrt[3]{32\pi/81} = 1.0747$ (Langford and Wilson, 1978). We have shown that there exists a universal scaling function for a given q , whose respective FWHM and integral breadth are given in Tab. 3.2. Hence, we can relate scales determined by microscopy and diffraction quite easily, without having to consider a detailed phenomenological model in terms of distribution functions (Sauthoff, 1973; Leoni and Scardi, 2004).

Specifically, if the APD scale is assumed to be $\bar{D} = L = 2/\xi$ in Eq. (3.20), we obtain for the $q = 2$ Potts model the Scherrer constants $K_{\text{FWHM}} = 1.2916$ and $K_{\text{I}} = 1.6275$. The rescaling factor $2(q-1)/q$ relates the derivative of the rescaled pair-correlation function $g(r)$ to the APB density ξ . With increasing q , its contribution becomes dominant for the behaviour of K , while the specific shape of the scaling function is of only secondary importance for increasing q , leading to $K_{\text{FWHM}} = 0.7908$ and $K_{\text{I}} = 1.0195$ for the $q = 4$ Potts case. In particular, if we consider a system of spheres with radius 1 which fill the complete volume of the system, the respective interface area density ξ would be given as $S/2V = 3/2$ (Glatter and Kratky, 1982). Hence the ratio of the scale defined by L and \bar{D} is $\sqrt[3]{16/9\pi} \approx 0.8271$. Therefore, if the specific definitions of the spatial scale \bar{D} are taken into account, we obtain a satisfactory approximation of the polycrystalline case ($q = \infty$) if the Scherrer constants are set to unity. However, for the low q case this approximation would lead to a drastic overestimation of the specific interface area.

3.6 Conclusion

In this chapter, the coarsening process in symmetric and asymmetric binary compounds (AB) was investigated via large-scale Monte Carlo simulations. We considered microscopically realistic models (Ising model) and an abstract approach using the Potts model to study the atomic ordering process in these systems.

We proposed an analytical expression for the real-space and reciprocal-space scaling functions. We obtained parameters for all realistic relevant cases $q = 2, 3$, and 4 , which give a very good fit of the simulation results. Using this model, we found that systems of the same ground-state degeneracy q bear closer a resemblance than systems of different q , independent of the underlying model. This result upholds our hypothesis of an universal scaling function describing the pair-correlation functions and structure factors of a system with a distinct ground-state degeneracy q .

Introducing the scaling parameter $L(t)$, a real-space scale proportional to the interface density, we studied the growth of the APDs and found the characteristic length scales of each system obeying the power-law dependence on time. Finally, we compared our APD scale to the evaluation methods commonly used in experiments. With our scaling parameter being essentially the inverse of the specific interface area, it is equivalent to the measure obtained via the linear intercept method in microscopy. Hence, with our scaling function, it is possible to relate, quantitatively, scales obtained via microscopy to those measured using the broadening of Bragg peaks in diffraction without any adjustable parameters.

In the following chapter, we apply this new scaling function of the $q = 2$ model to investigate the extent of $L2_1$ order in Ni_2MnZ alloys and, thereby, to obtain the APD scale from scattering experiments.

Chapter 4

Correlation of Structural and Magnetic Domains

4.1 Influence of Structural Order on the Magnetic Properties of Ni_2MnZ Heusler Alloys

In Chapter 3 the coarsening process of three-dimensional anti-phase domain structures was investigated. As mentioned before, structural order has a large influence in the development of system properties such as magnetism or yield strength, for example in superalloys (e.g. Ni_3Al (Stoloff, 1984)), superconductors (e.g. SrFe_2As_2 (Jesche et al., 2008)) and functional materials such as $\text{Gd}_5\text{Si}_2\text{Ge}_2$ (Pecharsky and Gschneidner, 1997) or the Heusler alloys (Acet et al., 2002; Neibecker et al., 2017).

Specifically in Ni_2MnZ Heusler compounds, the atomic order of the austenite phase plays a crucial role in their magnetic properties. Here the magnetic moments are mainly carried by the Mn atoms, whose exchange interaction depends strongly on the distance between them as in many other compounds with a sufficiently high concentration of Mn (Acet et al., 2002; Kwiatkowski et al., 2007). Their exchange interaction is dominated by the coupling between the Ni-Mn as well as the Mn-Mn pairs, as sketched in Fig. 4.1. Here we assume the magnetic moments of Ni to be induced by their surrounding Mn moments (Ležaić et al., 2013; Simon et al., 2015). The interaction between Ni-Mn pairs is ferromagnetic, while the exchange between Mn-Mn pairs is anti-ferromagnetic. In the case of a fully L_{21} ordered structure, as displayed in Fig. 4.1, direct Mn-Mn pairs no longer exist in the system. Hence the exchange interaction consists only of the ferromagnetic Ni-Mn interaction, resulting

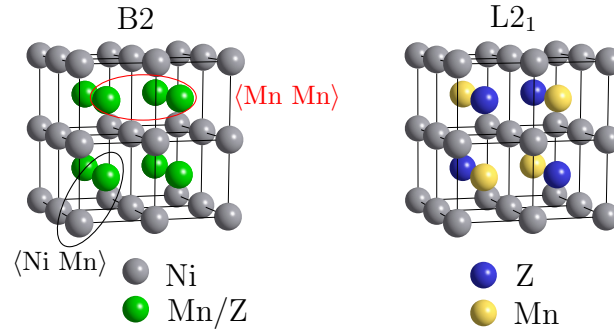


Figure 4.1: Sketch of the ordering states of Ni_2MnZ on the bcc lattice with their corresponding magnetic exchange interaction: In B2 order magnetic exchange interactions have to be considered between Ni-Mn pairs as well as Mn-Mn pairs as sketched by the two ellipses. In L2_1 order direct Mn-Mn pairs do not exist, therefore only the coupling of the Ni-Mn spins has to be considered.

in the ferromagnetic properties of a fully L2_1 ordered Ni_2MnZ compound (Kreissl et al., 2003). Yet, in the B2 ordered structure the Mn-Z sublattice is in disorder, resulting in direct Mn-Mn pairs as well as the induced Ni moments to be zero (Simon et al., 2015). Therefore the overall magnetic properties found in a B2 ordered Ni_2MnZ compound are anti-ferromagnetic (Acet et al., 2002). However, the atomic disorder leads to a local competition between the anti-ferromagnetic as well as ferromagnetic exchange interactions where locally non-collinear magnetic structures can exist (Acet et al., 2002). Due to this competition, the magnetic structure of intermediate ordering states of the B2- L2_1 -transition is complicated with a non-trivial transition between anti-ferromagnetic to ferromagnetic order.

The simplest model for the magnetic exchange interactions in Ni_2MnZ compounds is to assume that the spins of the next nearest neighbour Mn atoms couple ferromagnetically due to the mediation by the Ni atoms, while neighbouring Mn spins couple anti-ferromagnetically. If we apply this interaction model to a B2 ordered state, as sketched in Fig. 4.2, the system would exhibit anti-ferromagnetic properties since here direct Mn-Mn pairs exist and dominate the structure. However, this model leads to ferromagnetic properties in a fully L2_1 ordered crystal, as no Mn-Mn pairs are left in the system. For intermediate states of L2_1 order, we would expect, according to this argumentation, a reversal of magnetisation when crossing an APD boundary, as sketched in Fig. 4.2. The neighbouring Mn spins located at the domain interface would align anti-parallel, while the next nearest neighbour Mn spins inside the APD couple ferromagnetically. Hence, the direction of the magnetisation of an APD would be given by the Mn spins at the APD boundary. Using TEM and

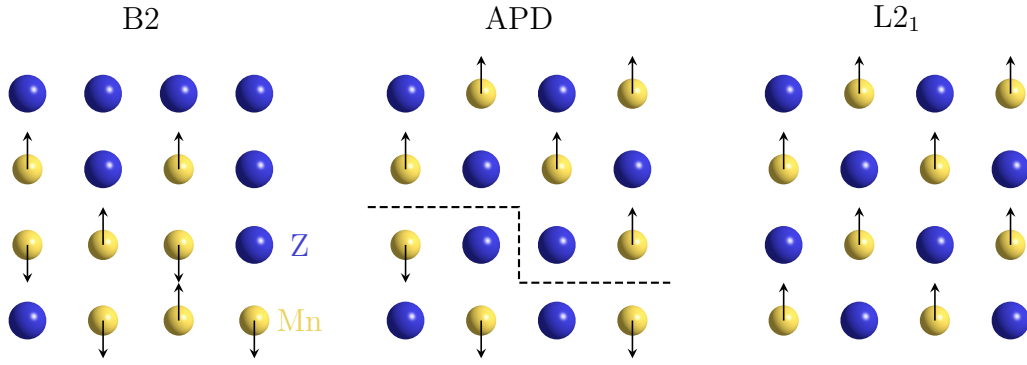


Figure 4.2: Sketch of the magnetic exchange interaction in Ni_2MnZ compounds in the plane of the Mn-Z sublattice: in B2 order the Mn-Z sublattice is disordered resulting in direct MnMn pairs whose spins align antiparallel to each other. In the intermediate ordering state an the structurally ordered domains are separated by an APB (dashed line), the spins located at the APB align antiparallel to each other, leading to an antiparallel alignment of the APD to each other. In L2_1 order no direct MnMn pairs are present, therefore the spins align parallel to each other.

Lorentz TEM the magnetisation has indeed been observed to reverse at structural APB boundaries in $\text{Ni}_2\text{MnAl}_{0.5}\text{Ga}_{0.5}$ samples, implying that structural and magnetic domains are identical (Yano et al., 2007; Ishikawa et al., 2008). Also, the width of the magnetic domain walls in these systems is unusually thin, about 10 nm (Yano et al., 2007). The magnetic properties of these systems are therefore strongly dependent on the microstructure, with anti-ferromagnetic and ferromagnetic exchange interactions being present (Neibecker et al., 2017).

The size of structurally ordered domains can be accessed either by real-space methods, e.g. electron microscopy (Murakami et al., 2006; Venkateswaran, Nuhfer, and De Graef, 2007; Yano et al., 2007; Murakami et al., 2011), or by diffraction methods in reciprocal space. An appropriate way to evaluate the length scale of structurally ordered domains is to measure the APB density, as it is commonly done in microscopy experiments (Rogers, Flower, and Rawlings, 1975; Suzuki, Takeyama, and Matsuo, 2002; Brenker, Müller, and Brey, 2003) via the linear intercept method (Smith and Guttman, 1953). In diffraction experiments, the finite size of the correlation length of L2_1 order results in a broadening of the corresponding superstructure peaks. Its respective length scale is directly linked to the peak's FWHM via the Scherrer equation (Scherrer, 1918).

In contrast to diffraction experiments, which are mostly used to probe the atomic structure of a sample, small-angle neutron scattering is sensitive to structures of the mesoscopic length scale (Mühlbauer et al., 2019). Due to the neutron's magnetic

moment, which couples to the local internal magnetic field from the magnetic atoms in the sample, the contrast between local magnetic fields can be probed and the corresponding magnetic microstructure can be investigated via small angle neutron scattering (SANS) experiments (Bhatti et al., 2012; El-Khatib et al., 2019).

In Ni_2MnGa , the B2 structure transforms within seconds to the full-Heusler structure (Overholser, Wuttig, and Neumann, 1999), whereas Ni_2MnAl shows, in general, a low $L2_1$ order tendency (Ziebeck and Webster, 1975; Acet et al., 2002). In contrast to these ternary compositions, the quaternary compound $\text{Ni}_2\text{MnAl}_{0.5}\text{Ga}_{0.5}$ can be obtained in the B2 state by quenching a crystal from the B2-stable regime to room temperature as well as large APDs can be achieved by low-temperature annealing quenched crystals in the $L2_1$ -stable regime (Ishikawa et al., 2008; Umetsu et al., 2011).

To study the interplay of magnetic and structural order as well as the mechanism of coupling of ferromagnetic domains across APD boundaries, we have applied neutron powder diffraction as well as small-angle neutron scattering (SANS) to investigate the structural and the magnetic microstructure, respectively, of $\text{Ni}_2\text{MnAl}_{0.5}\text{Ga}_{0.5}$ and Ni_2MnAl powder samples in distinct $L2_1$ ordering states. The powder diffraction data presented in this chapter were collected and partially published by P. Neibecker in Neibecker (2017). P. Chiu gathered the SANS data, partially analysed and presented them in Chiu (2017). Using the phenomenological model derived in the previous chapter, the diffraction data were analysed by the author and connected to the SANS data. The results of this chapter have been partially published in an article (Zweck et al., n.d.).

4.2 Sample Preparation

Polycrystalline Ni_2MnAl and $\text{Ni}_2\text{MnAl}_{0.5}\text{Ga}_{0.5}$ ingots were prepared by induction melting stoichiometric amounts of the constituting high purity elements and tilt or suction casting in Ar atmosphere. In order to promote homogeneity and to remove segregation effects from casting, the ingots underwent a solution annealing treatment and were subsequently water quenched. The exact compositions of the ingots were determined via Energy-Dispersive X-Ray Spectroscopy (EDS) at the Staatliche Materialprüfamt für Maschinenbau at the Technical University of Munich, Germany. For each alloy ten randomly selected positions were studied. The average over these values are given in Tab. 4.1 and show a satisfactory agreement with the nominal compositions stoichiometry.

Compound at.%(±0.5 %)	Ni	Mn	Al	Ga
$\text{Ni}_2\text{MnAl}_{0.5}\text{Ga}_{0.5}$	51.1	26.0	11.2	11.7
Ni_2MnAl	49.2	25.6	25.2	-

Table 4.1: Actual composition of the Ni_2MnAl and $\text{Ni}_2\text{MnAl}_{0.5}\text{Ga}_{0.5}$ ingots measured via EDS.

The ingots were ground to powder of grind size $<125\text{ }\mu\text{m}$. In order to release mechanical stresses and strains introduced by the grinding process the samples were subsequently annealed in evacuated quartz ampules at $T_q = 1073\text{ K}$, corresponding to the B2 stable regime, for 4 h and water quenched. To obtain distinct states of L2_1 order the powder samples underwent a low temperature annealing treatment in the L2_1 stable regime at $T_a = 623\text{ K}$. We investigated in total four $\text{Ni}_2\text{MnAl}_{0.5}\text{Ga}_{0.5}$ samples and three Ni_2MnAl samples, with the $\text{Ni}_2\text{MnAl}_{0.5}\text{Ga}_{0.5}$ samples being annealed for $t_a = 0.5\text{ h}$, 3 h and 10 d , and the Ni_2MnAl samples for 24 h and 10 d , respectively. For both compositions an as-quenched (a. q.) sample was retained.

To determine the magnetic transition temperatures T_c of the samples Differential Scanning Calorimetry (DSC) measurements were performed with heating rates of 10 K min^{-1} between 250 K and 400 K . In order to check if the grinding process had any influence on the magnetic properties of the samples corresponding bulk samples were prepared. While annealing these bulk samples at 623 K DSC measurements were performed for consecutive timesteps. The curves of the respective bulk samples show a sharp transition between the magnetic and paramagnetic phase, while the DSC data of the corresponding powder samples are in general broader with the transition being less distinctive due to the inhomogeneities of the powder grain. Fig. 4.3 shows the DSC curves of the Ni_2MnAl 24 h annealed bulk and powder sample, where we observe the curve of the bulk sample to be more distinctive compared to the powder sample. In order to retrieve the magnetic transition temperature from these less distinctive curves the data were convoluted with a centered Gaussian kernel. The position of the transition was identified as the position with the maximum negative gradient. The evolution of the corresponding transition temperatures with annealing time is shown in Fig. 4.4, where we observe a positive correlation between both parameters for both alloy families, as it has been reported for Ni_2MnAl bulk samples by Neibecker et al. (2014).

When comparing between the alloy families the low ordering tendency of Ni_2MnAl becomes clear, with its T_c evolution being slower than the one of $\text{Ni}_2\text{MnAl}_{0.5}\text{Ga}_{0.5}$. For Ni_2MnAl we observe an excellent agreement between the bulk and the powder

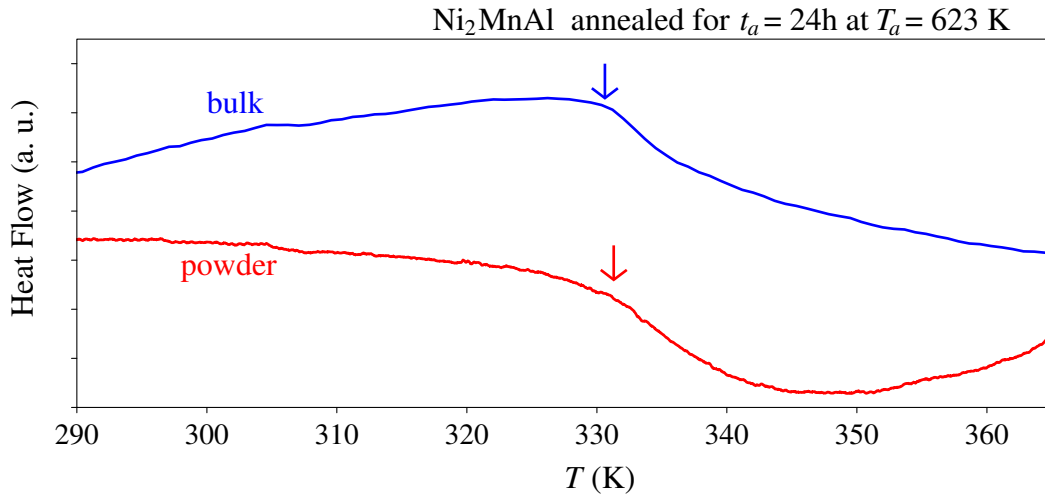


Figure 4.3: DSC measurements of the magnetic transition in Ni_2MnAl 24 h annealed for powder and bulk samples. Measurements have been performed on heating using a heating rate of 10 K min^{-1} . The respective T_c is indicated by the arrows and has been determined as the position of the maximum negative gradient.

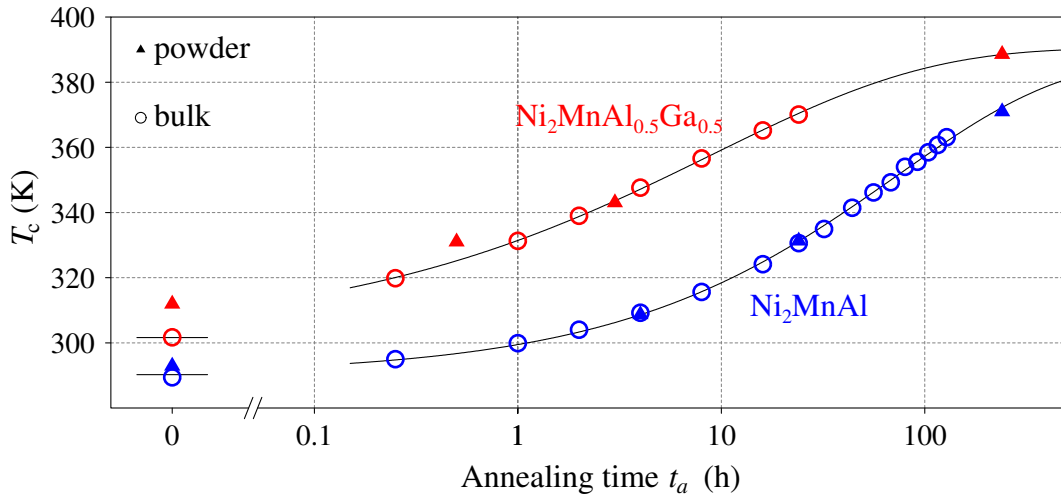


Figure 4.4: Evolution of the magnetic transition temperature extracted from the DSC measurements as function of annealing time t_a at $T_a = 623\text{ K}$ for the Ni_2MnAl and $\text{Ni}_2\text{MnAl}_{0.5}\text{Ga}_{0.5}$ powder and bulk samples. The black line serves as a guide for the eyes.

samples, while for $\text{Ni}_2\text{MnAl}_{0.5}\text{Ga}_{0.5}$ the results show a satisfactory agreement, with the results of the bulk samples being in general lower than for the powder samples. This deviation results most likely from the phenomenological determination of the transition temperature due to the broadened DSC curves of the powder samples, as shown in Fig. 4.3. For the bulk samples the transition is so distinctive that this phenomenological determination does not affect the resulting T_c -value.

4.3 Neutron Powder Diffraction

4.3.1 The Time-of-Flight Spectrometer POWGEN

We employed neutron powder diffraction measurements to study structural as well as magnetic order in intermetallic compounds. The experiments were carried out at the time-of-flight (TOF) diffractometer POWGEN, located at the Spallation Neutron Source (SNS) in Oak Ridge. The setup of the instrument is sketched in figure 4.5.

At SNS neutrons are produced in pulses by high energy protons hitting a target of liquid mercury, where spallation occurs. Here the protons are momentarily incorporated in the nuclei of the heavy atoms, transferring their energy to single nucleons, which results in an internal nucleon cascade within the excited mercury nucleus. This internal cascade is followed by an internuclear cascade when high energy particles including neutrons are ejected and absorbed by other nuclei. The charged protons will be stopped within the target, while many lower-energy neutrons and a variety of nucleons, photons and neutrinos are emitted and can be subsequently used. The pulses are emitted at a frequency f and contain white neutrons. The neutron bunch is scattered on a sample, as sketched in Fig. 4.5, and travels a fixed distance L from the source to the instrument detector, with faster neutrons of a shorter wavelength

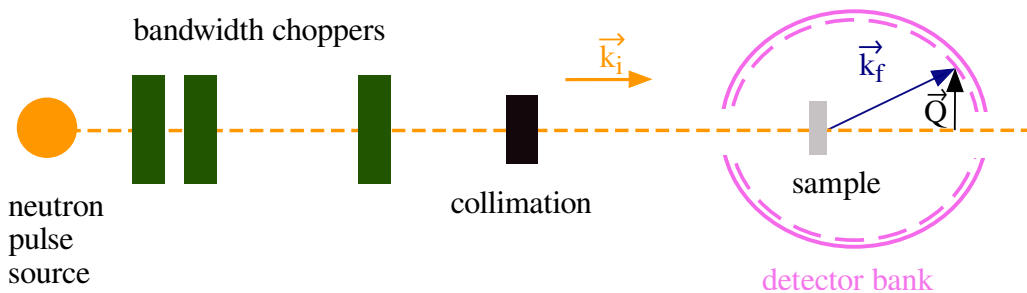


Figure 4.5: Sketch of the setup of the instrument POWGEN with a polychromatic neutron beam at SNS, Oak Ridge.

needing less flight time than slower neutrons with a larger wavelength. The path length L varies depending on the position of the detector bank. If solely neutrons from a single pulse, without any frame-overlap, are detected, one can determine the wavelength λ of the scattered neutron by measuring its time-of-flight t . The combination of Bragg's law and de Broglie's equation leads to the following proportionality between the wavelength and t :

$$\lambda = \frac{ht}{m_N L} \quad (4.1)$$

where h is the Planck constant, m_N is the mass of the neutron and L is the total flight path length. The neutrons' wavelength is inverse proportional to the wavevector transfer Q which is given by Bragg's equation as

$$Q = \frac{4\pi}{\lambda} \sin \theta \quad (4.2)$$

with θ being the scattering angle.

To avoid a frame-overlap of very fast or very slow neutrons leaking into other pulses, the incoming neutron pulse has to pass three bandwidth choppers before hitting the sample (Huq et al., 2015a). This chopper system sets the center frequency f_c as well as the bandwidth $\Delta\lambda$, which is chosen in order to prohibit frame-overlap. The bandwidth depends on the distance between the source and the detector as well as on the pulse frequency and is given according to Willis and Carlile (2009) as

$$\Delta\lambda = \frac{h}{m_N} = \frac{3956 \frac{\text{\AA m}}{\text{s}}}{Lf}. \quad (4.3)$$

For POWGEN the source-detector distance L varies between 62.5 m and 64.7 m depending on the specific detector position in the detector bank (Huq et al., 2015a). With the pulse source operating with a repetition rate $f = 60$ Hz, the maximum bandwidth one can record without eliminating whole neutron pulses is $\Delta\lambda = 1.066 \text{ \AA}$ (Huq et al., 2015a). In this thesis measurements at two different center wavelengths, $\lambda_c = 1.333 \text{ \AA}$ and $\lambda_c = 2.665 \text{ \AA}$, were performed. The corresponding wavelength $[\lambda_{\min}, \lambda_{\max}]$ as well as wavevector transfer ranges $[Q_{\min}, Q_{\max}]$ are listed in Tab. 4.2.

An expression for the resolution function R of the instrument can be obtained by taking the partial derivatives of equation 4.1 (Willis and Carlile, 2009)

$$R = \left(\frac{\Delta Q}{Q} \right)^2 = \left(\frac{\Delta d}{d} \right)^2 = \left(\frac{\Delta t}{t} \right)^2 + \left(\frac{\Delta L}{L} \right)^2 + \left(\frac{\Delta \theta \cos \theta}{\sin \theta} \right)^2. \quad (4.4)$$

$\lambda_c(\text{\AA})$	$\lambda_{\min}(\text{\AA})$	$\lambda_{\max}(\text{\AA})$	$Q_{\min}(\text{\AA}^{-1})$	$Q_{\max}(\text{\AA}^{-1})$
1.333	0.800	1.866	1.0239	15.1700
2.665	2.132	3.198	0.5975	5.6923

Table 4.2: Center wavelengths and their corresponding wavelength at POWGEN used for the measurements presented in this thesis. The accessible angle range 2θ is from 17.5° to 150° .

The maximum resolution for POWGEN is $\Delta d/d = 0.0015$ for $d = 1 \text{ \AA}$ (Huq et al., 2015b).

4.3.2 Neutron Scattering Theory

In order to interpret the neutron data obtained from scattering processes of large structural as well as magnetic domains the fundamental interactions of neutrons and matter will be revised in this section.

4.3.2.1 Neutron Interactions with Matter

The neutron is an uncharged particle which interact through short-range nuclear interactions. The scattering process of neutrons with nuclei is a quantum mechanical process and has to be described in terms of wavefunctions. The wave properties of the neutron and its interaction with matter given by the interaction potential $V(\mathbf{r})$ are described by the stationary Schrödinger Equation

$$E\Psi(\mathbf{r}) = \left[-\frac{\hbar^2 \Delta}{2m} + V(\mathbf{r}) \right] \Psi(\mathbf{r}). \quad (4.5)$$

which is a scalar wave equation for the wavefunction Ψ of a particle with energy E and mass m . \hbar denotes the reduced Planck constant. The neutron couples via the strong nuclear force interaction V_{nuc} to the nuclei which can be well described for low energy neutrons by point like Fermi pseudo potentials at the positions \mathbf{r}_i

$$V_{\text{nuc}}(\mathbf{r}) = \frac{2\pi\hbar^2}{m} \sum_{i=1}^N b_i \delta(\mathbf{r}_i) \quad (4.6)$$

where the nuclei are located at the positions \mathbf{r}_i and have the scattering lengths b_i (Squires, 2012). This approximation of the strong force interaction potential is valid for thermal and cold neutrons where the wavelength of the neutron is much larger than the range of the interaction.

Also the magnetic structure of a sample can be investigated via neutron scattering, since the neutron has a magnetic dipole moment $\boldsymbol{\mu}$, which couples to the internal or external local magnetic field \mathbf{B} . Its interaction $V_{\text{mag}}(\mathbf{r})$ is expressed by the Zeeman equation (Squires, 2012)

$$V_{\text{mag}}(\mathbf{r}) = -\boldsymbol{\mu} \cdot \mathbf{B}(\mathbf{r}). \quad (4.7)$$

The neutrons are either absorbed by, reflected by, or scattered off the sample via the nuclear and magnetic interactions. Due to their weak interaction potential other interactions, such as gravitational forces, can be neglected in most cases.

4.3.2.2 Scattering Process

In the simplest case the incident neutron beam can be represented by a plane wavefunction in z -direction $\Psi_i(k) = \exp(ikz)$, which is the solution of the Schrödinger equation in free space ($V = 0$) with k being the wavevector. When this plane wave is scattered at a single nucleus located at the origin with a scattering length b , the wavefunction of the scattered neutrons can be written as a spherical wavefunction $\Psi_f(k) = -\frac{b}{r} \exp(ikr)$, since the scattering is spherically symmetric.

In case of scattering off an arbitrary structure, which contains more than one single nucleus and is defined by a non-zero interaction potential $V(\mathbf{r})$, the scattered neutron wavefunction is given by the Lippmann-Schwinger equation (Squires, 2012):

$$\Psi_f(\mathbf{r}) = \Psi_i(\mathbf{r}) - \frac{m}{2\pi\hbar^2} \int \frac{\exp(i\mathbf{k}_f|\mathbf{r} - \mathbf{R}|)}{|\mathbf{r} - \mathbf{R}|} V(\mathbf{R}) \Psi_f(\mathbf{R}) d\mathbf{R} \quad (4.8)$$

where \mathbf{R} is within the sample, while \mathbf{r} is far from it. Hence we can assume $r \gg R$ and therefore approximate $|\mathbf{r} - \mathbf{R}| \simeq r - \mathbf{r} \cdot \mathbf{R}/r$. This equation is solved iteratively by inserting $\Psi_f(\mathbf{r})$ on the right hand side starting with the neutron's initial state $\Psi_i(\mathbf{r})$, the plane wavefunction. In most scattering experiments the dimensions of the sample are chosen in a way that multiple scattering events can be neglected, hence the wavefunction of the outgoing neutron is given by the solution after the first iteration. This corresponds to the first Born approximation and holds for scattering with thermal and cold neutrons. For $|\mathbf{r}| \gg |\mathbf{R}|$ the wavefunction of the scattered neutron can be approximated as a superposition of the incident wave and a spherical wave weighted by the Fourier transform of the interaction potential,

$$\Psi_f(\mathbf{r}) = \exp(i\mathbf{k}_i \cdot \mathbf{r}) + \frac{\exp(i\mathbf{k}_f \cdot \mathbf{r})}{r} \int V(\mathbf{R}) \exp(i\mathbf{Q} \cdot \mathbf{R}) d\mathbf{R}. \quad (4.9)$$

The Fourier transform of the interaction potential is also known as the scattering amplitude $f(\mathbf{Q})$ which depends on the momentum transfer $\mathbf{Q} = \mathbf{k}_f - \mathbf{k}_i$ of the neutron.

In a scattering experiment the number of neutrons scattered from the sample in the solid angle $d\Omega$ normalized to the incident neutron flux Φ is measured. The incident flux is defined as the number of particles per time that go through an area normal to the beam direction. The intensity scattered in Ω is called the differential scattering cross-section $d\sigma/d\Omega$ and is given by the squared scattering amplitude $|f(\mathbf{Q})|^2$ (Squires, 2012). The total scattering cross-section σ_{tot} is obtained by integration over all solid angles. For the simple case of neutrons being scattered off a single fixed nucleus the total cross-section is given as $\sigma_{\text{tot}} = 4\pi b^2$ (Squires, 2012).

Scattering neutrons on a regular arrangement of nuclei will result in a regular scattering pattern. For purely nuclear scattering this pattern can be approximated by the squared Fourier transform of a sum of Fermi pseudo potentials (Eq. (4.6)) located at the nuclei equilibrium positions \mathbf{r}_i

$$\frac{d\sigma}{d\Omega} = \sum_{j=1}^N \sum_{i=1}^N b_i b_j \exp(i\mathbf{Q} \cdot (\mathbf{R}_i - \mathbf{R}_j)). \quad (4.10)$$

In reality the scattering lengths of the nuclei in a material differ, either because of different spin configurations or different isotopes located at \mathbf{r}_i . Hence the scattering length of one atom can be written as a linear combination of its average scattering length \bar{b} and its specific deviation from it δb_i , $b_i = \bar{b} + \delta b_i$. Eq. (4.10) transforms to

$$\begin{aligned} \frac{d\sigma}{d\Omega} &= \sum_{j=1}^N \sum_{i=1}^N (\bar{b} + \delta b_i)(\bar{b} + \delta b_j) \exp(i\mathbf{Q} \cdot (\mathbf{R}_i - \mathbf{R}_j)) \\ &= \bar{b}^2 \sum_{j=1}^N \sum_{i=1}^N \exp(i\mathbf{Q} \cdot (\mathbf{R}_i - \mathbf{R}_j)) + \sum_{j=1}^N \sum_{i=1}^N \delta b_i \delta b_j \exp(i\mathbf{Q} \cdot (\mathbf{R}_i - \mathbf{R}_j)) \\ &\quad + 2\bar{b} \sum_{j=1}^N \sum_{i=1}^N \delta b_i \exp(i\mathbf{Q} \cdot (\mathbf{R}_i - \mathbf{R}_j)). \end{aligned}$$

Due to the definition of the center of mass — $\sum_{i=1}^N \delta b_i = 0$ — the last term can be neglected. Thus the scattering pattern can be split into a coherent part $\propto \bar{b}$, corresponding to the correlation between the positions of different nuclei, and an incoherent part, which is due to the random distribution of the deviations of the

scattering lengths from their mean value, and is given by (Squires, 2012)

$$\frac{d\sigma}{d\Omega} = \bar{b}^2 \sum_{i,j=1} \langle \exp(i\mathbf{Q} \cdot (\mathbf{R}_i - \mathbf{R}_j)) \rangle + \sum_{i,j} (\delta b_j)^2. \quad (4.11)$$

with $\langle \dots \rangle$ being the ensemble average.

4.3.2.3 Elastic Coherent Scattering Cross-Section

The intensity detected by a neutron powder diffractometer has four main contributions: elastic coherent, elastic incoherent, inelastic coherent and inelastic incoherent scattering. For the samples studied in this thesis, which are all powder samples of cubic crystal structures, the elastic coherent scattering is responsible for the defining features of the powder diffractogram, i.e., the positions, shapes and intensities of the Bragg peaks.

First we consider the nuclear scattering by a crystal whose unit cell contains more than one atom. The differential scattering cross-section results from the Fermi pseudo-potentials Eq. (4.6) and its general expression is given according to Squires (2012) as

$$\left(\frac{d\sigma}{d\Omega} \right)_{\text{coh,el}} = |f(\mathbf{Q})|^2 = (\bar{b})^2 N \exp(-2W(\mathbf{Q})) \sum_{\mathbf{d}} \exp(i\mathbf{Q} \cdot \mathbf{d}), \quad (4.12)$$

where N is the number of unit cells in the scattering volume and \mathbf{d} denotes the position of the nucleus in equilibrium. The exponential term $\exp(-2W(\mathbf{Q}))$ is known as the Debye-Waller factor, with the exponent coefficient $W(\mathbf{Q})$ corresponding to the mean-square displacement $Q^2 \langle u_Q^2 \rangle$ in the direction of \mathbf{Q} of the atoms in the crystal. For a cubic crystal \mathbf{u} is independent of the direction, thus we can express the direction dependent displacements u_Q by their mean value:

$$\langle u_x^2 \rangle = \langle u_y^2 \rangle = \langle u_z^2 \rangle = \frac{1}{3} \langle u^2 \rangle \quad (4.13)$$

Therefore, $W(\mathbf{Q})$ can be expressed as $W(\mathbf{Q}) = \frac{1}{6} Q^2 \langle u^2 \rangle$.

For scattering on a lattice the sum of exponential functions can be written as the sum of δ functions, $\sum_{\mathbf{d}} \exp(i\mathbf{Q} \cdot \mathbf{d}) = \frac{(2\pi)^3}{v_0} \sum_{\boldsymbol{\tau}} \delta(\mathbf{Q} - \boldsymbol{\tau})$, with v_0 being the volume of the unit cell of the crystal and $\boldsymbol{\tau}$ being a vector in the reciprocal lattice (Squires, 2012). Thus Eq. (4.12) can be written as

$$\left(\frac{d\sigma}{d\Omega} \right)_{\text{coh,el}} = N \frac{(2\pi)^3}{v_0} \exp(-2W(\mathbf{Q})) \sum_{\boldsymbol{\tau}} |S_{\text{nuc}}(\mathbf{Q})|^2 \delta(\mathbf{Q} - \boldsymbol{\tau}), \quad (4.14)$$

with the nuclear unit cell structure factor

$$S_{\text{nuc}}(\mathbf{Q}) = \sum_{\mathbf{d}} \bar{b}_{\mathbf{d}} \exp(i\mathbf{Q} \cdot \mathbf{d}), \quad (4.15)$$

where \mathbf{d} is the equilibrium position of the d^{th} atom in the unit cell.

Next we take into account the scattering cross-section due to the magnetic interaction between the neutron and unpaired electrons in the atom. The corresponding elastic differential scattering cross-section for a sample with many ferromagnetically ordered domains is given as (Squires, 2012)

$$\left(\frac{d\sigma}{d\Omega} \right)_{\text{el}} = (\gamma r_0)^2 N \frac{(2\pi)^3}{v_0} e^{-2W(\mathbf{Q})} F_{\text{mag}}^2(\mathbf{Q}) \langle S^\eta \rangle^2 \sum_{\boldsymbol{\tau}} \langle 1 - (\boldsymbol{\tau} \cdot \boldsymbol{\eta})_{\text{av}}^2 \rangle \delta(\mathbf{Q} - \boldsymbol{\tau}) \quad (4.16)$$

with the positive constant $\gamma = 1.913$, which is half the value of the neutrons' magnetic moment, r_0 is the classical radius of the electron equal to $2.818 \times 10^{-15} \text{m}$ and $\langle S^\eta \rangle$ is the average spin component in the direction $\boldsymbol{\eta}$, a quantity proportional to the magnetisation. $F_{\text{mag}}(\mathbf{Q})$ is the magnetic form factor which is defined according to Squires (2012) as

$$F_{\text{mag}}(\mathbf{Q}) = \int s(\mathbf{r}) e^{i\mathbf{Q} \cdot \mathbf{r}} d\mathbf{r} \quad (4.17)$$

with $s(\mathbf{r})$ being the normalised spin density of the unpaired electrons.

There are several differences between nuclear and magnetic elastic scattering. First, the magnetic form factor depends on Q , which results in a rapid decrease of the magnetic signal with increasing Q , whereas the nuclear form factor ($F_{\text{nuc}} = \bar{b}$) is independent of Q . Secondly, the magnetic Bragg scattering has a strong temperature dependence especially around the magnetic transition temperature T_c as it is proportional to $\langle S^\eta \rangle^2$ which falls to zero above T_c . For nuclear scattering the Bragg intensity varies only with the Debye-Waller factor. Lastly the magnetic scattering depends on the orientation of $\langle S^\eta \rangle$ relative to the reciprocal lattice $\boldsymbol{\tau}$ (Furrer, Mesot, and Strässle, 2009). Here only the components of the magnetisation perpendicular to $\boldsymbol{\tau}$ give a non-zero contribution to the scattering intensity. Note that in case of no preferred orientation of the ferromagnetic domains, the term $\langle 1 - (\boldsymbol{\tau} \cdot \boldsymbol{\eta})_{\text{av}}^2 \rangle$ converts to a factor of $2/3$.

For an anti-ferromagnet the average $\langle S^\eta \rangle$ taken over the whole lattice is zero, since a magnetically ordered domain decomposes into two interpenetrating sublattices, whose spins are oriented in opposite directions. Thus the cross-section is derived

for the so-called staggered average spin component $\langle S_i^\eta \rangle$, which corresponds to the magnetisation of each sublattice i . Its differential scattering cross-section is given for one sublattice with spins at the position \mathbf{d} in the magnetic unit cell (indicated by the index m) as

$$\left(\frac{d\sigma}{d\Omega} \right)_{\text{el}} = (\gamma r_0)^2 N_m \frac{(2\pi)^3}{v_{0,m}} \sum_{\boldsymbol{\tau}} |F_M(\boldsymbol{\tau}_m)|^2 \exp(-2W(\mathbf{Q})) (1 - (\boldsymbol{\tau} \cdot \boldsymbol{\eta})_{\text{av}}^2) \delta(\mathbf{Q} - \boldsymbol{\tau}_m). \quad (4.18)$$

The form factor F_M is defined by

$$F_M(\boldsymbol{\tau}_m) = \frac{1}{2} g \langle S_i^\eta \rangle F(\boldsymbol{\tau}_m) \sum_d \sigma_d e^{i\boldsymbol{\tau}_m \cdot \mathbf{d}} \quad (4.19)$$

where $\sigma_d = \pm 1$ is spin state at the position d in the magnetic unit cell.

4.3.3 Intensity in Time-of-Flight Neutron Powder Diffractometers

In an experiment the differential cross-section as described above can not be measured directly. Instead the cross-section of a Bragg peak, i.e., the integral of the differential cross-section over certain directions, is measured. In case of a powder sample the relationship between the integrated intensity I_{int} of the diffraction peak and its structure factors at the position Q_{hkl} may be written according to Squires (2012) as

$$I_{\text{int}} = \Phi \frac{V}{v_0^2} \frac{d\lambda^3}{8\pi r \sin \theta \sin 2\theta} \sum_Q |S(\mathbf{Q}_{hkl})|^2 e^{-2W(\mathbf{Q})} \quad (4.20)$$

where Φ is the neutron flux, $V = Nv_0$ represents the volume of the crystal, d is the effective diameter of the neutron detector which is placed at a distance r from the target and \sum_Q averages over all \mathbf{Q} with the same value of Q . Since we measure in a powder diffraction pattern the scattered intensity along one direction, not only one permutation of h , k and l results in the Bragg reflection at the respective Q , but all permutations which fulfill the Pythagorean requirement

$$h^2 + k^2 + l^2 = \left(\frac{2a \sin(2\theta/2)}{\lambda} \right)^2. \quad (4.21)$$

The number of permutations is called the multiplicity of the reflection.

Thus the intensity of a peak depends not only on the squared structure factors, the Debye-Waller factor and the multiplicities, but also on the setup of the experiment via the so called Lorentz factor.

Since one can not access the scattering cross-section directly in Q -space but in wavelengths or time-of-flights, the Lorentz factor accounts for the geometry and layout of the instrument, which - in case of POWGEN - uses a polychromatic beam and measures each data point for a fixed diffraction angle. Hence the corresponding Lorentz-factor is wavelength dependent and decomposes in two parts L_1 and L_2 .

The intensity detected for a given wavelength depends on the number of the reciprocal lattice points which can be observed at the same time. These points are distributed homogeneously on the surface of a sphere with radius Q in a powder sample, as each powder grain is randomly oriented. The observable area on this reciprocal sphere $4\pi Q^2$ corresponds to the first part of the Lorentz factor $L_1 \propto Q^{-2}$. For small Q the sphere is small and a large portion of this sphere is covered by the detector area. For large Q the area of the sphere increases quadratically, while the detector area stays the same, hence only a small portion of the respective sphere's surface can be detected. This leads to an asymmetric weight of the scattering events, since regions for large wavevector transfers are accounted for less than the regions for small wavevector transfers.

Further the intensity is not measured in Q but in the time-of-flight of the neutron, which is according to Eq. (4.1) linearly proportional to its wavelength λ . Hence a conversion of Q to λ has to be considered, where the wavevector transfer Q is inversely proportional to the wavelength via

$$Q = \frac{4\pi}{\lambda} \sin(2\theta/2). \quad (4.22)$$

For a fixed scattering angle we obtain

$$dQ \propto \frac{1}{\lambda^2} d\lambda. \quad (4.23)$$

The total Lorentz factor depends therefore on the units the measurement is analysed: It is the combination of both geometrical effects and is therefore proportional to λ^4 , if the measurement is analysed in t (Buras and Gerward, 1975), or Q^{-2} , if the data is transformed into Q -space and the conversion of Q is no longer necessary.

To extract the structural details from the diffraction data the Pawley refinement method (Pawley, 1981) was employed. The Bragg intensity $y_B(t)$ is given as (Von Dreele, Jorgensen, and Windsor, 1982)

$$y_B(t) = |S_{hkl}|^2 e^{-2W(Q)} m_{hkl} L(t) F(t) \quad (4.24)$$

where m_{hkl} is the multiplicity of the Bragg peak and $F(t)$ is the peak shape function.

The instrumental resolution function (IRF) $F(t)$ of a TOF diffractometer is according to Von Dreele, Jorgensen, and Windsor (1982) and Thompson, Cox, and Hastings (1987) best described by the convolution of back-to-back exponentials with a pseudo-Voigt-function. The peak shape parameters describe the rising and decaying exponentials with the rise coefficient α and the decay coefficient β , respectively, as well as the Gaussian (σ) and Lorentzian (γ) contributions to the pseudo-Voigt-function. Before each beam time cycle several standard samples are measured for calibration. The numerical considerations for this resolution functions are discussed in detail in the appendix A.

4.3.4 Determination of the Structural Domain Size

The general structure of an ordered Heusler alloy (X_2YZ) is $L2_1$ order and can be described by four interpenetrating fcc lattices. For crystals of an fcc symmetry non-zero Bragg reflections are observed solely for all even or all odd Miller indices (hkl) of the scattering planes. The corresponding reflections can be divided into three peak families originating from A2, B2 and $L2_1$ order (Webster et al., 1984). Their respective structure factors are defined as

$$\begin{aligned} S_{A2}(h, k, l) &= 4|(2f_X + f_Y + f_Z)| && \text{if } (h + k + l)/2 = 2n \\ S_{B2}(h, k, l) &= 4|(2f_X - f_Y - f_Z)| && \text{if } (h + k + l)/2 = 2n + 1 \\ S_{L2_1}(h, k, l) &= 4|(f_Y - f_Z)| && \text{if } h, k, l \text{ all odd} \end{aligned}$$

where f_i is the average scattering factor of one of the four fcc sublattices, with the average taken over the scattering factors of the respective atoms occupying this sublattice. The structure factor of the A2 reflections solely depends on the alloys' composition, resulting from all lattice sites contributing in phase. For B2 order, as mentioned in Chap. 2, the structure factor results from the diffraction contrast between the Wyckoff positions (1a) and (1b), which are occupied by X atoms and a random distribution of Y and Z atoms, respectively. Finally the $L2_1$ peaks are due to the diffraction contrast of the inner fcc sublattices of the bcc structure, resulting from the different scattering lengths on the Y and the Z sublattices.

Fig. 4.6 shows the neutron powder diffraction patterns of the four $Ni_2MnAl_{0.5}Ga_{0.5}$ samples at $T_m = 450$ K using both center wavelengths. All diffraction peaks can be assigned to the three distinct peak families, A2, B2 and $L2_1$. The A2 and B2 reflections

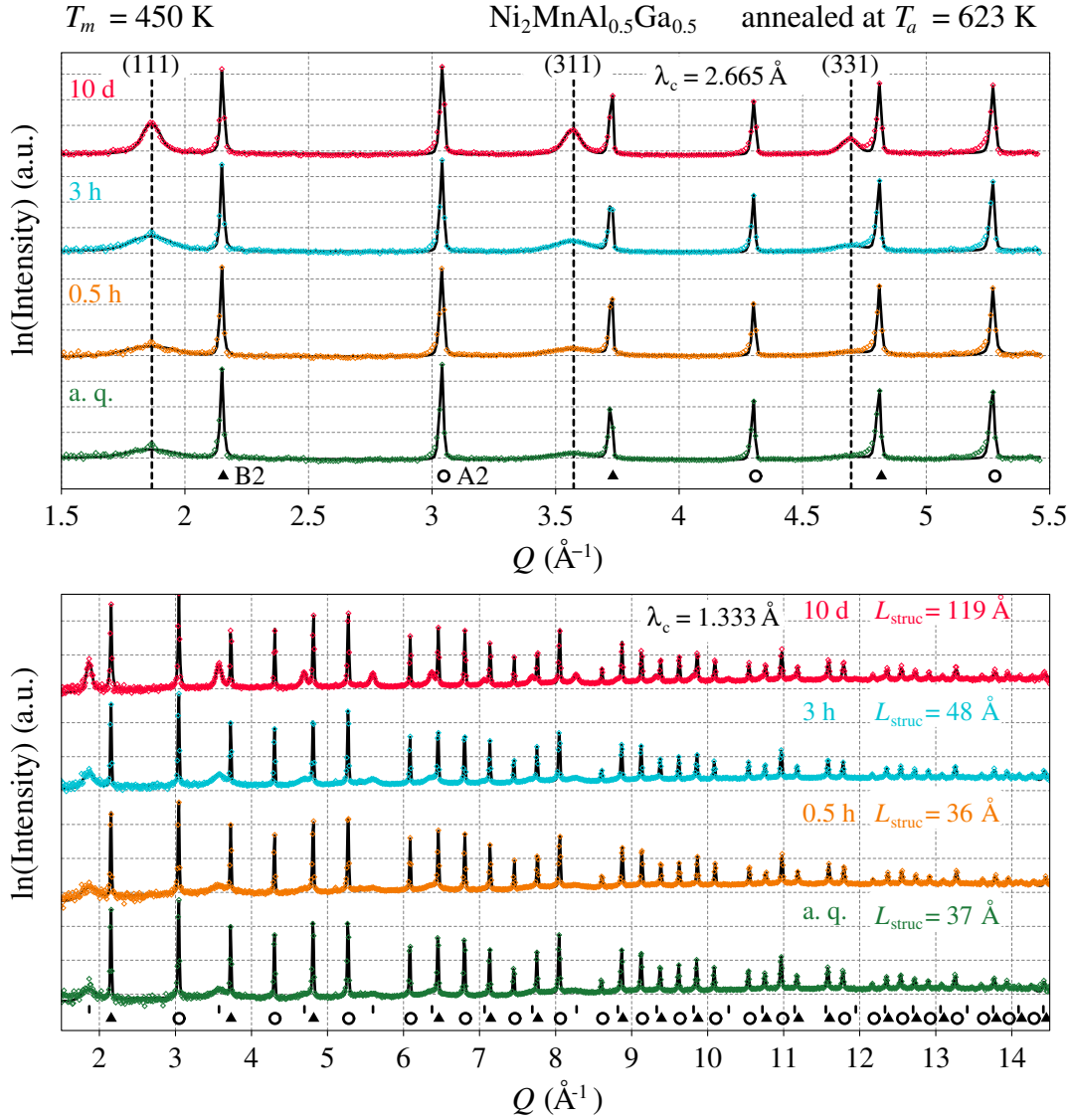


Figure 4.6: Neutron diffraction patterns obtained for $\text{Ni}_2\text{MnAl}_{0.5}\text{Ga}_{0.5}$ in four distinct annealing states, $T_a = 623$ K. The measurements were performed at $T_m = 450$ K, well above the highest $T_c = 392$ K of the powder samples, and with a center wavelength $\lambda_c = 2.665$ Å (top) and $\lambda_c = 1.333$ Å (bottom). The solid black lines represent the Pawley refinements to the experimental data, the location of the nuclear reflections (A2, B2 and L_{21}) is indicated by small symbols (circle, triangle and grey dotted line for $\lambda_c = 2.665$ Å or bar for $\lambda_c = 1.333$ Å) at the bottom of the diagrams.

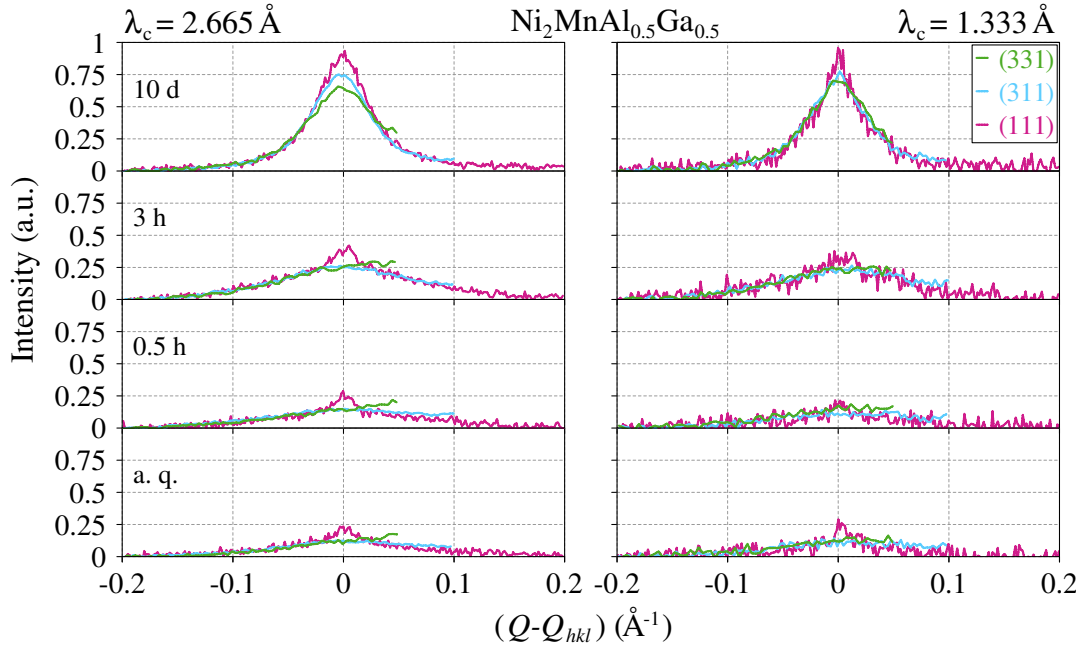


Figure 4.7: L_{21} peaks present in the diffractogram at $\lambda_c = 2.665 \text{ \AA}$ and $\lambda_c = 1.333 \text{ \AA}$ shifted onto each other, corrected for the Debye-Waller factor, multiplicities as well as the background.

are as sharp as expected from the calibration measurements for every annealing state and therefore independent of the respective finite correlation length of L_{21} order. Therefore, in order to describe the structural details of our patterns as best as possible the IRF parameters were adapted to fit the A2 and B2 peaks, as we observe no indication of strain or size broadening in these reflections.

In contrast to that the reflections of the L_{21} peak family are generally broader than expected from the calibration measurements. As a function of increasing annealing time all of these peaks sharpen and gain intensity, independent of their location in Q -space. Fig. 4.7 displays the L_{21} peaks shifted onto each other, which were measured using $\lambda_c = 2.665 \text{ \AA}$ at $T_m = 450 \text{ K}$ and are corrected for the Debye-Waller factor, multiplicities of the specific reflection and the background. The broadening of the different reflections is independent of the peak location, hence the finite correlation length of L_{21} order must be the reason for this broadening. By comparing the diffraction patterns of different annealing duration the continuous transition from B2 to L_{21} order can be observed. Even though the measurements were performed well above the magnetic transition temperatures we still observe additional intensity on the smallest L_{21} reflection (111) for all annealing states. Here the additional signal decays with increasing Q . The L_{21} reflections at larger Q show no additional signal, as shown in Fig. 4.7, thus — due to the strong Q -dependence of the magnetic

structure factor ($\propto Q^{-4}$) — the nature of this signal must be magnetic. At such high temperatures possible magnetic short-range order from, e.g., neighbouring Mn-Mn atoms present at the APBs or as local disorder in the APDs can cause this additional intensity contribution. Thus the smallest reflection is neglected in the refinement analysis and does not contribute to the determination of the structural details of the diffraction data.

To investigate the ordering transition from B2 to L2₁ order quantitatively we employed the Pawley refinement method (Pawley, 1981) and examined the evolution of the correlation length of L2₁ order with annealing time. We used a linear combination of only resolution broadened peak profiles for the A2 and B2 reflections, a six coefficient polynomial for the background, and an additional model function given in Eq. 3.17 to describe the broadened L2₁ peaks. The model function $S'(QL_{\text{struc}}(t)/2)$ was derived in the previous chapter (Chap. 3) and is centered around the Bragg peak position Q_{hkl} . The retrieved scale of the APDs $L_{\text{struc}}(t)$ is inverse proportional to the interfacial density of the domains and is equivalent to the scale obtained by the linear intercept method (Smith and Guttman, 1953) used in microscopy experiments. The corresponding refinements are plotted together with the patterns in the semi-logarithmic plot for the Ni₂MnAl_{0.5}Ga_{0.5} in Fig. 4.6 and for the Ni₂MnAl samples in Fig. 4.8. The diffractograms of the Ni₂MnAl samples show the same qualitative behaviour, with the L2₁ peaks increasing in sharpness and intensity with annealing time.

Using this combination we refine the diffractograms at both λ_c simultaneously via least-squares fitting. According to counting statistics the inverse of the squared uncertainties of the diffraction data was used as weights. We obtain an excellent agreement between the refinements and the diffraction data for all annealing states and both alloy families. The corresponding L2₁ order length scales L_{struc} , as listed in Fig. 4.8 and 4.6, increase with annealing time. By comparing the retrieved length scales of both alloy families the lower L2₁ ordering tendency of Ni₂MnAl becomes clear, with its largest length scale being about half of the longest (10 d) annealed Ni₂MnAl_{0.5}Ga_{0.5} sample.

The correlation length of L2₁ order grows with annealing time. This positive correlation was also observed in TEM measurements for Ni₂MnAl_{0.5}Ga_{0.5} samples, which were of the order of 100 nm (Yano et al., 2007; Umetsu et al., 2011; Murakami et al., 2011). Since these samples were annealed at a higher temperature (673 K (Yano et al.,

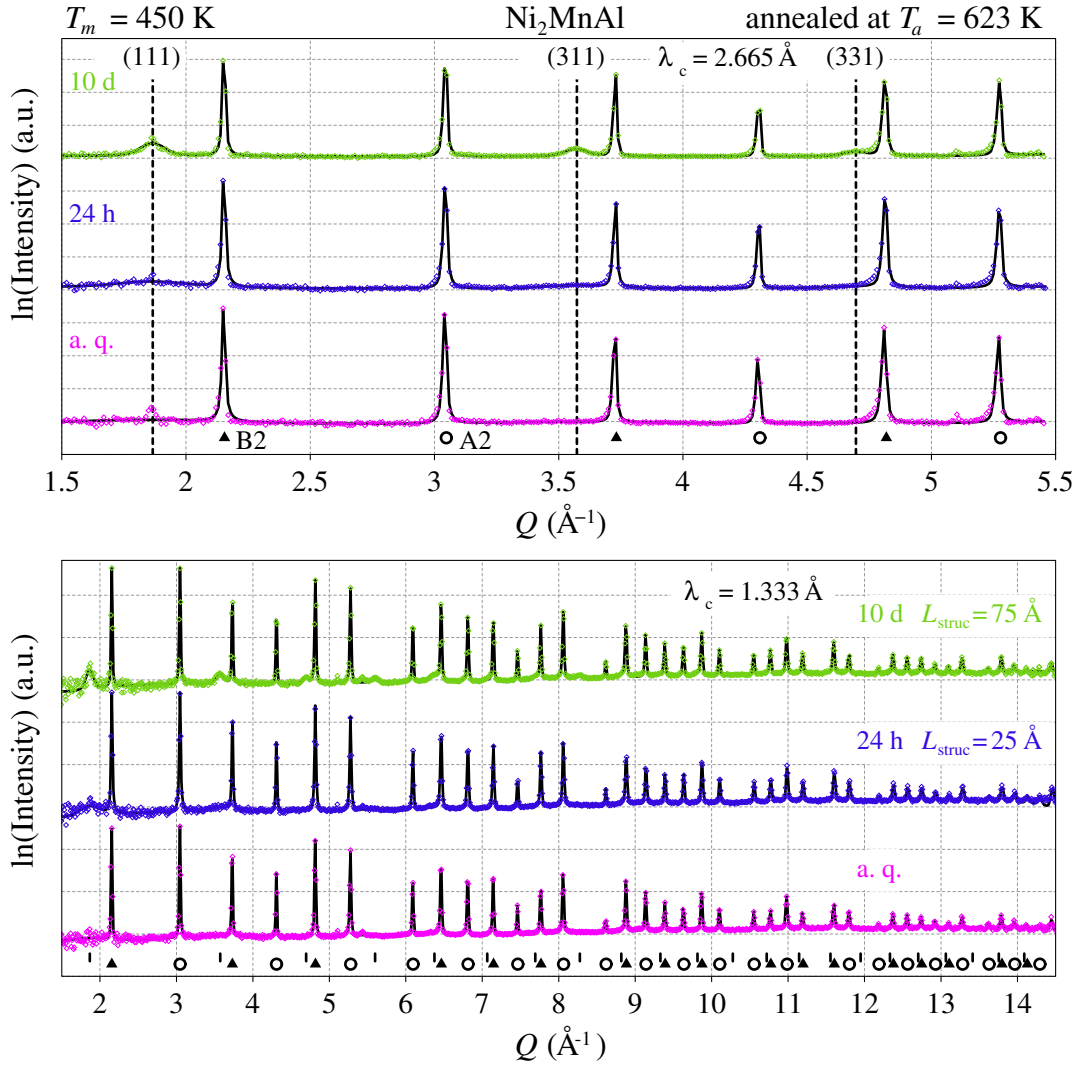


Figure 4.8: Neutron diffraction patterns obtained for Ni_2MnAl in three distinct annealing states. The measurements were conducted at $T_m = 450$ K with the center wavelengths $\lambda_c = 2.665$ Å (top) and $\lambda_c = 1.333$ Å (bottom); the solid black lines represent the Pawley refinements to the experimental data, the location of the nuclear reflections (A2, B2 and L_1) is indicated by small symbols (circle, triangle and grey dotted line for $\lambda_c = 2.665$ Å or bar for $\lambda_c = 1.333$ Å) at the bottom of the diagrams.

2007; Murakami et al., 2011) and 773 K (Umetsu et al., 2011), respectively) in contrast to our samples (annealed at 623 K), their domain sizes are as expected larger.

4.4 Small-Angle Neutron Scattering

In order to investigate the microstructure as well as magnetic inhomogeneities on the mesoscopic length scale (1 nm up to a few hundred nm) (Mühlbauer et al., 2019), small-angle neutron scattering (SANS) proves to be a powerful technique. SANS enables the study of the formation and growth of precipitation in a phase separation process (Kostorz, 1991) as well as the magnetic microstructure due to the magnetic interaction of the neutron and the unpaired electrons of the atoms. Thus, using this technique we can investigate the formation and growth of magnetically ordered domains in our structurally ordered compounds.

We performed SANS measurements at the instrument SANS-1 at the Forschungsreaktor München II (FRMII), Garching, and at the instrument D33 at the Institut Laue-Langevin (ILL), Grenoble. Since both instruments are located at a nuclear reactor, the setup of SANS-1 will be described in the following as an example for a SANS experiment with a monochromatic neutron beam. The specifications for the instrument setup of D33 are given below. The typical setup is sketched in figure 4.9.

A cold neutron beam is guided through a vertically curved S-shaped neutron guide line to a selector tower. The S-shape of the guide line prevents undesired neutrons to arrive at the instrument by resulting in a cut-off to small wavelengths, as these fast neutrons would only increase the background (Gilles, Ostermann, and Petry, 2007). Passing an adjacent velocity selector tower produces a qisuaasi monochromatic beam of cold neutrons of a bandwidth $\Delta\lambda = 10\%$ in a wavelength range of 4.5 Å to 30 Å. The beam passes a collimation system consisting of a combination of apertures which allow only neutrons whose path is sufficiently straight to pass. The collimation system has a variable length of 1 m up to 20 m. The collimated beam then hits the

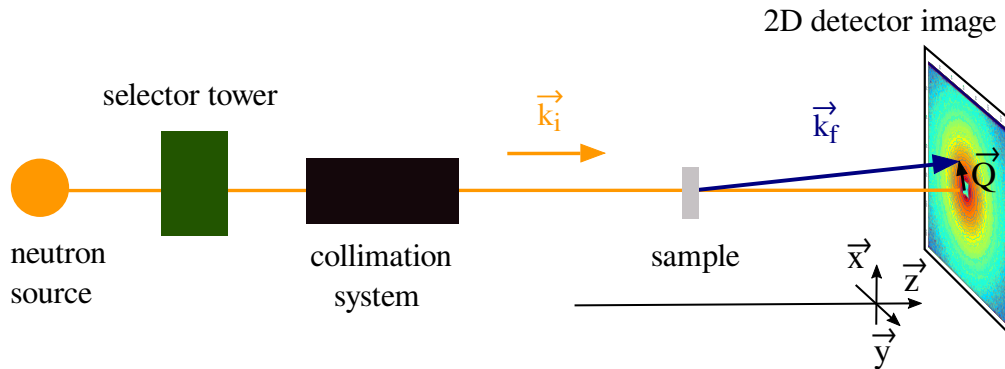


Figure 4.9: Sketch of the setup of a SANS instrument with a monochromatic neutron beam at a nuclear reactor. The scattering signal is recorded in the $Q_x \times Q_y$ plane.

powder sample and the intensity of the scattered neutrons is recorded by an 1 m×1 m detection area. The detector can be moved to a sample-detector distance of 2 m up to 22 m. It is made out of 128 position sensitive ^3He tube-detectors with the tubes having an active length of 1 m and a diameter of 7.94 mm. This yields a final pixel resolution of 8 mm×8 mm (Mühlbauer et al., 2016) and a detection area of 128×128 pixels.

The instrument setup of D33 consists a velocity selector producing a quasi-monochromatic beam of neutrons with wavelengths between 4.5 Å and 40 Å (Dewhurst et al., 2016). The scattered neutrons are detected in the evacuated detector tank by five position-sensitive ^3He detector panels, consisting of a rear area detector and four separate monoblock panels. The sample-detector distance can be varied between 1.2 m to 12.8 m with a minimum distance of 0.8 m between the front panels and the rear detector. The dimensions of an individual ^3He gas tube are 4.5 mm×10 mm with the rear detector consisting of a 0.64 m×0.64 m array of 128 horizontal position-sensitive detector tubes. The position along the wire is digitized into 256 channels, corresponding to a pixel size of 2.5 mm, thus yielding a detector area of 256×128 pixels. The intrinsic resolution along the wire length is estimated to be approximately 5 mm, matching that of the tube spacing in the vertical direction (Dewhurst et al., 2016).

The accessible Q -range depends on the sample-detector distance L , the wavelength of the incoming neutrons λ as well as the accessible radial distance on the detector r (Mühlbauer et al., 2019) and is given via the following equation

$$Q = \frac{4\pi}{\lambda} \sin(0.5 \arctan(r/L)). \quad (4.25)$$

4.4.1 Neutron Scattering of Large Structures

Since length scales larger than atomic dimensions are investigated, a description of the corresponding differential scattering cross-section via the point-like Fermi-pseudo potentials as in Eq. (4.12) is no longer reasonable. Instead, we introduce the scattering length density $\rho(\mathbf{r})$, which is the total scattering length per unit volume. Using this quantity the elastic differential scattering cross-section $d\sigma/d\Omega(\mathbf{Q})$ defined in Eq. (4.12) transforms to macroscopic elastic differential scattering cross-section $d\Sigma/d\Omega(\mathbf{Q})$ which is averaged over the whole sample and can be expressed according

to Feigin and Svergun (1987) by

$$\begin{aligned}\frac{d\Sigma}{d\Omega}(Q) &= \left| \int_V \rho(\mathbf{R}) \exp(-i\mathbf{Q} \cdot \mathbf{R}) d\mathbf{R} \right|^2 \\ &= \int_V \int_V \rho(\mathbf{R})^* \rho(\mathbf{R}_2) \exp(-i\mathbf{Q} \cdot (\mathbf{R}_2 - \mathbf{R})) d\mathbf{R} d\mathbf{R}_2 \\ &= \int_V \left[\int_V \rho(\mathbf{R})^* \rho(\mathbf{R} + \mathbf{r}) d\mathbf{R} \right] \exp(-i\mathbf{Q} \cdot \mathbf{r}) d\mathbf{r}\end{aligned}$$

with V being the sample volume and $*$ denoting the complex conjugation. Since the autocorrelation function of the scattering length density is defined as the term in the square brackets, $d\Sigma/d\Omega(Q)$ is its Fourier transform.

If the scattering model can be considered to consist of two phases of different scattering length densities (ρ_1 and ρ_2), for example grains and vacuum or magnetic domains with different magnetisation, one can investigate the shape and size of large structures in the sample. In structural ordering processes — as the ones we observe for Ni_2MnZ compounds — the structurally ordered domains have the same scattering length density, thus making it impossible to detect structural domains in our samples using SANS. However, due to the neutron's exchange interaction with the local internal magnetic field we can still use SANS to access the magnetic microstructure.

4.4.2 Magnetic Domains in Ni_2MnZ Compounds

In order to investigate the magnetic microstructure of the $\text{Ni}_2\text{MnAl}_{0.5}\text{Ga}_{0.5}$ and Ni_2MnAl powder samples with distinct L2_1 order states, small-angle neutron scattering measurements were conducted at SANS-1 at the FRM II, Garching. To reduce the probability of multiple scattering events the powder samples, which were wrapped in aluminium foil, had an effective thickness of 0.4 mm. Measurements between 4.2 K and 450 K were performed at three detector distances, 2 m, 8 m and 20 m, using unpolarised neutrons. For the short detector distances we chose a neutron wavelength of 5 Å, while for the largest distance we performed measurements using a wavelength of 6 Å in order to access a Q -regime of down to 0.002 Å^{-1} . To limit the influence of the beam stop, correct for inactive detectors as well as the noise from the shadow of the beam tube we applied a mask to our data. In the absence of an external magnetic field the scattering was isotropic in the detector plane ($Q_x \times Q_y$), thus it was radially averaged to obtain the scattering signal $d\Sigma/d\Omega(Q)$ in the Q range of $0.002 \text{ Å}^{-1} \leq Q \leq 0.3 \text{ Å}^{-1}$. Instead of stabilizing the temperature the data were collected continuously during temperature sweeps to acquire them in the whole temperature

range. We observe no dependence of the signal on the temperature gradient, as the profiles measured during a cooling cycle are identical the profiles measured while heating the sample. The signal of an empty Aluminum foil was measured for all three distances and subtracted from the respective samples' intensities.

Fig. 4.10 displays the SANS profiles in a temperature range from 5 K to 450 K of the $\text{Ni}_2\text{MnAl}_{0.5}\text{Ga}_{0.5}$ powder samples. For the sample with the longest annealing duration of 10 d, shown in Fig. 4.10 panel a), the SANS profiles recorded above the magnetic transition temperature of $T_c = 392$ K can be best described for small $Q < 0.03 \text{ \AA}^{-1}$ by a straight line on these double logarithmic plots, indicating a power-law behaviour. The scattering intensity in this low Q -regime has its main contributions from the divergence of the beam as well as the Porod scattering of large (> 100 nm) 3D structures, such as powder grains or powder grain boundaries. In the high Q -regime ($Q > 0.1 \text{ \AA}^{-1}$) the power-law scattering gives way to a different behaviour. Here the intensity consists mainly of scattering of chemical inhomogeneities on the atomic length scale as well as incoherent scattering. Hence no large structures of the mesoscopic length scale can be observed at such high temperatures in the SANS profiles where our sample is paramagnetic.

With decreasing temperature an additional intensity contribution appears in the SANS profiles at $Q \approx 0.1 \text{ \AA}^{-1}$, which shifts in the temperature range from 450 K to 390 K towards lower Q . This behaviour can be observed best by comparing the last three SANS profiles which correspond to the measurements at 450 K, 400 K and 390 K. For the profile at 450 K shows no additional signal, while for the measurement at 400 K we observe a new contribution in the profile, with its maximum being at around $Q = 0.07 \text{ \AA}^{-1}$. This contribution appears to have shifted to $Q = 0.05 \text{ \AA}^{-1}$ for the measurement at $T_m = 390$ K.

Below the magnetic transition temperature the additional signal remains at around $Q \approx 0.03 \text{ \AA}^{-1}$ and increases in intensity with decreasing temperature. Atomic diffusion is at such low temperatures inactive in this composition, thus structural changes cannot be the reason for any temperature-dependent signal and the nature of this signal must be magnetic, corresponding to the scattering of magnetic domains in the sample.

This temperature-dependent behaviour is present in all annealing states, Fig. 4.10 a) to d), as well as in the ternary alloy family, with the corresponding measurements displayed in Fig. 4.11 b) and c). The signal is most distinctive for the profile of the sample with the longest annealing duration and weakest for the as-quenched

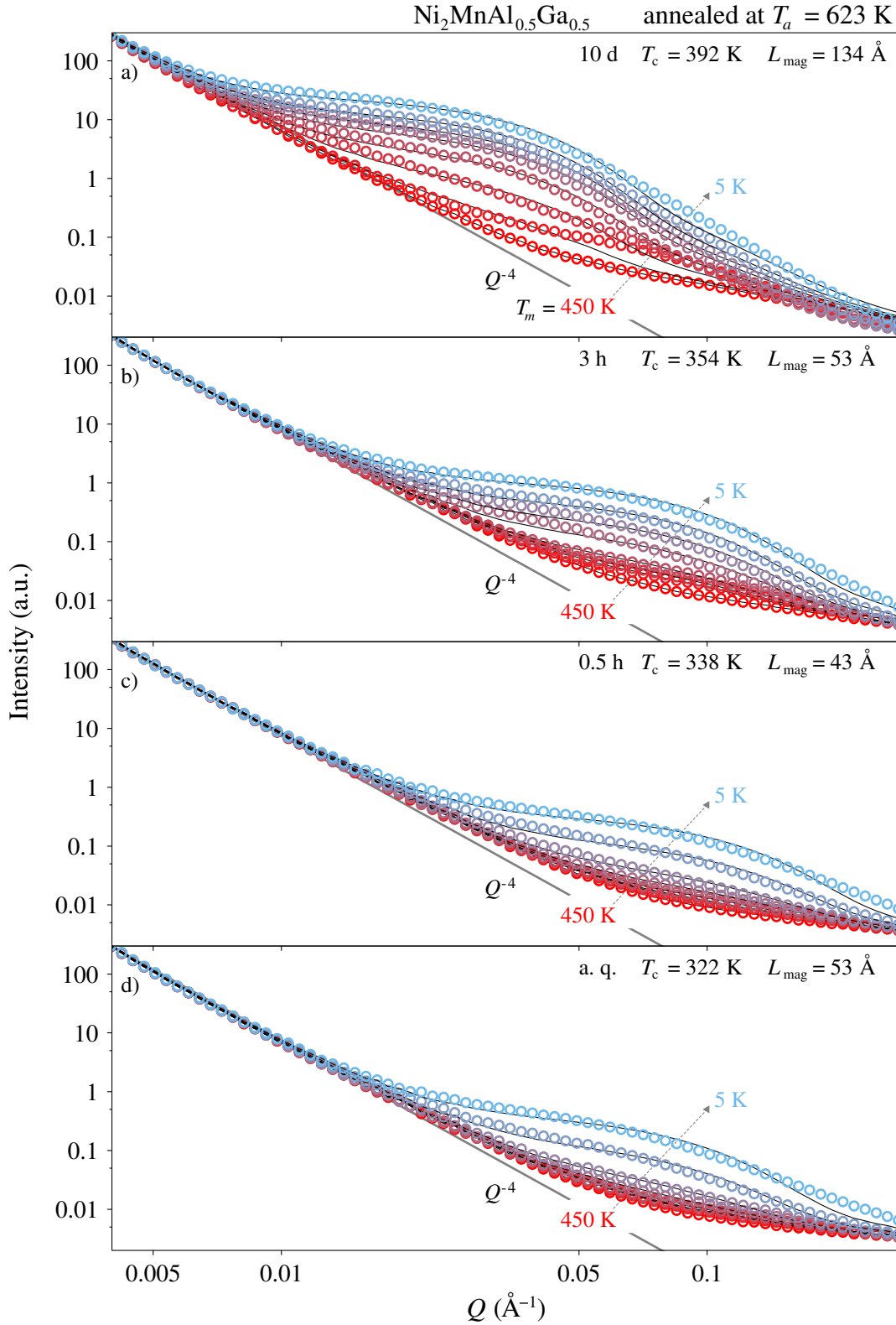


Figure 4.10: Temperature-dependent SANS profiles of the $\text{Ni}_2\text{MnAl}_{0.5}\text{Ga}_{0.5}$ samples annealed for a) 10 d, b) 3 h, c) 0.5 h at $T_a = 623 \text{ K}$ and d) the as-quenched sample at $T_m = 5 \text{ K}$, 300 K, 340 K, 360 K, 380 K, 390 K, 400 K and 450 K. The profiles are plotted together with a linear combination of the profile at 450 K and a model function given in Eq. 3.16 (black line).

one. Its onset varies for each sample, corresponding to the respective transition temperature T_c . A similar temperature-dependence of the SANS profiles was observed in $\text{Ni}_{44}\text{Co}_6\text{Mn}_{40}\text{Sn}_{10}$ alloys, see Ref. (Bhatti et al., 2012; El-Khatib et al., 2019).

To study the extent of the magnetic order quantitatively we fit the SANS profiles using a combination of the signal at $T_m = 450$ K, $I_{450\text{ K}}$, corresponding to the structural scattering signal of the sample, and the model function given in Eq. (3.16), which accounts for the scattering signal from the magnetic domains and was derived in the previous chapter. The model function is composed of a Lorentzian and two Gaussian distributions, as depicted in Fig. 4.11 a), and the complete fit to the SANS profiles is given as

$$I(Q) = A(T)(L_{\text{mag}}(t)/2)^3 S(QL_{\text{mag}}(t)/2) + B(T)I_{450\text{ K}}. \quad (4.26)$$

We determine the size L_{mag} from the low temperature measurements ($T_m < 200$ K). Under the assumptions that the magnetic domains are continuous as well as their size is temperature-independent, we keep L_{mag} fix for the determination of the factors $A(T)$ and $B(T)$ for all measurements. In order to minimize the relative – instead of the absolute – deviations between the data and our model on this double logarithmic scale, we used the inverse square of the intensity as weights instead of the inverse intensity, which would correspond to the weights according to the counting statistics. We observe a satisfactory agreement between the SANS profile and the fit. The prefactor A is a measure of the strength of the magnetic signal, while B is the prefactor of the structural signal and is of the order of unity.

The obtained length scale L_{mag} corresponds to the magnetic domain interface density, as listed in Tab. 4.3. Since the length scale obtained via SANS is equivalent to the length scale extracted from the neutron powder diffraction data (Zweck and Leitner, 2021), we can compare the extent of the magnetic as well as the structural order directly without any further transformation needed. Both scales are of the same size and increase with annealing time, as it has been reported in Lorentz-TEM measurements (Umetsu et al., 2011). Their values agree satisfactory and imply both domains to be identical. This observation agrees with the measurements performed on $\text{Ni}_2\text{MnAl}_{0.5}\text{Ga}_{0.5}$ as well as Ni_2MnGa samples using Lorentz-TEM (Murakami et al., 2006; Venkateswaran, Nuhfer, and De Graef, 2007; Ishikawa et al., 2008; Umetsu et al., 2011).

In contrast to the quaternary compound the SANS profile of the as-quenched Ni_2MnAl sample shows no additional intensity at low temperatures, implying that Ni_2MnAl in its B2 ordered state has no magnetic inhomogeneities such as ferromagnetic domains.

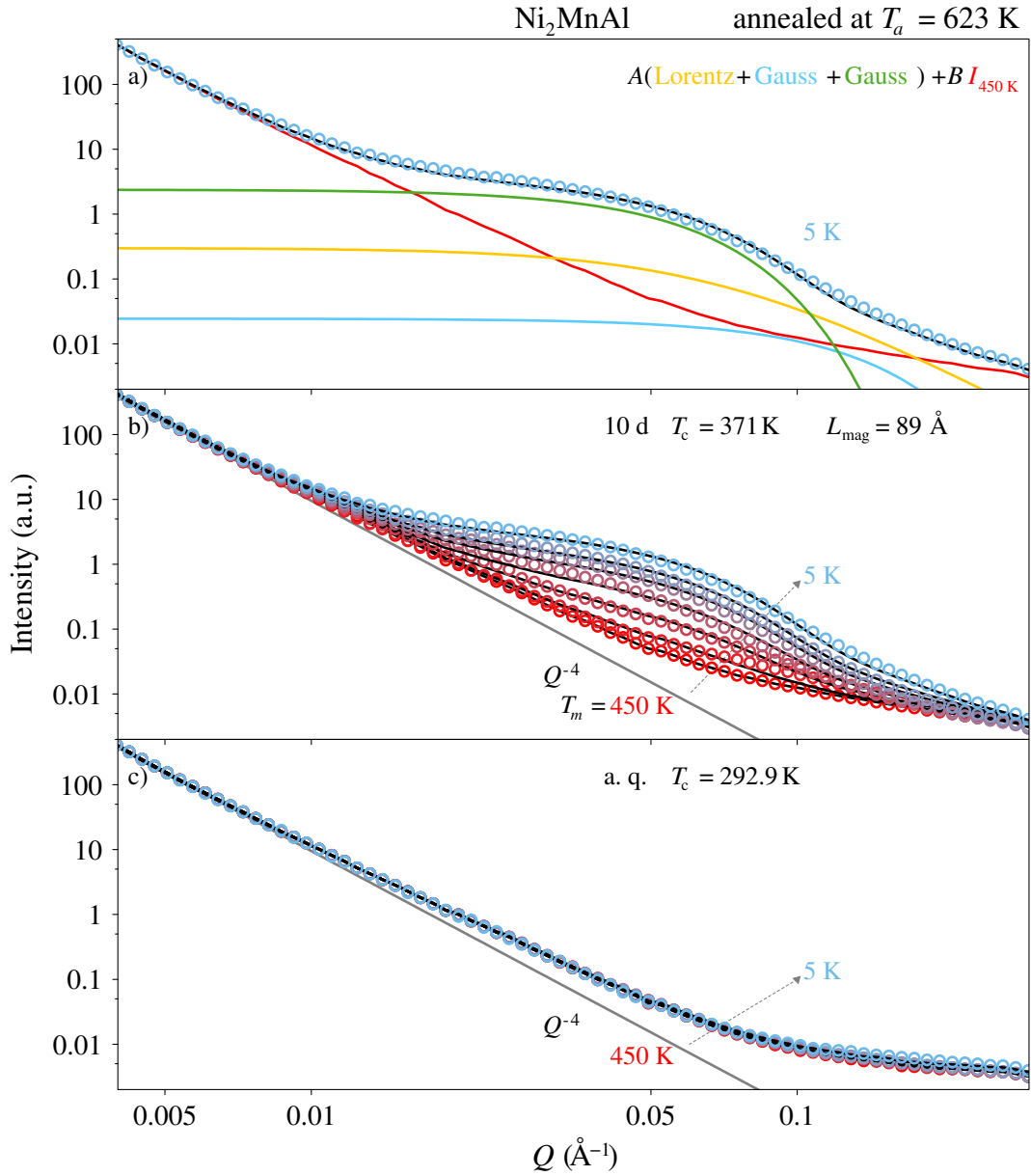


Figure 4.11: a) The model's contributions for the SANS profile at $T_m = 5 \text{ K}$ for the Ni_2MnAl sample 10 d annealed at $T_a = 623 \text{ K}$ are a Lorentzian and two Gaussians together with the signal at 450 K. Temperature-dependent SANS profiles of the Ni_2MnAl sample annealed for b) 10 d and c) the as-quenched sample at $T_m = 5 \text{ K}$, 300 K, 340 K, 360 K, 380 K, 390 K, 400 K and 450 K. The profiles are plotted together with a linear combination of the profile at 450 K and a model function 3.16 (black line).

$\text{Ni}_2\text{MnAl}_{0.5}\text{Ga}_{0.5}$	as-quenched	0.5 h	3 h	10 d
$L_{\text{struc}}(\text{\AA})$	44	42	52	119
$L_{\text{mag}}(\text{\AA})$	52	43	53	134
Ni_2MnAl	as-quenched		24 h	10 d
$L_{\text{struc}}(\text{\AA})$	-		39	71
$L_{\text{mag}}(\text{\AA})$	-		-	89

Table 4.3: APB density L_{struc} as well as magnetic interface density L_{mag} of the $\text{Ni}_2\text{MnAl}_{0.5}\text{Ga}_{0.5}$ and Ni_2MnAl samples of distinct annealing durations at $T_a = 623$ K.

This observation agrees with the magnetisation measurements of Acet et al. (2002), who found Ni_2MnAl in the B2 ordered state to exhibit anti-ferromagnetic properties.

4.4.2.1 Magnetic Transition

The difference between the integral weighted with the square of Q , $\int I(Q)Q^2 dQ$, of the SANS profiles and the respective weighted integral of the signal at 450 K is proportional to the strength of the magnetic contribution $A(T)$. In order to obtain a quantity proportional to the magnetic moment of the sample the integral is taken in a Q -range relative to the magnetic domain size, $[\pi/L_{\text{mag}}, 3\pi/L_{\text{mag}}]$, as well as corrected to the weight and composition of the respective sample. In Fig. 4.12 the temperature-dependent difference integrals are shown relative to the difference integral of the SANS profile at 5 K of the $\text{Ni}_2\text{MnAl}_{0.5}\text{Ga}_{0.5}$ sample 10 d annealed. The magnetic signal decreases continuously to zero with increasing temperature, indicating a second order phase transition. Fitting the transition with the critical mean-field behaviour $(1 - (T/T_c))^{1/2}$ allows us to obtain the respective magnetic transition temperatures. The extrapolated values are in good qualitative agreement with the results obtained via the DSC measurements, but the DSC values are noticeably lower which is due to the diffuse DSC curves and the resulting phenomenological determination of its transition temperature.

With annealing time, the magnetic contribution of the small-angle scattering signal increases steadily for all powder samples of both the $\text{Ni}_2\text{MnAl}_{0.5}\text{Ga}_{0.5}$ and Ni_2MnAl alloys. For the latter one, we observe an increase from essentially zero according to Fig. 4.11 c). This increase is contradictory to the time-dependent behaviour of the characteristic lengths L_{mag} , where we observe at small annealing times almost no change and only after 10 d annealing a significant increase. We interpret these results in the following way: The coarsening kinetics show a thermally activated behaviour. Hence, when a sample is quenched from a disordered state to room temperature,

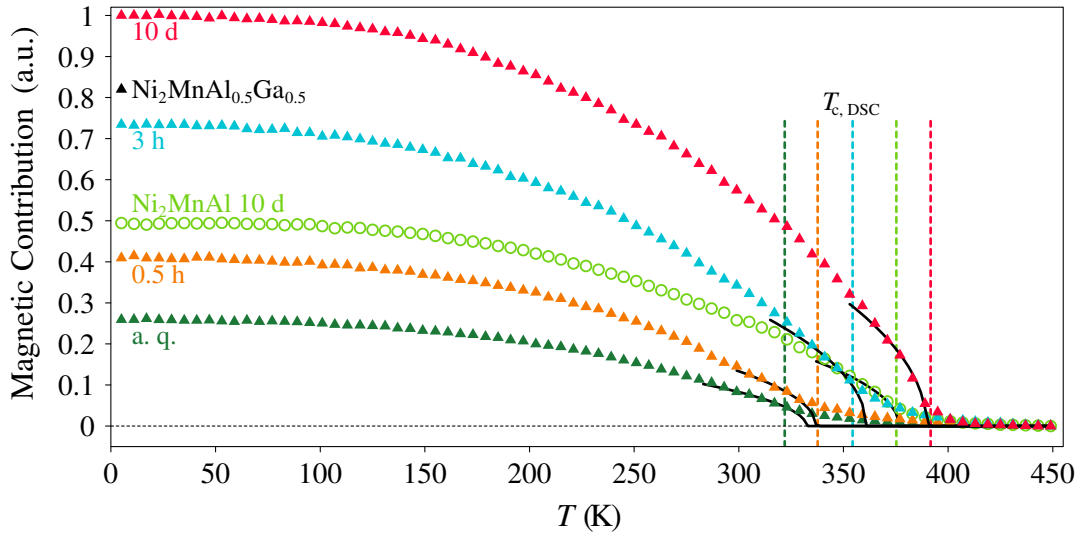


Figure 4.12: Strength of the magnetic contribution in the SANS profiles in the temperature range between 5 K and 450 K in $\text{Ni}_2\text{MnAl}_{0.5}\text{Ga}_{0.5}$ and Ni_2MnAl powder samples relative to the maximum strength in $\text{Ni}_2\text{MnAl}_{0.5}\text{Ga}_{0.5}$ 10 d annealed. The magnetic transition temperature is extrapolated by fitting the data close to the transition by the mean-field behaviour $(1 - T/T_c)^{1/2}$, plotted here as solid black lines, while the corresponding transition temperatures obtained via DSC measurements are plotted as dashed lines.

the few moments the sample spends just below the ordering temperature, 931 K for $\text{Ni}_2\text{MnAl}_{0.5}\text{Ga}_{0.5}$ (Ishikawa et al., 2008) and 1220 K (Soltys, 1981) for Ni_2MnAl , will coarsen the configuration to a scale that would have taken much longer to reach at the low-temperature annealing temperature of 623 K. However, the resulting APDs will show a lower degree of long-range order than expected for the low-temperature annealing temperature, since their degree of long-range order will correspond to the one just below the order-disorder transition. As a consequence, the ordered moment per formula unit is small, as a Mn anti-structure atom aligns antiparallel to the regular Mn spins (Simon et al., 2015). Hence, when low-temperature annealing such a quenched sample, the first few atomic exchanges per site will increase the degree of long-range order of the APD configuration towards the new equilibrium value, which apparently corresponds to timescales of some hours. Thus, this explains the increase in magnetic scattering, while observing no change in the growth of the characteristic length scale. The latter process, corresponding to the coarsening of the domains, takes place on much longer timescales on the order of days. Another contribution to the increase of the magnetic small-angle contribution would be a finite width of disordered APD walls, whose volume fraction decreases with coarsening, but we think this effect to be much smaller in comparison.

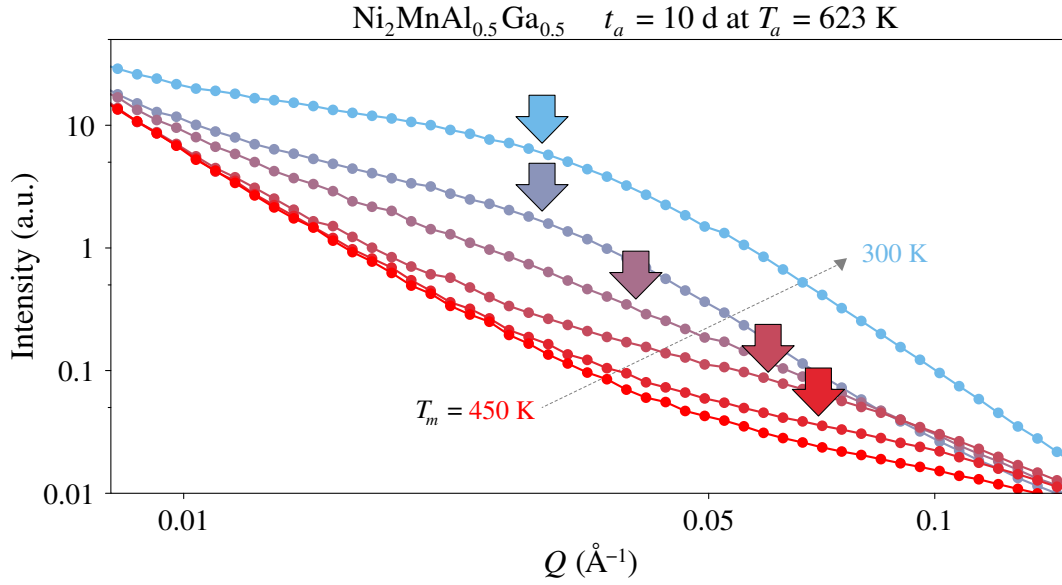


Figure 4.13: Radially averaged SANS signal at 300 K, 380 K, 390 K, 400 K, 420 K and 450 K for the $\text{Ni}_2\text{MnAl}_{0.5}\text{Ga}_{0.5}$ sample 10 d annealed.

4.4.2.2 Shift of Intensity

As mentioned above the intensity of the additional signal shifts towards smaller Q close to the transition temperature while cooling the sample. This shift can be observed well by comparing the SANS profiles measured close to T_c , with a section of distinct profiles measured on the $\text{Ni}_2\text{MnAl}_{0.5}\text{Ga}_{0.5}$ sample with the longest annealing duration being shown in Fig. 4.13. In order to investigate the intensity distribution of the additional signal quantitatively the difference spectra between the profiles and the signal at 450 K is studied. The corresponding difference spectra for the $\text{Ni}_2\text{MnAl}_{0.5}\text{Ga}_{0.5}$ sample annealed for 10 d are shown in Fig. 4.14 together with the respective structure factors $S(Q)$.

Approximating this magnetic signal for $Q \rightarrow 0$ with the structure factor allows us to investigate the mean $\langle Q \rangle$ which is given as

$$\langle Q \rangle = \frac{\int S(Q) Q dQ}{\int S(Q) dQ}. \quad (4.27)$$

Its evolution with temperature is shown in Fig. 4.15. For all annealing states as well as for both alloy families the mean Q value is constant below the respective transition temperature at roughly π/L_{mag} . Above T_c $\langle Q \rangle$ increases, corresponding to a shift of intensity towards higher Q , with the most distinct shift being observed for the longest annealed samples.

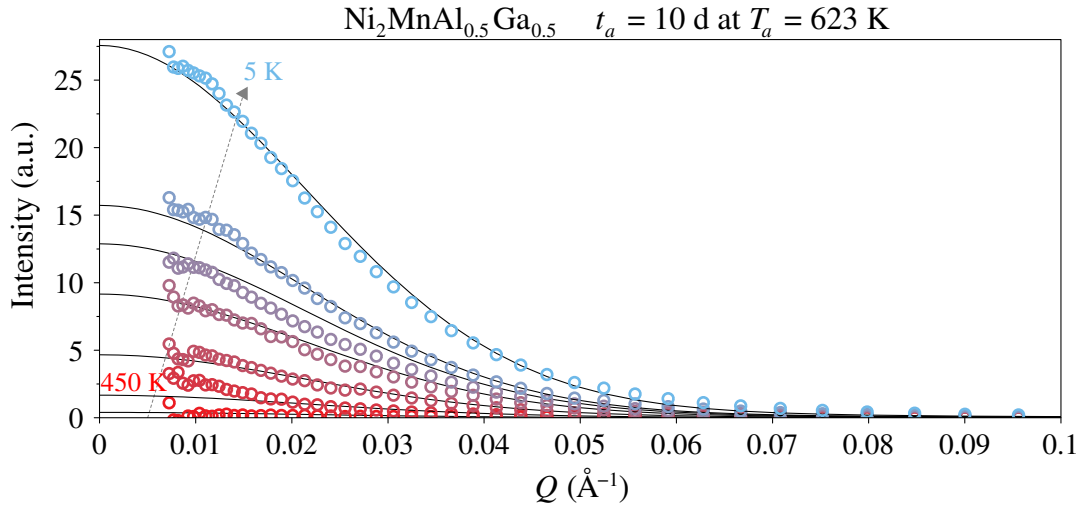


Figure 4.14: Difference spectra between the SANS profiles and the scattering signal at 450 K, $I_{450\text{K}}$, for the $\text{Ni}_2\text{MnAl}_{0.5}\text{Ga}_{0.5}$ sample 10 d annealed at 623 K on a linear scale. Depicted are the profiles at 5 K, 300 K, 340 K, 360 K, 380 K, 390 K and 400 K. The black lines correspond to the scaling functions $S(k)$ defined in Eq. (3.16).

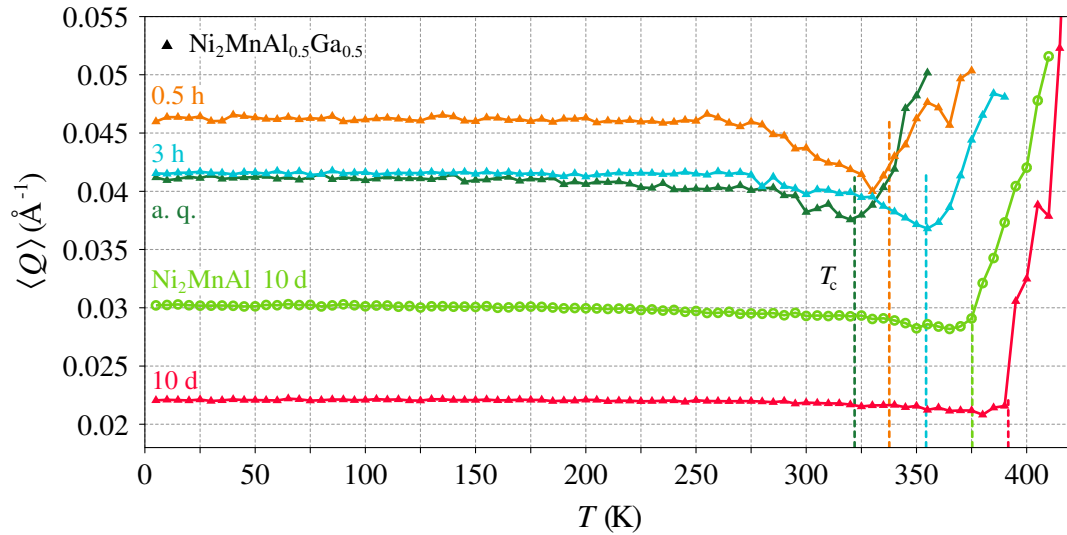


Figure 4.15: Mean $\langle Q \rangle$ of the difference spectra between the SANS profiles and the scattering signal at 450 K, $I_{450\text{K}}$. The positions of the transition temperatures are marked by dashed lines.

One explanation for this shift is the transition from magnetic scattering intensity to diffuse scattering intensity, as the magnetic contrast is lost with increasing temperature due to the decreasing coupling strength of the magnetic moments. With this loss of magnetic order the scattering intensity shifts towards higher Q as the neutrons are no longer scattered from a magnetic microstructure but disordered spins corresponding to more diffuse scattering. This continuous decrease in the intensity distribution within the ferromagnetic phase equals the second order transition of a ferromagnet to a paramagnet.

4.5 Conclusion

The results presented in this chapter demonstrate a strong correlation between the structurally ordered domains and the magnetic ones in Ni_2MnZ compounds. Using the same phenomenological model derived in Chap. 3 the data recorded by a neutron powder diffractogram could be directly compared to the results obtained from SANS profiles. The length scale of the structural order in these compounds is of the same size as the length scale of the magnetic order. Hence our observations agree with the Lorentz-TEM studies Yano et al. (2007) implying both domains to coincide.

Furthermore, the magnetic transition was investigated by comparing the temperature-dependent SANS data and the retrieved transition temperatures are in good agreement with DSC measurements of the same samples.

Finally a shift in intensity in the magnetic signal of the SANS profile was observed around the transition temperature. This shift is attributed to the transition from a magnetically ordered structure to a paramagnet, which results in a transition of the intensity distribution towards the high Q -regime.

Chapter 5

Anti-Ferromagnetic Coupling of Anti-Phase Domains

5.1 Introduction

In the previous chapter, the magnetic domains in the Ni_2MnZ compounds were observed to be the same size as the structurally ordered ones. These observations agree with TEM and Lorentz-TEM studies of thin Ni_2MnAl and $\text{Ni}_2\text{MnAl}_{0.5}\text{Ga}_{0.5}$ samples (Yano et al., 2007; Umetsu et al., 2011), which found the structural domains to be identical with the magnetic ones. In contrast to these measurements, the magnetic correlation lengths obtained from low-temperature neutron powder diffraction patterns were found to be much larger than the structural L2_1 order, as presented in Neibecker (2017). Fig. 5.1 displays in its upper panel the powder diffraction patterns of the $\text{Ni}_2\text{MnAl}_{0.5}\text{Ga}_{0.5}$ samples recorded well above their magnetic transition temperatures. These patterns were discussed in detail in the previous chapter and show broadened L2_1 reflections, with the corresponding structural correlation length being of the order of ~ 80 Å. In the lower panel of Fig. 5.1 the corresponding measurements below their magnetic transition temperatures at 200 K are displayed. Here we observe a sharp, strongly Q -dependent intensity contribution on top of the broadened L2_1 reflections. Due to its temperature- as well as its strong Q -dependence, this sharp additional contribution was identified to result from the magnetic order of the sample (Neibecker, 2017). For all annealing states, this signal is as sharp as expected from the calibration measurements, indicating a magnetic correlation length of at least 530 Å, which disagrees with the one obtained from the SANS measurements (~ 100 Å).

A detailed discussion of this signal and the low-temperature diffraction patterns is given in Neibecker (2017).

One possible explanation for these large deviations between the magnetic correlation lengths is the coupling between the magnetic domains. There are three possible scenarios for the magnetic exchange interaction across APBs:

In the first scenario, the spins located in two neighbouring APDs do not couple across their APB. Hence their exchange interaction is confined to the size of the respective APD. This case would correspond to spins coupling ferromagnetically inside an APD, forming ferromagnetic domains. These magnetic domains would compare to isolated superspins, which couple paramagnetically to an external magnetic field. Without any exchange interaction between the superspins, they would be randomly orientated in case of no preferred orientation given by an external magnetic field. Hence the magnetic microstructure would correspond to large magnetic inhomogeneities, as observed in the SANS measurements. For the neutron powder diffraction measurements, this case would lead to broadened magnetic reflections similar to the $L2_1$ superstructure peaks, which is inconsistent with our observations in the low-temperature powder diffraction patterns.

In the second scenario, the superspins interact ferromagnetically across the APBs. Here, the magnetic order would be not confined to the APD size but persist through the sample similar to a macroscopically ferromagnetic system. This case would contradict our observation from the SANS measurements as no magnetic inhomogeneities would exist in this scenario. For the neutron diffractogram, this case would correspond to an additional magnetic contribution on the peak intensities at low Q but leave the peak width as determined by the structural order unchanged, thus disagreeing with our observations.

In the last scenario, the superspins of neighbouring APDs interact anti-ferromagnetically across the APB, while the spins located in the same APD interact ferromagnetically with each other. Here the exchange interaction would be long-range, as the spin coupling is not confined to the APD size and would persist through the adjacent domains due to the couplings of the spin across the APBs. Hence this third case would correspond to magnetic structures of the mesoscopic length scale, as we observed in SANS. But the exchange interaction also leads to a much larger correlation length of the magnetic order than the correlation length of the structural order. A detailed discussion of the implications of this AFM-like coupling of APDs for the neutron powder diffractogram is given in Neibecker (2017), with this case leading to

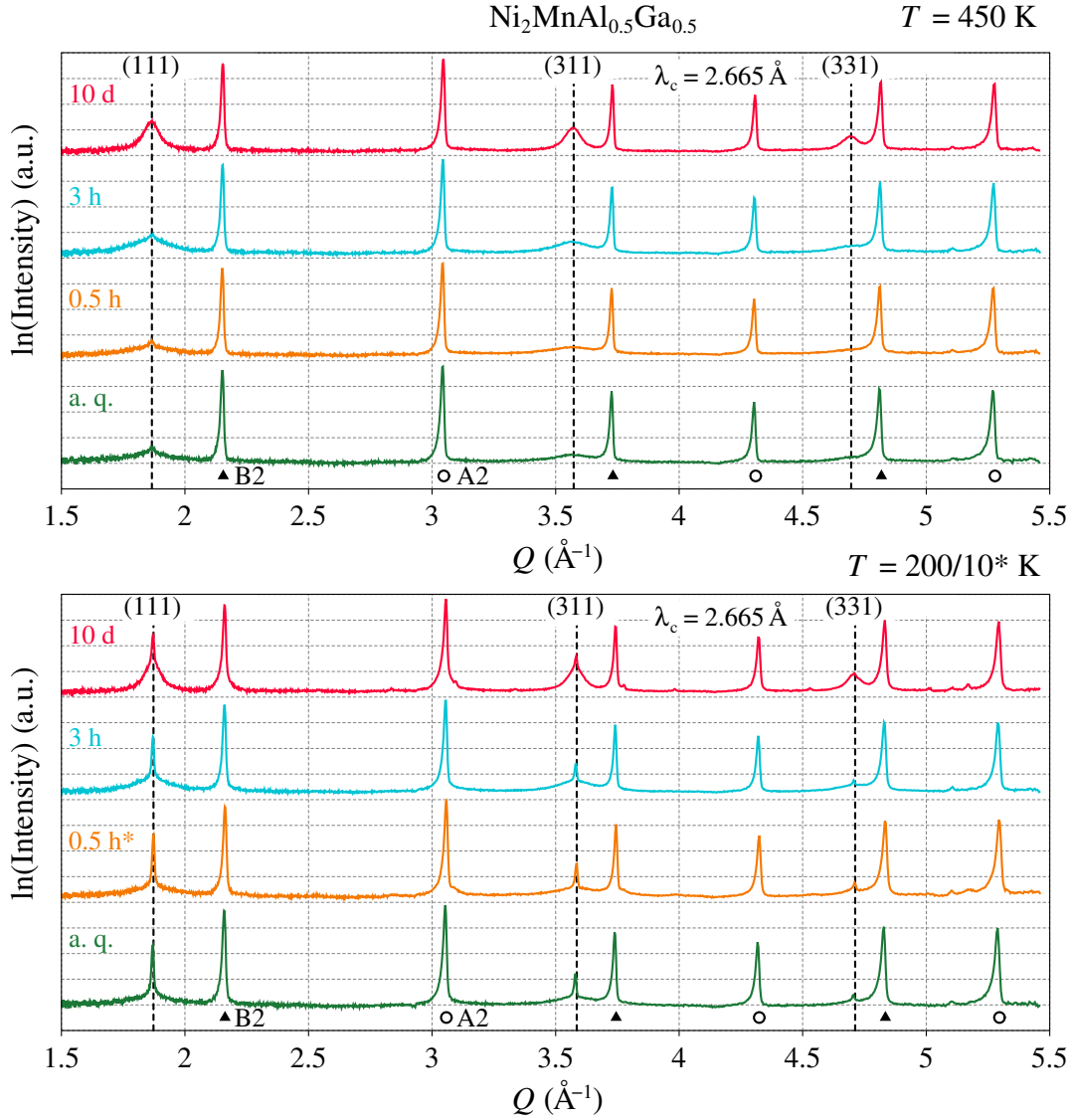


Figure 5.1: Neutron powder diffraction patterns of the $\text{Ni}_2\text{MnAl}_{0.5}\text{Ga}_{0.5}$ powder samples of distinct L_{21} order states using a center wavelength of $\lambda_c = 2.665 \text{ \AA}$: in the upper panel the measurements at 450 K, above the magnetic transition temperatures, are shown, while in the lower panel the diffraction data recorded below the respective T_c , at 200 K, are displayed. The dashed lines denote the position of the L_{21} reflections, while the positions of the fundamental Bragg peaks of A2 and B2 order are indicated by circles and triangles.

a sharp additional intensity on top of the $L2_1$ reflections just as we observe in the low-temperature diffraction patterns.

This last case is the most interesting one as it corresponds to our simple model of the magnetic coupling in Ni_2MnZ compounds being only dependent on the structural order of the Mn atoms. For example, in Lorentz-TEM measurements, a reversal of the magnetisation at the APBs was observed (Yano et al., 2007). Still, until now, this coupling across structural domain boundaries has not been studied in bulk Ni_2MnZ samples.

To distinguish between these three coupling across the APBs scenarios further, the SANS signal of the powder samples was investigated with an external magnetic field applied. Without a magnetic field, the SANS signal of the powder samples was, as expected, isotropic. Due to the neutrons' exchange interaction with the average spin component in the direction $\boldsymbol{\eta}$, S^η , a quantity proportional to the magnetisation of the sample, the magnetic scattering intensity is proportional to the difference between unity and the scalar product of the wavevector transfer \boldsymbol{Q} and $\boldsymbol{\eta}$, $I \propto (1 - (\boldsymbol{Q} \cdot \boldsymbol{\eta})^2)$ as given in Eq. (4.16). Hence only magnetic inhomogeneities with a magnetisation component perpendicular to \boldsymbol{Q} have a non-zero contribution to the scattering intensity. The magnetic scattering intensity in case no magnetic field is applied corresponds to the contribution of 2/3 of the sample's spins due to the random orientation of the grains.

If a magnetic field is applied, the spins of ferromagnetic domains align parallel to the magnetic field direction. The main spin component of the sample $\boldsymbol{\sigma}$ corresponds to the sum over all spins in the sample and is in this case parallel to \boldsymbol{B} . Hence the SANS signal of a ferromagnet becomes anisotropic with intensity being shifted in the direction perpendicular to the magnetic field (Wagner et al., 1991). Thus for the first scenario of the magnetic coupling across APBs we would expect a shift of intensity with less intensity in the direction parallel to the \boldsymbol{B} -field and more in the direction perpendicular to it.

We expect the domains to respond to the external magnetic field like a Heisenberg anti-ferromagnet for the third scenario. The energy of an anti-ferromagnetic arrangement is minimal, if the angle between the magnetisations \boldsymbol{M}_A and \boldsymbol{M}_B of the respective sublattices is $2\alpha = 180^\circ$, with $E \propto M^2 \cos(2\alpha)$, as sketched in Fig. 5.2 on the left. Suppose an external magnetic field $\boldsymbol{B}_{\text{ext}}$ is applied to an arrangement of anti-ferromagnetic spins; in that case, an additional term, the Zeeman term, has to be considered with the spins of both sublattice wanting to be aligned in the field

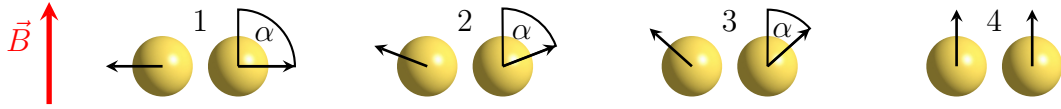


Figure 5.2: Action of an external magnetic field \mathbf{B} on an anti-ferromagnet, the coupled spins align perpendicular to the \mathbf{B} -field under the angle α . The magnetic field increases from state 1, corresponding to a small magnetic field, to state 4, corresponding to the spin state with a very high magnetic field being applied.

direction. Hence the energy of the system is given as $E \propto M^2 \cos(2\alpha) + BM \sin(\alpha)$. Here the energy minimum is obtained if the spins align perpendicular to the external magnetic field, since this spin arrangement allows an antiparallel alignment to its neighbouring spin as well as a parallel alignment to the magnetic field under a certain angle α (Neel, 1952), as sketched in state 1 of Fig. 5.2. With increasing magnetic field, the spins can be turned more and more in field direction, as sketched in states 2 and 3 of Fig. 5.2, until for high enough fields, the spins are completely aligned in field direction, resulting in a polarised spin state, as displayed in the state 4 of Fig. 5.2. Thus for this coupling of the APDs across APBs scenario, we would expect the super spins σ_i , corresponding to the mean magnetisation direction of a single domain, to align perpendicular to the magnetic field direction at a low magnetic field. Hence the expected SANS signal would show a shift of intensity in the field direction.

Investigating the SANS signal close to the magnetic transition temperature as well as under high magnetic fields allows us to study the interplay and strength of the magnetic exchange interactions of the spins located in neighbouring APDs as well as their coupling to an external magnetic field.

5.2 Isothermal Measurements Under High Magnetic Fields

In order to investigate the coupling mechanism between the magnetic domains in Ni_2MnZ alloys, small-angle neutron scattering measurements were performed on the $\text{Ni}_2\text{MnAl}_{0.5}\text{Ga}_{0.5}$ powder samples with a magnetic field of up to 4 T applied. The measurements were conducted at SANS-1 at the FRM II, Garching, at a sample-detector distance of 8 m. Using unpolarised neutrons of a wavelength of 5 Å allowed us to access a Q -range of $[0.007, 0.11] \text{ Å}^{-1}$. We collected the data during several isothermal sweeps of the magnetic field between 0 T and 4 T in a temperature range of 50 K to 315 K. Similar to the measurements discussed in the previous chapter,

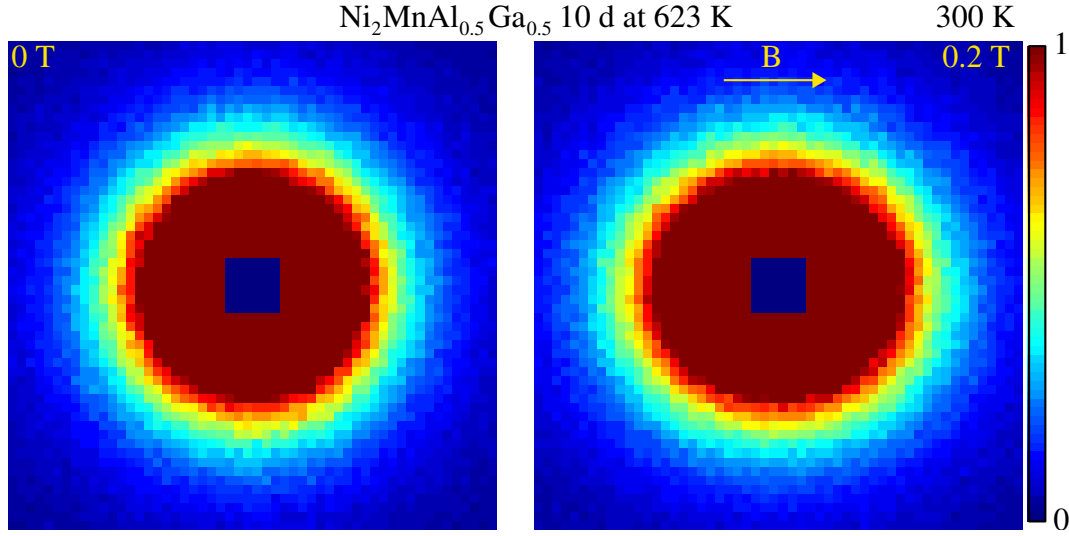


Figure 5.3: 2D SANS signal of the $\text{Ni}_2\text{MnAl}_{0.5}\text{Ga}_{0.5}$ sample annealed for 10 d at 623 K with no magnetic field and with a magnetic field of 0.2 T applied, measured at 300 K.

we observe no difference between the samples' profiles measured during heating or cooling.

In Fig. 5.3 the 2D SANS signals of the $\text{Ni}_2\text{MnAl}_{0.5}\text{Ga}_{0.5}$ sample with the longest annealing duration of ten days are shown for no and a small magnetic field of 0.2 T applied at 300 K. Comparing both signals, we observe a clear redistribution of intensity from the isotropic picture in case of no external magnetic field to an anisotropic signal in case of a non-zero magnetic field, with more intensity in the direction parallel to the magnetic field. Hence the spins of the sample show a behaviour similar to a Heisenberg anti-ferromagnet, with its scattering signal indicating that the main spin component σ_i of a single domain is perpendicular to the magnetic field. This observation confirms our theoretical model of the spin coupling in Ni_2MnZ alloys, with the spins interacting ferromagnetically inside an APD, while the ferromagnetic domains couple anti-ferromagnetically to each other across the APBs.

The radial average of the scattering signals at 300 K with distinct magnetic fields between 0 T and 4 T applied is shown in Fig. 5.4 a). At zero magnetic field we observe the same characteristic magnetic signal, which was discussed in detail, in the previous chapter 4. With an increasing magnetic field, this signal shifts towards higher Q and decreases in intensity.

In order to study the anisotropy of the magnetic signal quantitatively, we take the radial average of the intensity in the horizontal and the vertical direction. The distinct regions of the 2D signal which contribute to each profile are shown in the inset of

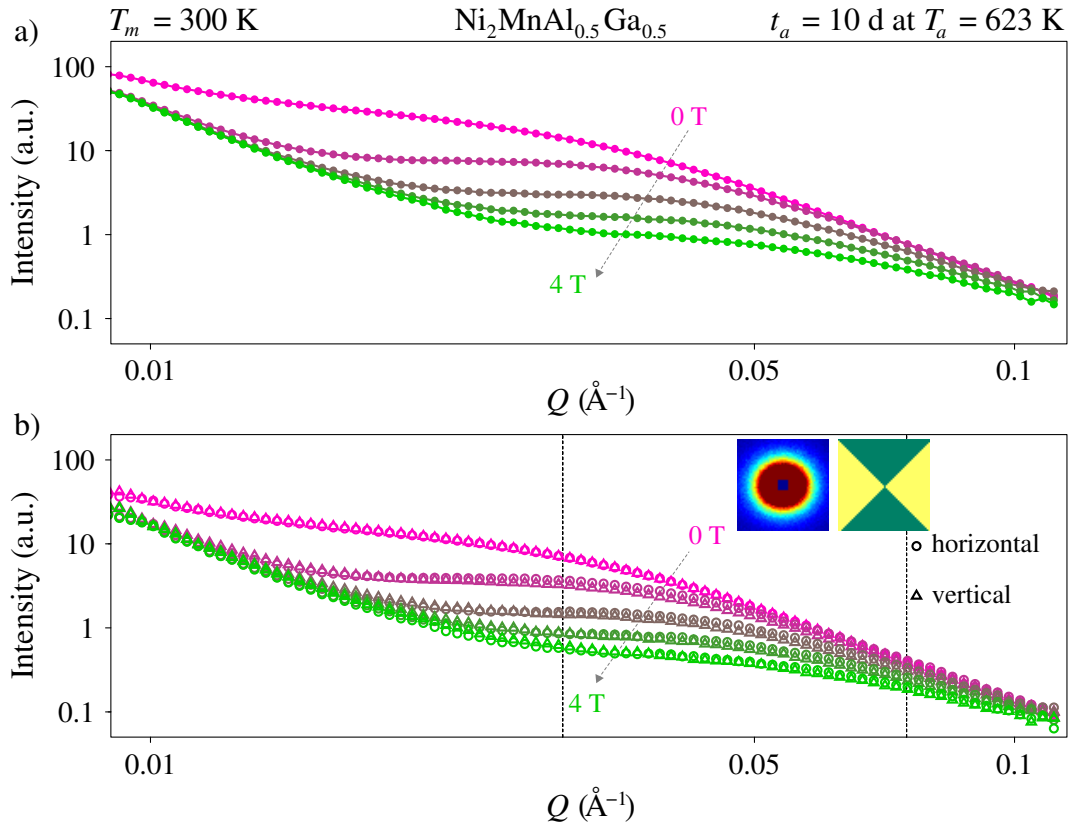


Figure 5.4: Radially averaged SANS-profiles at 300 K of the 10 d annealed $\text{Ni}_2\text{MnAl}_{0.5}\text{Ga}_{0.5}$ sample under 0 T, 1 T, 2 T, 3 T and 4 T, depicted in a). The respective radially averaged SANS-profiles in the horizontal and vertical direction are shown in b). The dashed lines mark the Q -range, in which anisotropy of the signal is evaluated.

Fig. 5.4 b), with the corresponding direction-dependent profiles being displayed in Fig. 5.4 b). If no external magnetic field is applied, both profiles show an identical intensity distribution. In the case of a non-zero external magnetic field, the profile in the horizontal direction ($\parallel \mathbf{B}_{\text{ext}}$), depicted as circles in Fig. 5.4 b), displays more intensity than the profile in the vertical direction ($\perp \mathbf{B}_{\text{ext}}$), depicted as triangles, around the centre of the magnetic signal, sketched by the dashed lines in Fig. 5.4 b).

Taking the integral of these profiles around the centre of the magnetic signal allows us to investigate the coupling of the sample's spins with each other and the external magnetic field closer. The integral is evaluated in the Q -range $[0.03, 0.075] \text{ \AA}^{-1}$, with the range being sketched in Fig. 5.4 b). We performed isothermal scans of the magnetic field at 50 K and 300 K for the $\text{Ni}_2\text{MnAl}_{0.5}\text{Ga}_{0.5}$ sample 10 d annealed and the evolution of the integrated intensity is shown in Fig. 5.5 a). For both temperatures, we observe the same qualitative behaviour: For small magnetic fields, the total intensity increases before decreasing with increasing magnetic field, as indicated in the radial averages shown in Fig. 5.4.

The respective integrals of the direction-dependent profiles are shown in Fig. 5.5 b). For the integral parallel to the field direction, we observe an intensity maximum at 0.3 T and 0.2 T, respectively. In contrast, the vertical intensity integral decreases continuously with increasing magnetic field. The integral in field direction is in general larger than the one perpendicular to the magnetic field, with their intensity ratios being depicted for both temperatures in Fig. 5.5 c). Furthermore, their ratio is a quantity proportional to the magnetisation direction of a single domain, as it indicates the direction main spin component on the mesoscopic length scale. With increasing magnetic field, it decreases for both isothermal measurements.

Comparing the scans at 50 K and 300 K, we observe a distinctly stronger intensity integral as well as anisotropy in the lower temperature B -scan, which is due to the strength of the magnetic signal being temperature-dependent, as discussed in Chap. 4.4.2. At low temperatures, the signal at zero magnetic field shows signs of a remaining anisotropy in field direction, with the integral ratio being larger than 0.5. This observation indicates that a preferred spin alignment perpendicular to the magnetic field remains in the sample even after applying a magnetic field.

For the as-quenched $\text{Ni}_2\text{MnAl}_{0.5}\text{Ga}_{0.5}$ sample B -scans were recorded at 50 K, 130 K, 200 K, 270 K, 305 K and, close to the magnetic transition temperature, at 315 K. Their integral ratios are displayed in the lower panel of Fig. 5.5 d) and show the same qualitative behaviour as the ones of the 10 d annealed sample. The anisotropy maximum

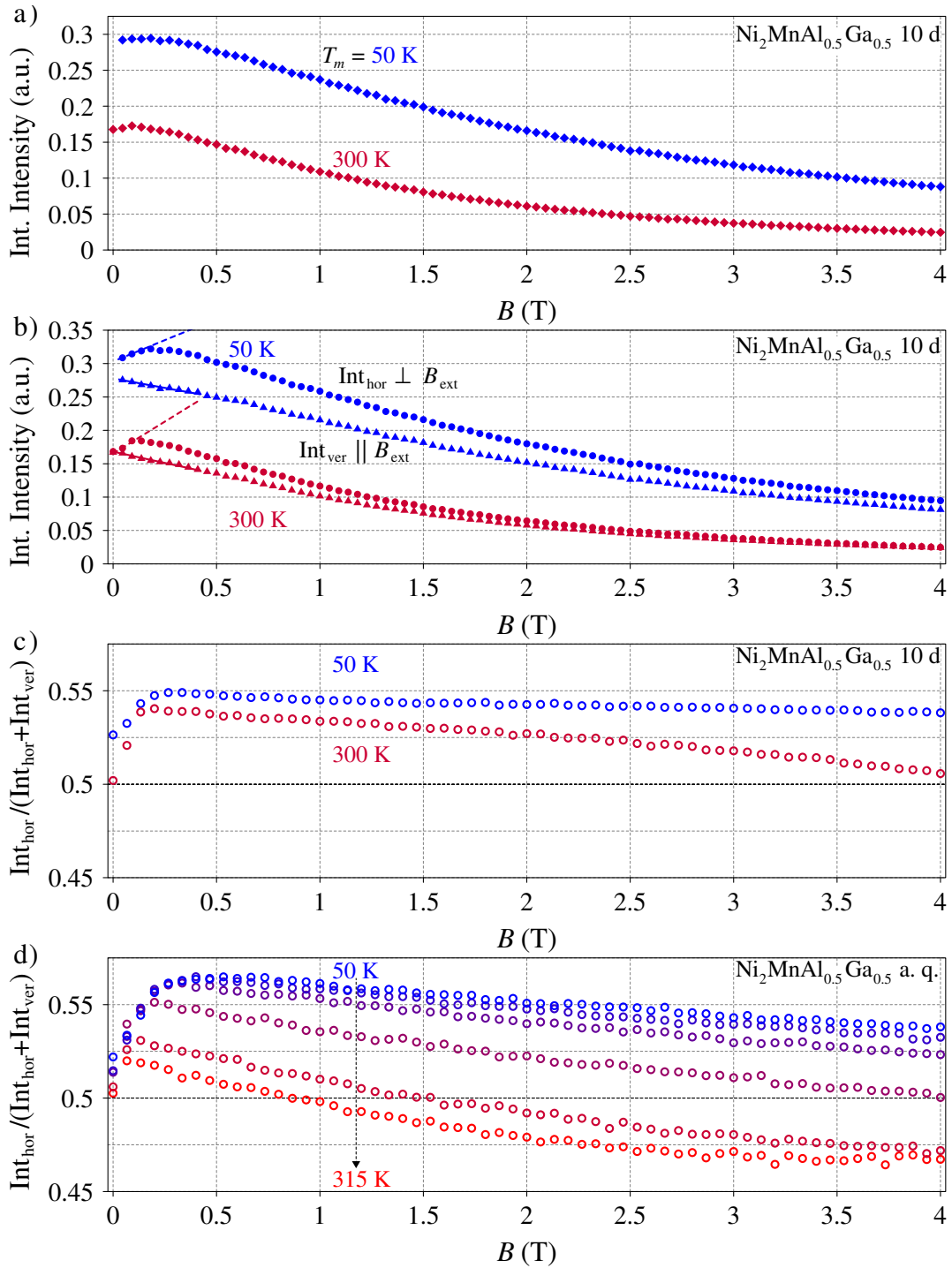


Figure 5.5: The integrals of the SANS profiles for the scan of the magnetic field at 50 K and 300 K for the $\text{Ni}_2\text{MnAl}_{0.5}\text{Ga}_{0.5}$ sample 10 d annealed are shown in a). The respective integrals in the horizontal and vertical direction are shown in b), with the corresponding integral ratios being depicted in c). For the as-quenched $\text{Ni}_2\text{MnAl}_{0.5}\text{Ga}_{0.5}$ sample B -scans were recorded at 50 K, 130 K, 200 K, 270 K, 305 K and, close to the magnetic transition temperature, at 315 K and the corresponding integral ratios are shown in d).

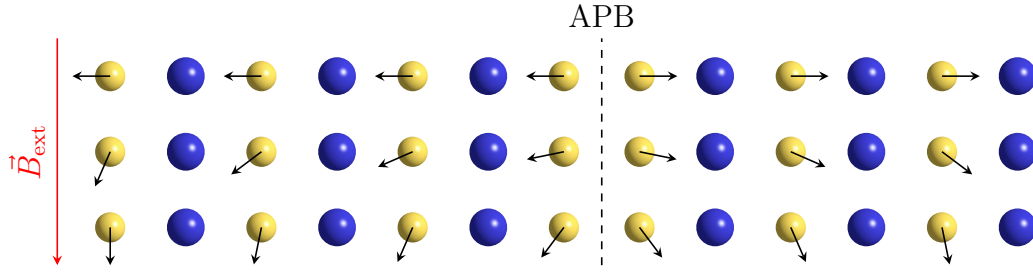


Figure 5.6: 1D sketch of antiferromagnetically coupled APDs with increasing magnetic field. The APB is sketched by the black dashed line.

shifts with decreasing temperature towards higher magnetic fields, starting from 0.1 T for the signal close to the magnetic transition temperature, $T_c = 322$ K, and shifts to 0.3 T for the scan at 50 K. For the scans close to T_c , we observe a continuous transition of the anisotropy from more intensity in the direction parallel to the \mathbf{B} -field to more intensity in the direction perpendicular to it.

The increase of the total intensity for small magnetic fields applied can be explained by considering the geometry of the experiment setup. We measured the signal in the $Q_x \times Q_y$ -plane. Without a magnetic field, the spins in the powder sample have no preferred direction and are therefore randomly distributed. However, due to the neutron's magnetic interaction with the spins, only $2/3$ of the spins contribute to the scattering signal in Q_x and Q_y direction. If all spins were aligned in the z -direction, the intensity of the signal would be at its maximum, 1 in both directions, as the main spin component of the sample is in this case orthogonal to all possible \mathbf{Q} , which can be recorded.

If a small external magnetic field is applied in x -direction, the spins of an anti-ferromagnet align preferably perpendicular to it, thus having their main spin components in y and z direction. Hence we expect a shift of intensity, with the intensity in field direction increasing from a factor of $2/3$ to a factor of 1 since the spins aligned in y and z direction contribute to the scattering intensity measured in x direction. With no spins being aligned along the x direction, only the intensity of spins aligned in z contribute to the intensity perpendicular to the magnetic field (Q_y). Therefore the intensity along Q_y decreases from a factor $2/3$ to a factor $1/2$. With the intensity of one direction of the signal increasing twice as much as decreasing in the other, as shown in Fig. 5.4 b), we observe the total intensity to increase for small magnetic fields. The decrease in intensity of the magnetic signal as well as its shift towards higher Q with the increasing magnetic field is very similar to the temperature-dependent behaviour of the SANS-signal discussed in the previous chapter 4.4.2. To explain this shift, we

need to consider the different coupling strengths inside the domain. In the case of the temperature-dependent signal, we found that, with increasing temperature, the intensity of the SANS signal decreases due to the decrease of the magnetic contrast in the sample. In Chap. 4.4.2 we assumed the shift to be due to increasing magnetic disorder which leads to a loss of intensity in the scattering signal at low Q , corresponding to scattering of structures on the mesoscopic length scale, and an increasing diffusive scattering intensity in the high Q -regime. In the case of an external magnetic field, the same model applies; only now the spins inside a domain are not disordering but aligning parallel to the field. Likewise to the previous scenario, the magnetic contrast is lost, resulting in a loss of intensity in the scattering signal. However, in this case the scattering of the spins inside a domain is not diffusive but results from the scattering of a ferromagnetic alignment. Hence the intensity of the Bragg peak increases in the low Q -regime, which cannot be observed in these SANS measurements directly but only as the intensity loss of our magnetic signal. This process is sketched in Fig. 5.6, where three states of a 1D representation of anti-ferromagnetically coupled APDs with an increasing magnetic field are displayed.

Close to T_c , we observe a transition of the anisotropy from more intensity in the horizontal direction to the vertical one. Here the effects of temperature and magnetic field on the spin coupling have to be considered. To study this linear transition closer, further magnetic SANS measurements at high temperatures were performed and will be discussed in the next section.

5.3 Temperature-Dependent Measurements

In order to study the magnetic coupling in APDs with temperature as well as an external magnetic field, high temperature magnetic SANS measurements were performed in a temperature range of 50 K to 500 K at the instrument D33 at the ILL, Grenoble. Since the magnetic signal of samples of a shorter annealing duration is located at higher Q and shifts with an increasing magnetic field towards higher Q , a Q -range of $[0.02, 0.28] \text{ \AA}^{-1}$ was investigated using a sample-detector distance of 2 m as well as neutrons of the wavelength of 5 Å. We applied magnetic fields of up to 640 mT in the x -direction, perpendicular to the incoming neutron beam, and performed isomagnetic temperature sweeps as well as isothermal scans of the magnetic field. The measured scattering signals were recalibrated as described in the appendix B.

The SANS profiles measured at SANS-1 fit perfectly to the SANS profiles measured at D33, as depicted in Fig. 5.7 for the $\text{Ni}_2\text{MnAl}_{0.5}\text{Ga}_{0.5}$ sample 10 d annealed for the pro-

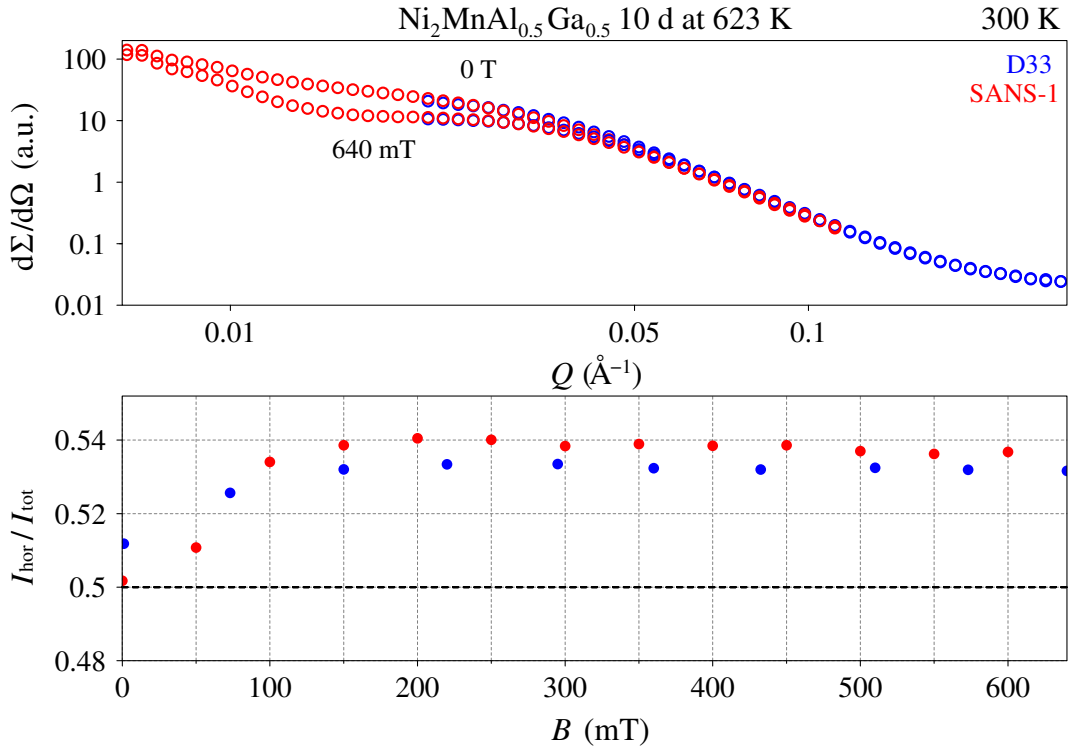


Figure 5.7: Radially averaged SANS profiles of the $\text{Ni}_2\text{MnAl}_{0.5}\text{Ga}_{0.5}$ sample 10 d annealed were measured at 300 K without an external magnetic field at SANS-1 for a sample-detector distance of 8 m and at D33 for a sample-detector distance of 2 m.

files recorded at 300 K without a magnetic field and with a magnetic field of 640 mT applied. The profiles measured at the respective instruments are scaled according to their sample-detector distance, their detector area and pixel area. Their respective anisotropies were analysed by taking the ratio of the integral in the horizontal direction and the total intensity Int_{tot} ($\text{Int}_{\text{tot}} = \text{Int}_{\text{hor}} + \text{Int}_{\text{ver}}$). The integrals were obtained for the same Q -range and are for both instruments in good agreement, as shown in the lower panel of Fig. 5.7.

Since the location of the magnetic signal depends on the $L2_1$ order state for the Ni_2MnZ compounds, the integrals to study the anisotropy were taken for shorter annealing durations in a Q -range of $[0.05, 0.1] \text{\AA}^{-1}$. In contrast, for the longest annealed $\text{Ni}_2\text{MnAl}_{0.5}\text{Ga}_{0.5}$ sample a Q -range of $[0.03, 0.075] \text{\AA}^{-1}$ was chosen. The evolutions of the anisotropy with temperature as well as magnetic field are depicted for all annealing states of the $\text{Ni}_2\text{MnAl}_{0.5}\text{Ga}_{0.5}$ powder samples in Fig. 5.8, Fig. 5.9 as well as Fig. 5.10. For measurements at high temperatures ($\gg T_c$) we expect the signal to be isotropic since, as the sample becomes paramagnetic, the large magnetic inhomogeneities vanish. Here small anisotropies of the signal were observed, for

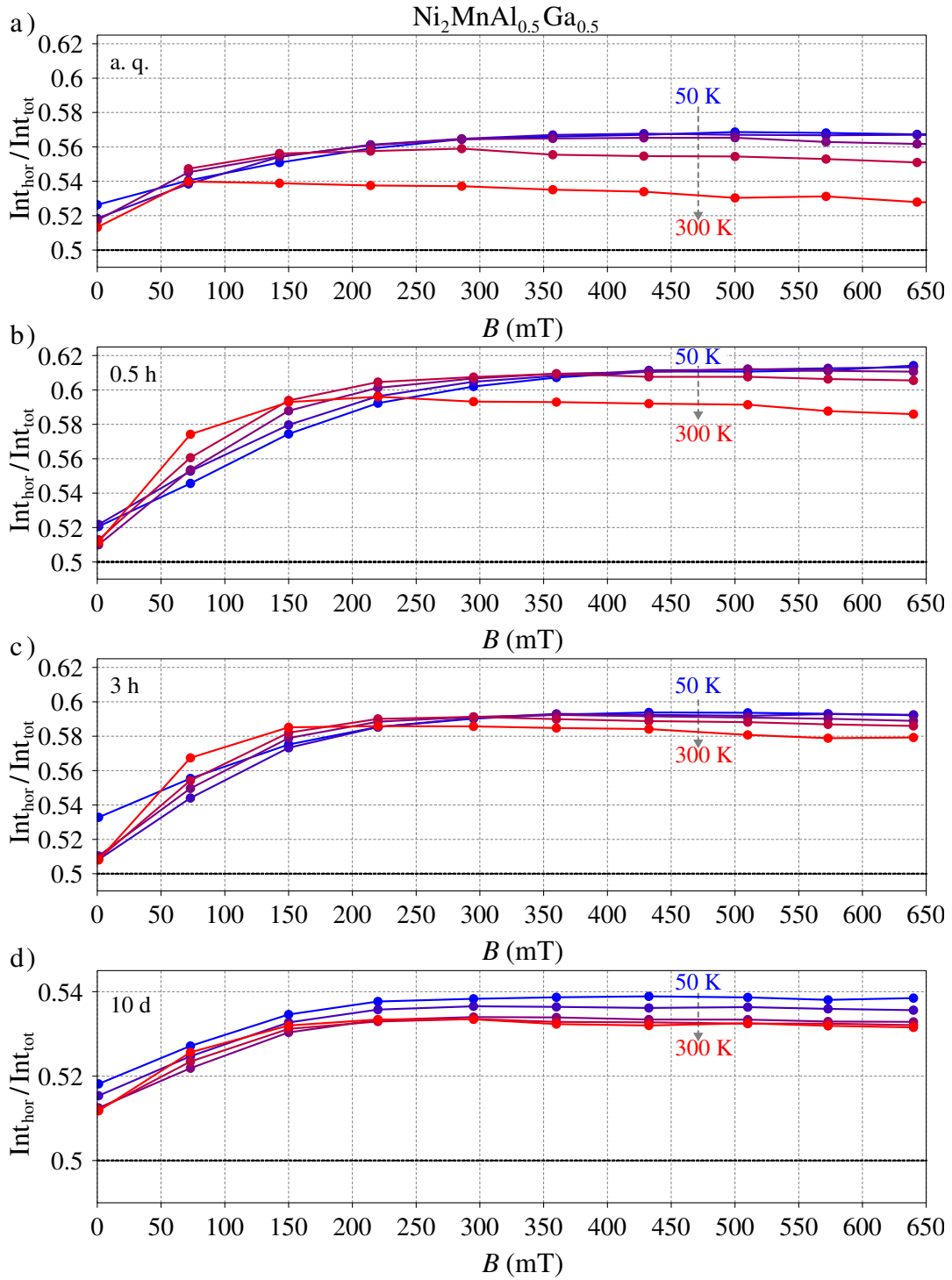


Figure 5.8: Isothermal sweeps of the magnetic field at 50 K, 130 K, 200 K, 250 K and 300 K of the $\text{Ni}_2\text{MnAl}_{0.5}\text{Ga}_{0.5}$ powder samples a) as-quenched, b) 0.5 h, c) 3 h and d) 10 d annealed at 623 K. The ratios of the intensity integral in horizontal direction to the total integrated intensity ($\text{Int}_{\text{hor}}/\text{Int}_{\text{tot}}$) of the as-quenched sample were retrieved from the measurements at SANS-1, while for the other samples this ratio was obtained from measurements conducted at D33. The solid lines are a guide to the eye. The remanence is due to the order of the measurements, for example the measurements of the 10 d sample were recorded during field cooling. Int_{tot} is defined as the sum of Int_{hor} and Int_{ver} .

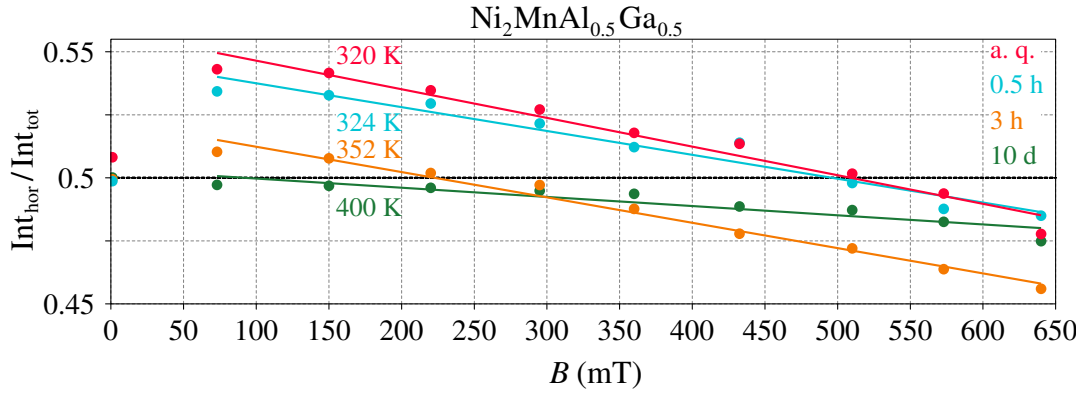


Figure 5.9: Evolution of the ratio of the integrals of the direction dependent profiles with the magnetic field close to the magnetic transition temperatures of 322 K, 338 K and 354 K of the respective $\text{Ni}_2\text{MnAl}_{0.5}\text{Ga}_{0.5}$ powder samples as-quenched, 0.5 h and 3 h annealed at 623 K. Linear fits of the respective curves are depicted as solid lines.

which we corrected by adding a small constant contribution to all horizontal integrals. For low temperatures, this contribution does not affect the resulting anisotropies as the signal is much stronger than at high temperatures.

These isothermal measurements, depicted in Fig. 5.8, show independent of the annealing state the same characteristic behaviour: Well below the magnetic transition temperature we observe more intensity in the horizontal direction (\parallel to B) than in the vertical one. Above the magnetic transition temperature, the scattering signal is isotropic, with the ratio between the horizontal integral to the total intensity being 0.5. The remanence observed for the samples is due to the order in which the measurements were recorded. For the 10 d annealed samples all measurements were recorded for field cooling, decreasing the magnetic field from 640 mT to 0 mT. In the case of the 3 h sample, the measurements at 50 K were recorded while field cooling, while the respective measurements at 300 K were performed during field heating. When approaching the magnetic transition temperature, we observe the same continuous transition of the anisotropy as we did in the measurements at SANS-1 when applying high magnetic fields for the as-quenched sample displayed in Fig. 5.5 d). Fig. 5.9 shows the evolution of the anisotropy close to T_c for the as-quenched, 0.5 h and 3 h annealed $\text{Ni}_2\text{MnAl}_{0.5}\text{Ga}_{0.5}$ samples. Here the anisotropy decreases linearly with increasing magnetic field and becomes smaller than 0.5, indicating a change in the main spin component of the sample from perpendicular to the B -field to parallel to it. Hence we can turn the main spin component in field direction either with high enough fields as in the case of the measurements at SANS-1 or at temperatures close to T_c with lower fields.

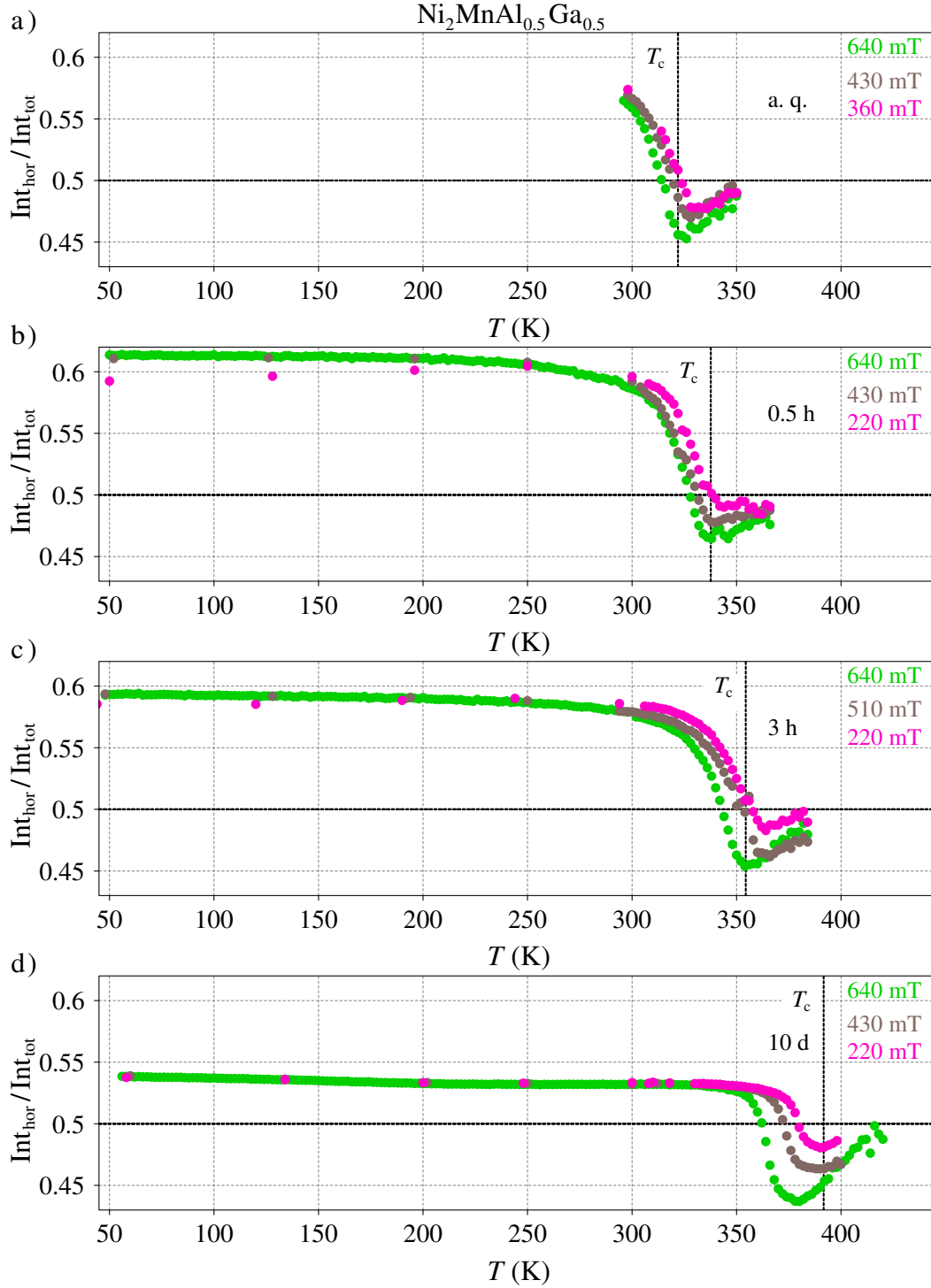


Figure 5.10: Evolution of the ratio of the integrals of the direction dependent profiles with temperature for a magnetic field of 640 mT, 430 mT and 220 mT of the $\text{Ni}_2\text{MnAl}_{0.5}\text{Ga}_{0.5}$ powder samples as-quenched, 0.5 h, 3 h and 10 d annealed at 623 K.

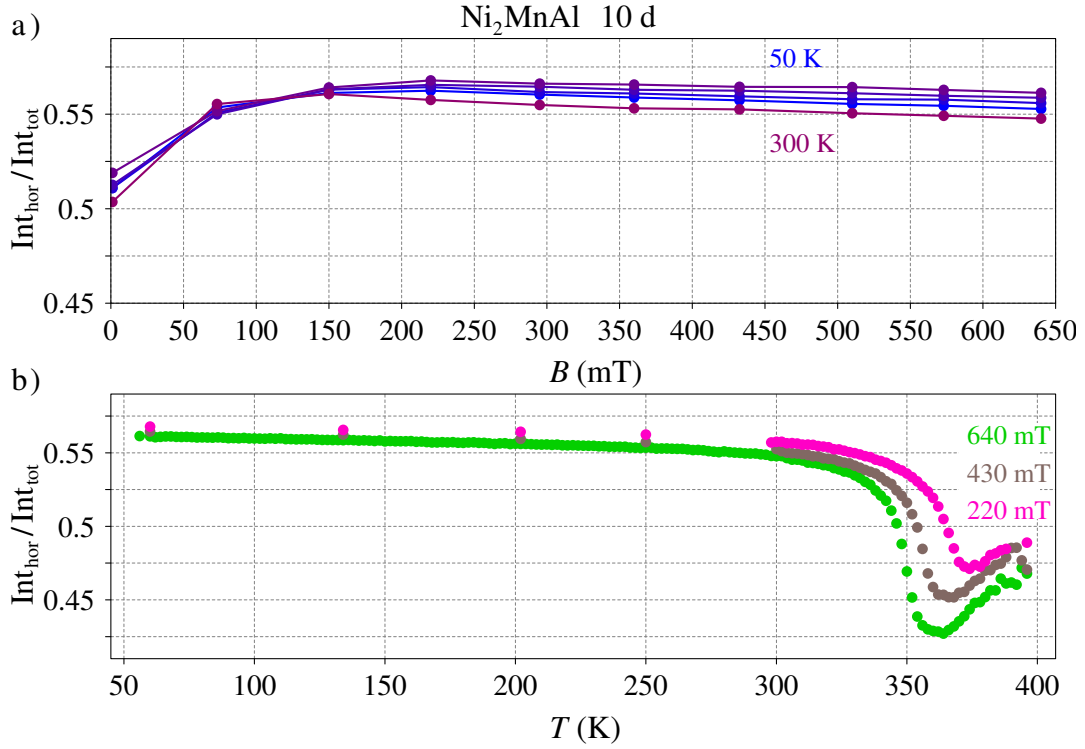


Figure 5.11: Evolution of the integral ratio of the direction dependent profiles for the Ni_2MnAl sample 10 d annealed with a) increasing magnetic field at 50 K, 130 K, 200 K, 250 K, 300 K, 400 K, 450 K and 500 K. In b) its evolution with temperature for a magnetic field of 640 mT, 430 mT and 220 mT are shown.

Fig. 5.10 shows the evolution of the anisotropy of the scattering signal with temperature while a constant magnetic field is applied. For all $\text{Ni}_2\text{MnAl}_{0.5}\text{Ga}_{0.5}$ samples we observe the same characteristic behaviour: The anisotropy is constant for temperatures well below the respective T_c with more intensity in the horizontal than vertical direction. When approaching the transition temperature, the anisotropy decreases until, close to T_c , it changes to be smaller than 0.5. For temperatures well above T_c the scattering signal becomes isotropic, with the ratio of the direction dependent profiles being one. These two phase transitions of the anisotropy are visible in all samples as well as for different magnetic field values. With increasing magnetic field, the transitions shift towards lower temperatures as well as anisotropy in the second phase becomes larger, as shown in Fig. 5.8 d).

Comparing between the distinct annealing states of the $\text{Ni}_2\text{MnAl}_{0.5}\text{Ga}_{0.5}$ samples we observe the scattering signal of the longest annealed sample to be the least anisotropic one at low temperatures as well as experiencing close to T_c the strongest anisotropy perpendicular to the magnetic field.

The evolution of the anisotropy for the Ni_2MnAl sample 10 d annealed at 623 K is depicted in Fig. 5.11 a) for the isothermal measurements and in b) for a constant B -field. We observe the same characteristic behaviour as for the $\text{Ni}_2\text{MnAl}_{0.5}\text{Ga}_{0.5}$ samples.

The ratio of all samples is at low temperatures greater than 0.5, which indicates the main spin component of the domains being perpendicular to the magnetic field. Hence the response of the spins located in the domains for all distinct $L2_1$ order states as well as both alloy families corresponds to that of a Heisenberg anti-ferromagnet, indicating an anti-ferromagnetic coupling of the APDs across their APBs. Above the magnetic transition temperatures, the samples become paramagnetic, thus losing the magnetic microstructure and leading to isotropic scattering signals.

To explain the linear decrease of the anisotropy at a constant temperature close to T_c , shown in Fig. 5.9, the competing forces acting on the spins have to be considered: According to the Heisenberg model, the energy of the exchange interaction of the atoms i, j with the electron spins S_i, S_j is given by $U_H = -2JS_i \cdot S_j$. This term depends on the alignment of the spins to each other. Hence, it is sensitive to the fluctuations of the spins, which contribute quadratically. If a magnetic field is applied, also the interaction of the magnetic moments with an external magnetic field has to be considered via the so-called Zeeman-term, $U_{\text{Zeeman}} = g_S \frac{\mu_B}{\hbar} \mathbf{S} \cdot \mathbf{B}_{\text{ext}}$. At low temperatures, the spins are stiff, with only small deviations from their ground-state. The Heisenberg term here dominates, and it is even at high fields not possible to change the antiparallel alignment of the spins, as we observed in the previous section Fig. 5.5a). With increasing temperature, the spins fluctuate around their ground-state alignment due to thermal excitations. These fluctuations result in a parabolic decrease of the influence of the spin stiffness for the interaction between two magnetic moments ($U_H \propto |S|^2$). The Zeeman term decreases linearly with the spin stiffness, hence at temperatures close to T_c as well as high magnetic fields, this term dominates, resulting in a change of the main spin direction to parallel to the magnetic field, as sketched in Fig. 5.6.

In case of a constant magnetic field applied, we observe two magnetic transitions: At low temperatures, the spins inside an APD align antiparallel to the spins in the neighbouring APDs. With increasing temperature, the spins begin to fluctuate, with the fluctuations of the spins located inside the domain being stronger than for the spins located at the APB according to our model, presented in Chap. 4. When approaching the respective T_c the Zeeman term dominates, resulting in the spins inside an APD

to align parallel to the magnetic field. The more spins are turned in the field direction, the easier it is to spin-polarize the remaining spins due to their ferromagnetic exchange interaction. Hence for the isomagnetic transition, we observe a steeper transition of the anisotropy. This change in the anisotropy corresponds to the transition from an antiparallel alignment of the spins across APBs to the spin polarised case, sketched in Fig. 5.6. As the temperature increases further, this polarised spin alignment becomes disordered as the sample becomes paramagnetic, resulting in an isotropic scattering signal.

5.4 Conclusion

Using magnetic SANS measurements the coupling of the magnetic domains across APBs in Ni_2MnZ compounds was investigated. Due to the anisotropy of the magnetic scattering signal in the case of an applied magnetic field, we observed the domains to behave similar to a Heisenberg anti-ferromagnet, indicating the spins located in neighbouring APDs to couple anti-ferromagnetically across their APB.

With increasing magnetic field, the magnetic scattering signal shifts towards higher Q and its intensity decreases similar to its behaviour with increasing temperature, discussed in Chap. 4.4.2. Hence we were able to study the coupling strengths of the spins inside a domain; we found the model given for the temperature-dependence to be valid for this case as well, with the spins inside a domain breaking from the order of the domain earlier than the ones located at the APB.

With increasing temperature, we observed two magnetic transitions in the samples: first from the antiparallel alignment of the domains to a spin polarised case when approaching the respective magnetic transition temperature and the transition from this spin polarised state to a disordered paramagnetic one above the T_c .

Chapter 6

Summary

Throughout this thesis, the atomic ordering process and its influence on the magnetic properties in Ni_2MnZ Heusler alloys were investigated.

In chapter 3 we studied the coarsening process of anti-phase domains in symmetric and asymmetric binary compounds via large scale Monte Carlos simulations. Using the q -state Potts model and microscopically realistic models of atomic order in compounds, we showed that there exists a universal scaling function for a system with a given ground-state degeneracy q . The general form of the scaled real-space pair-correlation functions can be described very well by a linear combination of an exponential function and two Gaussian distributions. The respective Fourier transform of this real-space scaling function results in a very good fit of the scaled reciprocal-space structure factors. Further, integrating this three-dimensional radially symmetric function over two perpendicular dimensions gave us an expression corresponding to the peak profile in powder diffractometry. Finally, we introduced the scaling factor $L(t)$, which relates the APD scale to the inverse of the specific interface area of the APD configuration. This spatial length scale is equivalent to the domain size obtained with the standard linear intercept method in microscopy. With our expression of the peak profile we can describe the size broadened superstructure peaks in diffraction using the same scaling factor $L(t)$. Hence, we obtained in this chapter a model which quantitatively relates the APD scale obtained in microscopy to the ones measured via scattering experiments without any adjustable parameters.

The correlation between structural order and the extent of magnetic order in Ni_2MnZ Heusler alloys was investigated in chapter 4. Here, we demonstrated the applicability of our phenomenological model for the coarsening process in Ni_2MnZ Heusler alloys.

The structural ordering process of the B2-L2₁ transition corresponds to a system with a ground-state degeneracy $q = 2$. We investigated the APD scale of Ni₂MnAl and Ni₂MnAl_{0.5}Ga_{0.5} powder samples for distinct L2₁ ordering states using neutron powder diffraction. With increasing annealing time, we observed an increase in the APD scale for the ternary and quaternary compounds. Small-angle neutron scattering measurements were performed on the powder samples to study the respective magnetic microstructure. We obtained an equivalent length scale for the magnetic order by applying the same phenomenological model. Comparing both length scales showed that the magnetic and structural domains are identical. Finally, we observed in the temperature-dependent SANS profiles a shift of intensity towards higher Q for the measurements above the magnetic transition temperature. This shift indicates an increase in diffusive scattering intensity, which equals to the loss of the magnetic contrast in the samples.

Having provided strong evidence that the structural and magnetic order are strongly correlated, we investigated the magnetic coupling of the magnetic domains across the structural domain boundaries in Ni₂MnZ compounds via magnetic small-angle neutron scattering. In chapter 5, the presented magnetic scattering signal shows an anisotropy in the case of an applied magnetic field, similar to the expected response of a Heisenberg anti-ferromagnet. This behaviour of the scattering intensity is observed in all samples and indicates the spins located in neighbouring APDs to couple anti-ferromagnetically across their APB. Interestingly, we observed with increasing temperature two magnetic transitions in the samples: first from the antiparallel alignment of the domains to a spin polarised case when approaching the respective magnetic transition temperature and at higher temperatures the transition from this spin polarised state to a disordered paramagnetic one above the T_c .

The here presented model gives a qualitative description of the coarsening process of anti-phase domains as well as the development of magnetic order on the mesoscopic length scale. However in this model we used the assumption that there is no magnetic disorder inside the domains, resulting for example from Mn antisites, or magnetocrystalline anisotropy. Instead we considered the spins to be free to align to an external magnetic field only depending on their neighbouring spins and all magnetic domains to be perfectly ordered. Since the microscopic picture of magnetic order is much more complicated than assumed in our model, it would be interesting to test our model and further develop it for the magnetic order.

Appendix A

Considerations of the Instrumental Resolution Function for Time-of-Flight Neutron Powder Diffractometers

The line shape of a spectrum curve measured at a time-of-flight neutron powder diffractometer at a pulsed neutron source is asymmetric due to the moderation process in a spallation source. Here the high-energy neutrons are moderated to epithermal (> 300 meV) and thermal (< 300 meV) energies before being used for diffraction. The resulting neutron pulse structure is shaped further by the choppers of the velocity selectors and has a complex and asymmetric shape, which is usually characterized by a sharp exponential rise and slower exponential decay (Von Dreele, Jorgensen, and Windsor, 1982). This asymmetry makes describing the line shape of a TOF neutron powder diffraction pattern difficult: Von Dreele, Jorgensen, and Windsor (1982) suggested an empirical description, which is a back-to-back paired set of exponentials convoluted with a Gaussian distribution. A more successful approach is given by the convolution of a pseudo-Voigt function and the back-to-back exponentials (Thompson, Cox, and Hastings, 1987) and is implemented in many diffraction analysis programs (Larson and Von Dreele, 1994; Rodríguez-Carvajal, 2001). In this section the convolution of these functions is derived as well as the numeric considerations needed for its evaluation are discussed.

One of the best mathematical descriptions of the instrumental and sample intrinsic profiles measured via powder diffraction is the Voigt profile $V(x; \sigma, \gamma)$ (Young and Wiles, 1982). It is given by a convolution of a Lorentzian distribution $L(x; \gamma)$ and a Gaussian distribution $G(x; \sigma)$. However, due to its relative complexity its

computational use was delayed and many earlier programs used instead a simple approximation, the pseudo-Voigt function $V_p(x; f)$ (David, 1986). Rather than computing the convolution of both distributions this profile is a linear combination of the Gaussian and the Lorentzian distribution, as given in

$$V_p(x; f) = \eta L(x; f) + (1 - \eta)G(x; f) = \eta \frac{f}{\pi(x^2 + f^2)} + (1 - \eta) \frac{1}{f\sqrt{2\pi}} e^{-x^2/(2f^2)}. \quad (\text{A.1})$$

Here, η is the scaling parameter of the Gaussian and the Lorentzian distribution and f is the total full width at half maximum parameter of $V_p(x; f)$. In order to mimic the exact Voigt function the pseudo-Voigt profile is parametrized as proposed by Thompson, Cox, and Hastings (1987): The total FWHM f is given by the Gaussian f_G and Lorentz f_L as:

$$f = [f_G^5 + 2.69269f_G^4f_L + 2.42843f_G^3f_L^2 + 4.47163f_G^2f_L^3 + 0.07842f_Gf_L^4 + f_L^5].$$

The scaling parameter η is a function of the Lorentz and total FWHM and is described by

$$\eta = 1.36603 \frac{f_L}{f} - 0.47719 \left(\frac{f_L}{f} \right)^2 + 0.11116 \left(\frac{f_L}{f} \right)^3.$$

Since further convolutions with additional functional contributions such as the moderator pulse, described by back-to-back exponentials (Von Dreele, Jorgensen, and Windsor, 1982), are needed to describe the time-of-flight neutron powder diffraction data and these convolutions are more simply computed for the pseudo-Voigt profile than the Voigt profile, many programs, such as *General Structure Analysis System* (GSAS; Larson and Von Dreele (1994)) and FULLPROF (Rodríguez-Carvajal, 2001) still use rather the pseudo-Voigt profile than the Voigt profile.

The back-to-back exponentials are given as

$$B(x; a, b) = \frac{ab}{a+b} \left(e^{-ax} \theta(x) + e^{bx} \theta(-x) \right) \quad (\text{A.2})$$

where $\theta(x)$ is the Heaviside step function, a is the decay coefficient and b the rise coefficient.

The convolution of an exponential decay with a Gaussian distribution is

$$\begin{aligned} \left(\left(e^{-ax} \theta(x) \right) \otimes \left(\frac{1}{\sqrt{2\pi}\sigma} e^{-x^2/2\sigma^2} \right) \right) (y) &= \frac{1}{\sqrt{2\pi}\sigma} \int_0^\infty e^{-ax} e^{-(y-x)^2/2\sigma^2} dx \\ &= \frac{1}{\sqrt{\pi}} e^{-a(y-\sigma^2 a/2)} \int_{-(y-\sigma^2 a)/\sqrt{2}\sigma}^\infty e^{-z^2} dz, \end{aligned}$$

where we used the substitution $z = (x - (y - f^2 a)) / \sqrt{2}f$. The integral of $\exp(-z^2)$ can be written as the complementary error function. Since the convolution of an exponential rise function and a Gaussian distribution can be derived analogously, we obtain for the convolution of the back-to-back exponentials with the Gaussian part of the pseudo-Voigt function the following expression:

$$\left(B(x; a, b) \otimes G(x; f) \right) (y) = \frac{ab}{2(a+b)} \left(e^{-a(y-f^2 a/2)} \operatorname{erfc} \left(-\frac{y-f^2 a}{\sqrt{2}f} \right) + e^{b(y+f^2 b/2)} \operatorname{erfc} \left(\frac{y+f^2 b}{\sqrt{2}f} \right) \right)$$

For the convolution of Eq. A.2 and a Lorentzian profile we have to consider first the expression of the Lorentzian distribution as an imaginary function:

$$\frac{1}{1 + (\Gamma x)^2} = \frac{1}{2} \left(\frac{1}{1 + i\Gamma x} + \frac{1}{1 - i\Gamma x} \right) = \operatorname{Re} \left(\frac{1}{1 + i\Gamma x} \right) \quad (\text{A.3})$$

where the last expression holds for real x values. If the exponential decay coefficient is also a real number, one can write the convolution as

$$\begin{aligned} \left(\left(e^{-ax} \theta(x) \right) \otimes \left(\frac{1}{(\Gamma x)^2 + 1} \right) \right) (y) &= \operatorname{Re} \left(\int_0^\infty e^{-ax} \frac{1}{1 + i\Gamma(y-x)} dx \right) \\ &= \operatorname{Re} \left(\frac{i}{\Gamma} e^{-a(y-i/\Gamma)} \int_{-a(y-i\Gamma)}^\infty \frac{e^{-z}}{z} dz \right), \end{aligned}$$

where z substitutes the following expression $z = -ay + ia/\Gamma$. The integral of this equation is known as the exponential integral $E_1(x) = \int_x^\infty \exp(-t)/t dt$, hence we can write the convolution of $B(x; a, b)$ and the Lorentz part of the pseudo-Voigt profile as

$$\begin{aligned} \left(B(x; a, b) \otimes L(x; f) \right) (y) &= \frac{ab}{\pi(a+b)} \operatorname{Re} \left(i e^{-a(y-if)} E_1(-ay + ia f) \right) \\ &\quad + \frac{ab}{\pi(a+b)} \operatorname{Re} \left(i e^{b(y+if)} E_1(by + ib f) \right) \end{aligned}$$

The complete convolution of $B(x; a, b)$ and the pseudo-Voigt function is a function of t , the time of flight of a neutron from its source to the detector. As t can reach large values ($t > 10\,000\ \mu\text{s}$), the numeric representation of $\exp(bt)$ can become problematic. But in the convolution the exponential functions, which can become very large, are combined with functions, which become very small for large t . Hence in order to still give meaningful expression for such values, we have to consider approximations and different expressions for the complementary error function and the exponential integral.

The exponential integral can be expressed by a convergent series as (Abramowitz and Stegun, 1972)

$$E_1(x) = -\gamma - \ln(x) - \sum_{k=1}^{\infty} \frac{(-x)^k}{k k!} \quad (\text{A.4})$$

where γ is the Euler-Mascheroni constant. For large x values, in the limits $t < -6/b$ and $20/b < t$, as well as if the FWHM of the Lorentzian distribution is smaller than the exponential coefficient, the integral is well approximated by the continued fraction expansion (Abramowitz and Stegun, 1972)

$$E_1(x) = \frac{\exp(-x)}{x + \frac{1}{1 + \frac{2}{x + \frac{2}{1 + \frac{3}{x + \frac{3}{\dots}}}}}}. \quad (\text{A.5})$$

Using these expressions we can give a good numeric representation of the respective convolution, as the exponential functions either cancel each other as in Eq. (A.5) or the values of t are small enough to be expressed by $\exp(bt)$.

In case of the complementary error function $\text{erfc}(y)$ we use the following case distinction to approximate it (Press et al., 1992):

$$\text{erfc}(x) \approx \begin{cases} \tau(x) & x \geq 0 \\ 2 - \tau(-x) & x \leq 0 \end{cases} \quad (\text{A.6})$$

where the function $\tau(x)$ is given as

$$\begin{aligned}\tau(x) = u \exp(& -x^2 - 1.26551223 + 1.00002368u + 0.37409196u^2 + 0.09678418u^3 \\ & - 0.18628806u^4 + 0.27886807u^5 - 1.13520398u^6 + 1.48851587u^7 \\ & - 0.82215223u^8 + 0.17087277u^9)\end{aligned}$$

with u being defined as $u = 1/(1 + 0.5|x|)$. Here the exponents of the exponential functions can be added in the problematic case of $x \geq 0$, which resolves the numeric representation problem. For values smaller 0, the exponential function is small and therefore in this case no further approximation is needed.

Via these approximations we are able to give a numeric evaluation of the instrumental resolution function over the whole t -range.

Appendix B

Calibration of the Small-Angle Neutron Scattering Signal

This appendix chapter deals with the correction of the miscalibration of a 2D SANS detector. For both instruments, SANS-1 at FRM II and D33 at ILL, we measured the SANS signal using a ^3He gas multi-tube detector with a monoblock design.

Fig. B.1 shows the 2D scattering intensity of our $\text{Ni}_2\text{MnAl}_{0.5}\text{Ga}_{0.5}$ 10 d annealed sample at room temperature without a magnetic field applied, measured at D33, ILL, Grenoble. At first glance we observe an isotropic signal as we have seen at the instrument SANS-1 for the same sample under similar conditions. A closer examination of the signal reveals that several detector rows are shifted against each other, as indicated by the arrows in Fig. B.1. As these shifts are visible in all measurements independent of the sample, temperature or external magnetic field, they must be due to a no longer valid calibration of the plane detector. As for our data analysis of the 2D signal the ratio of the intensity distribution in the horizontal and vertical direction is of great interest, a precise allocation of the events on the plane detector is crucial.

These shifts are due to the set-up of the detector, which was briefly discussed in Chap. 4.4. To understand why we can correct for them via an ex post calibration, we first discuss the general set-up of such a plane detector in greater detail and compare its signal between both instruments.

Dewhurst et al. (2016) give a detailed description of the experimental set-up of the instrument D33. Its neutron detector is a ^3He gas multi-tube detector with the dimensions of $0.64\text{ m} \times 0.64\text{ m}$. It contains 128 horizontal position sensitive detector tubes with a vertical resolution of 5 mm determined by the tube spacing. In the

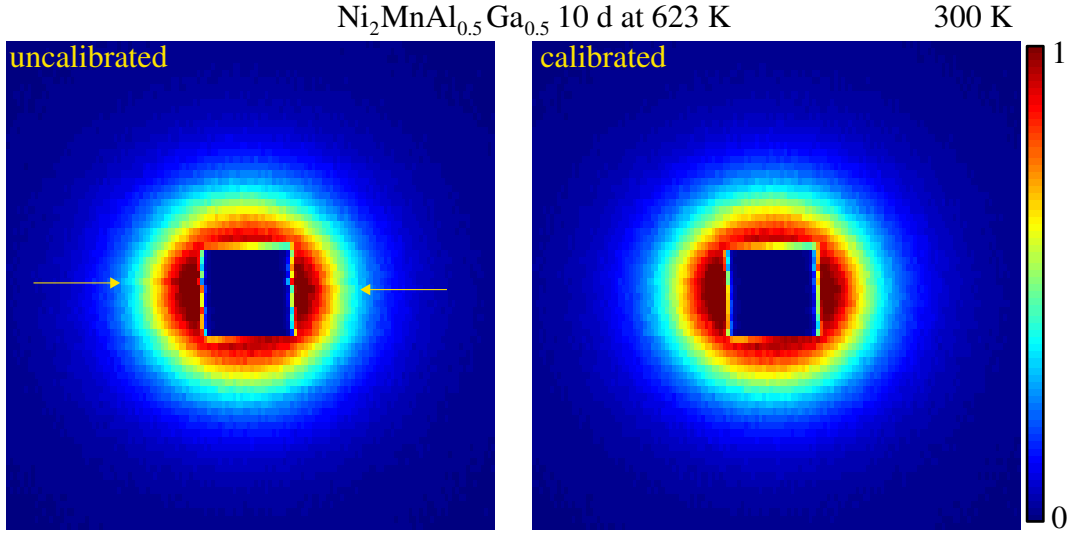


Figure B.1: 2D SANS signal of the sample $\text{Ni}_2\text{MnAl}_{0.5}\text{Ga}_{0.5}$ 10 d annealed at room temperature without an external magnetic field. On the left the uncalibrated signal is depicted, while on the right the signal after calibration is shown.

horizontal direction the event positioning is provided by a charge division of the neutron event on the resistive detection wire. The position along the wire is digitized into 256 channels, corresponding to a pixel size of 2.5 mm. The intrinsic resolution along the wire length is estimated to be approximately 5 mm, matching that of the tube spacing in the vertical direction. Due to the construction of the 2D detector, each row corresponds to a single detector, which is evaluated independently to their neighbouring rows and must be calibrated separately.

In case of D33 the detector is calibrated by mounting a Cadmium mask with precisely machined slits on its front window. Using a so-called flat scattering sample, e.g. water or acrylic glas, ensures a uniform illumination over the entire detector surface. With the neutrons being only detected at the positions of the slits, the raw pixel positions are determined via centre-of-mass calculations. Dewhurst et al. (2016) observed the position sensitivity of the tubes to be highly linear with different offsets and gradients for each tube.

The observed shifts in the 2D signal appear to be mainly in the horizontal direction as shown in Fig. B.2, where the intensity distribution around the beam stop in vertical and horizontal direction is depicted. The beam stop covers an area of (13×27) pixels, at the position $[59, 72] \times [114, 141]$ pixels. Since the shifts are stable for all measurements independent of the sample and sample environment, we determine the parameters of our ex post calibration from the sum over all profiles, which gives us the best counting statistics for the correction of these shifts.

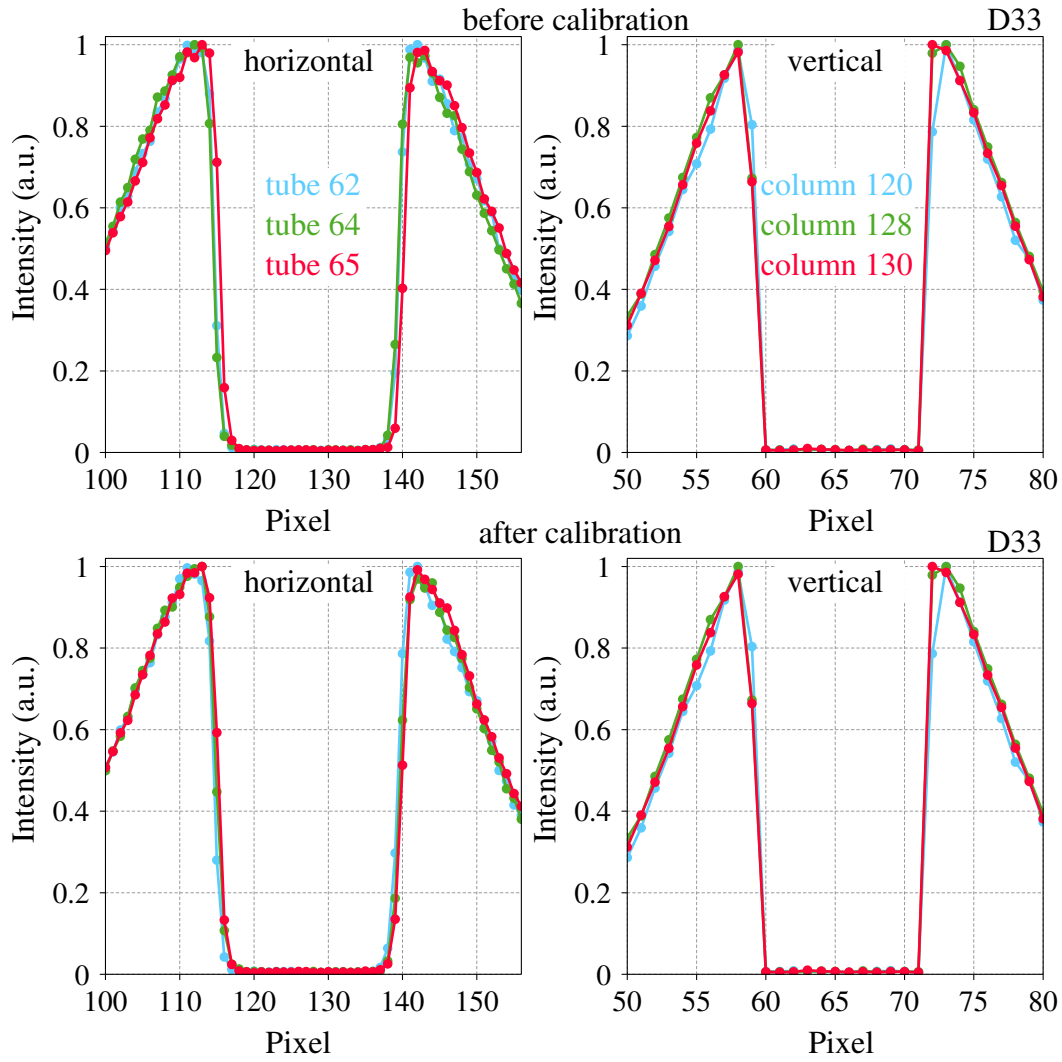


Figure B.2: Upper panels: Intensity distribution at D33 around the beam stop before the calibration. Here are shown the intensity distribution of detector rows on the right and detector columns on the left of the $\text{Ni}_2\text{MnAl}_{0.5}\text{Ga}_{0.5}$ 10 d spectra, measured at room temperature without an external magnetic field. In the lower panel the intensity distribution is shown after the calibration. The line connecting the data points is a guide for the lines.

The idea behind the ex post calibration method is, that the intensity distribution measured in a certain detector row x should not differ severely from the ones recorded in its neighbouring rows $(x - 1)$ and $(x + 1)$. This assumption is valid for our powder samples as the scattering intensity is expected to decay continuously away from the beam center. Further we observe the shifts between the detector rows to be uncorrelated to each other. Hence, we correct for them by comparing the interpolated intensity distribution to the mean of the interpolated intensities of the neighbouring rows. As the plot of raw pixel position versus physical position shows the position sensitivity of the tubes to be highly linear but with different offsets and gradients for each tube (Dewhurst et al., 2016), we describe the positioning along each detector tube by the following linear variation of $y \in [1, 256]$

$$\tilde{y} = s(x)y + dy(x), \quad (\text{B.1})$$

where $s(x)$ is the scaling factor, which corresponds to the respective resistivity of the detection wire x , and $dy(x)$ is the shift, being the physical offset of the detector row x relative to its neighbours. Finally we consider the relative efficiency $E(x)$ of the detector row x , which fluctuates around unity due to the varying ^3He pressure in the tubes (Dewhurst et al., 2016).

We determine all three parameters for each detector row via least-squares fitting of the row intensity distribution by minimizing the relative deviation between the interpolated data and the interpolated average of its neighbours. In order to prevent the beam stop effecting our parameters we mask the pixels parallel to the beam stop in all rows. As we observe a strong correlation between the efficiency and the scale $s(x)$ as well as know from (Dewhurst et al., 2016) that the efficiency should be stable around unity, we use a regularization matrix which leaves the efficiency of the detector tubes deviating less than 10^{-5} from 1. The respective parameter values of the linear variation for each row are depicted in Fig. B.3. We fit these three parameters iteratively.

With the obtained parameters we calibrate our signal by reassigning counts from one pixel to another along the detection wire. We assume that the locations of the events in a pixel are uniformly distributed and assign each event a position inside their respective pixel. To redistribute the events according to our calibration parameters we apply the inverse of the linear variation of Eq. (B.1) to each event location and assign the counts to the pixels which their new location corresponds to. Counts that

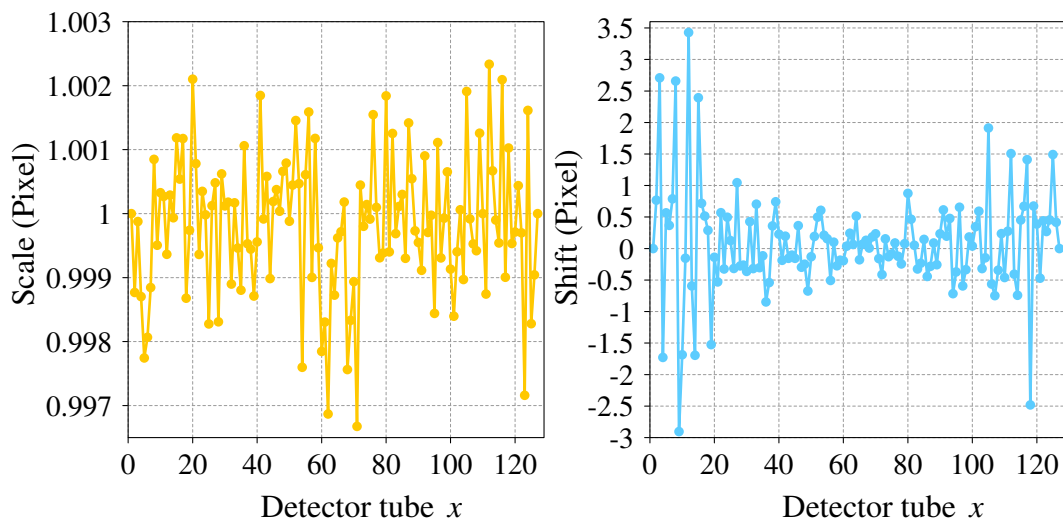


Figure B.3: The ex post calibration parameters scale $s(x)$ and shift $dy(x)$ of the detector tubes x .

would be assigned to a pixel below 1 or beyond 256 are neglected, which is the case for less than 1% of the total number of counts per tube.

We applied this calibration to all SANS profiles measured at D33.

Bibliography

- Abramowitz, M. and Stegun, I. (1972). *Handbook of mathematical functions*. Washington, D.C.: U.S. Dept. of Commerce, National Bureau of Standards, pp. 229–229. ISBN: 978-0883075890.
- Acet, M., Duman, E., Wassermann, E., Mañosa, L., and Planes, A. (2002). „Coexisting ferro- and antiferromagnetism in Ni₂MnAl Heusler alloys“. *J. Appl. Phys.* 92.7, pp. 3867–3871. DOI: 10.1063/1.1504498.
- Allen, S. and Cahn, J. (1975). „Coherent and incoherent equilibria in iron-rich iron-aluminum alloys“. *Acta Metall.* 23.9, pp. 1017–1026. ISSN: 0001-6160. DOI: 10.1016/0001-6160(75)90106-6.
- (1979). „A microscopic theory for antiphase boundary motion and its application to antiphase domain coarsening“. *Acta Metall.* 27.6, pp. 1085 –1095. DOI: 10.1016/0001-6160(79)90196-2.
- Bazavov, A., Berg, B., and Dubey, S. (2008). „Phase transition properties of 3D Potts models“. *Nucl. Phys. B* 802.3, pp. 421–434. ISSN: 0550-3213. DOI: 10.1016/j.nuclphysb.2008.04.020.
- Bhatti, K., El-Khatib, S., Srivastava, V., James, R., and Leighton, C. (Apr. 2012). „Small-angle neutron scattering study of magnetic ordering and inhomogeneity across the martensitic phase transformation in Ni_{50-x}Co_xMn₄₀Sn₁₀ alloys“. *Phys. Rev. B* 85 (13), p. 134450. DOI: 10.1103/PhysRevB.85.134450.
- Blundell, R. and Bray, A. (June 1994). „Phase-ordering dynamics of the O(n) model: Exact predictions and numerical results“. *Phys. Rev. E* 49 (6), pp. 4925–4937. DOI: 10.1103/PhysRevE.49.4925.
- Bortz, A., Kalos, M., Lebowitz, J., and Zendejas, M. (July 1974). „Time evolution of a quenched binary alloy: Computer simulation of a two-dimensional model system“. *Phys. Rev. B* 10 (2), pp. 535–541. DOI: 10.1103/PhysRevB.10.535.
- Bradley, A., Jay, A., and Bragg, W. (1932). „The formation of superlattices in alloys of iron and aluminium“. *Proc. R. Soc. Lond. A* 136.829, pp. 210–232. DOI: 10.1098/rspa.1932.0075.

- Bradley, A., Rodgers, J., and Bragg, W. (1934). „The crystal structure of the heusler alloys“. *Proc. R. Soc. Lond. A* 144.852, pp. 340–359. DOI: 10.1098/rspa.1934.0053.
- Bradley, A., Taylor, A., and Bragg, W. (1938). „An X-ray study of iron-nickel-aluminium ternary equilibrium diagram“. *Proc. R. Soc. Lond. A* 166.926, pp. 353–375. DOI: 10.1098/rspa.1938.0098.
- Bray, A. (2002). „Theory of phase-ordering kinetics“. *Adv. Phys.* 51.2, pp. 481–587. DOI: 10.1080/00018730110117433.
- Brenker, F., Müller, W., and Brey, G. (Aug. 2003). „Variation of antiphase domain size in omphacite: A tool to determine the temperature–time history of eclogites revisited“. *Am. Mineral.* 88.8-9, pp. 1300–1311. ISSN: 0003-004X. DOI: 10.2138/am-2003-8-912.
- Buras, B. and Gerward, L. (May 1975). „Relations between integrated intensities in crystal diffraction methods for X-rays and neutrons“. *Acta Crystallographica Section A* 31.3, pp. 372–374. DOI: 10.1107/S0567739475000782.
- Chiu, P. (2017). „Correlation of magnetic domains and L_{21} anti-phase domains in NiMn-based Heusler alloys“. MA thesis. Technical University of Munich.
- Creutz, M. (Apr. 1980). „Monte Carlo study of quantized SU(2) gauge theory“. *Phys. Rev. D* 21 (8), pp. 2308–2315. DOI: 10.1103/PhysRevD.21.2308.
- David, W. (Feb. 1986). „Powder diffraction peak shapes. Parameterization of the pseudo-Voigt as a Voigt function“. *J. Appl. Crystallogr.* 19 (1), pp. 63–64. DOI: 10.1107/S0021889886089999.
- Dewhurst, C., Grillo, I., Honecker, D., Bonnaud, M., Jacques, M., Amrouni, C., Perillo-Marcone, A., Manzin, G., and Cubitt, R. (Feb. 2016). „The small-angle neutron scattering instrument D33 at the Institut Laue–Langevin“. *J. Appl. Crystallogr.* 49.1, pp. 1–14. DOI: 10.1107/S1600576715021792.
- Efron, B. and Tibshirani, R. (1994). *An Introduction to the Bootstrap*. Chapman & Hall/CRC Monographs on Statistics & Applied Probability. Boca Raton, FL: CRC Press. ISBN: 978-0-412-04231-7. DOI: 10.1201/9780429246593.
- El-Khatib, S., Bhatti, K., Srivastava, V., James, R., and Leighton, C. (Oct. 2019). „Nanoscale magnetic phase competition throughout the $\text{Ni}_{50-x}\text{Co}_x\text{Mn}_{40}\text{Sn}_{10}$ phase diagram: Insights from small-angle neutron scattering“. *Phys. Rev. Materials* 3 (10), p. 104413. DOI: 10.1103/PhysRevMaterials.3.104413.
- Feigin, L. and Svergun, D. (1987). *Structure Analysis by Small-Angle X-Ray and Neutron Scattering*. Springer, Boston, MA, pp. 26–127. ISBN: 978-0-306-42629-2. DOI: 10.1007/978-1-4757-6624-0.

- Ferrenberg, A., Xu, J., and Landau, D. (Apr. 2018). „Pushing the limits of Monte Carlo simulations for the three-dimensional Ising model“. *Phys. Rev. E* 97 (4), p. 043301. DOI: 10.1103/PhysRevE.97.043301.
- Fratzl, P. and Penrose, O. (Aug. 1994). „Kinetics of spinodal decomposition in the Ising model with vacancy diffusion“. *Phys. Rev. B* 50 (5), pp. 3477–3480. DOI: 10.1103/PhysRevB.50.3477.
- Frigo, M. and Johnson, S. (2005). „The Design and Implementation of FFTW3“. *Proc. IEEE* 93.2. Special issue on “Program Generation, Optimization, and Platform Adaptation”, pp. 216–231. DOI: 10.1109/JPROC.2004.840301.
- Frontera, C., Vives, E., Castán, T., and Planes, A. (Jan. 1997). „Monte Carlo study of the growth of L1₂-ordered domains in fcc A₃B binary alloys“. *Phys. Rev. B* 55 (1), pp. 212–225. DOI: 10.1103/PhysRevB.55.212.
- Frontera, C., Vives, E., and Planes, A. (1994). „Antiphase domain growth in BCC metallic alloys via vacancies“. *Z. Phys. B* 96, pp. 79–86. DOI: 10.1007/BF01313017.
- Furrer, A., Mesot, J., and Strässle, T. (2009). *Neutron Scattering in Condensed Matter Physics*. World Scientific Publishing Co. Pte. Ltd., pp. 123–127. ISBN: 978-981-02-4831-4.
- Gilles, R., Hofmann, M., Gao, Y., Johnson, F., Iorio, L., Larsen, M., Liang, F., Hölzel, M., and Barbier, B. (2010). „Probing the relationship of long-range order in nanodomain FeCo alloys with ternary additions using neutron diffraction“. *Met. Mat. Trans. A* 41.5, pp. 1144–1150. DOI: 10.1007/s11661-009-9933-y.
- Gilles, R., Ostermann, A., and Petry, W. (Apr. 2007). „Monte Carlo simulations of the new small-angle neutron scattering instrument SANS-1 at the Heinz Maier-Leibnitz Forschungsneutronenquelle“. *J. Appl. Crystallogr.* 40.s1, s428–s432. DOI: 10.1107/S0021889807006310.
- Glatter, O. and Kratky, O. (1982). *Small Angle X-ray Scattering*. Academic Press Inc., pp. 26–29. ISBN: 9780122862809.
- Graf, T., Felser, C., and Parkin, S. (2011). „Simple rules for the understanding of Heusler compounds“. *Prog. Solid State Chem.* 39.1, pp. 1–50. ISSN: 0079-6786. DOI: 10.1016/j.progsolidstchem.2011.02.001.
- Grest, G., Anderson, M., and Srolovitz, D. (Sept. 1988). „Domain-growth kinetics for the Q-state Potts model in two and three dimensions“. *Phys. Rev. B* 38 (7), pp. 4752–4760. DOI: 10.1103/PhysRevB.38.4752.
- Groot, R. de, Mueller, F., Engen, P. van, and Buschow, K. (June 1983). „New Class of Materials: Half-Metallic Ferromagnets“. *Phys. Rev. Lett.* 50 (25), pp. 2024–2027. DOI: 10.1103/PhysRevLett.50.2024.

- Heusler, F. (1903). „Über magnetische Manganlegierungen“. *Verhandlungen der Deutschen Physikalischen Gesellschaft* 12, p. 219.
- Hu, F., Shen, B., and Sun, J. (2000). „Magnetic entropy change in Ni_{51.5}Mn_{22.7}Ga_{25.8} alloy“. *Appl. Phys. Lett.* 76.23, pp. 3460–3462. DOI: 10.1063/1.126677.
- Huq, A., Hodges, J., Gourdon, O., and Heroux, L. (2015a). „Powgen: A third-generation highresolution high-throughput powder diffraction instrument at the Spallation Neutron Source“. *European Powder Diffraction Conference; August 2010, Darmstadt, Germany*. Oldenbourg Wissenschaftsverlag, pp. 127–136. DOI: doi : 10 . 1524 / 9783486991321-024.
- Huq, A., Hodges, J., O.Gourdon, and Heroux, L. (2015b). „Powgen: A third-generation highresolution high-throughput powder diffraction instrument at the Spallation Neutron Source“. *European Powder Diffraction Conference; August 2010, Darmstadt, Germany*. Oldenbourg Wissenschaftsverlag, pp. 127–136. DOI: 10 . 1524 / 9783486991321-024.
- Iosevich, A. and Liflyand, Elijah (2014). „The Fourier Transform of a Radial Function“. *Decay of the Fourier Transform*. Basel: Springer, pp. 93–126. ISBN: 978-3-0348-0625-1. DOI: 10.1007/978-3-0348-0625-1_5.
- Ishikawa, H., Umetsu, R., Kobayashi, K., Fujita, A., Kainuma, R., and Ishida, K. (2008). „Atomic ordering and magnetic properties in Ni₂MnGa_xAl_{1-x} Heusler alloys“. *Acta Mater.* 56.17, pp. 4789–4797. ISSN: 1359-6454. DOI: 10.1016/j.actamat.2008.05.034.
- Jesche, A., Caroca-Canales, N., Rosner, H., Borrmann, H., Ormeci, A., Kasinathan, D., Klauss, H., Luetkens, H., Khasanov, R., Amato, A., Hoser, A., Kaneko, K., Krellner, C., and Geibel, C. (Nov. 2008). „Strong coupling between magnetic and structural order parameters in SrFe₂As₂“. *Phys. Rev. B* 78 (18), p. 180504. DOI: 10.1103/PhysRevB.78.180504.
- Kawasaki, K. (May 1966). „Diffusion Constants near the Critical Point for Time-Dependent Ising Models. I“. *Phys. Rev.* 145 (1), pp. 224–230. DOI: 10.1103/PhysRev.145.224.
- Kawasaki, K., Yalabik, M., and Gunton, J. (Jan. 1978). „Growth of fluctuations in quenched time-dependent Ginzburg-Landau model systems“. 17 (1), pp. 455–470. DOI: 10.1103/PhysRevA.17.455.
- Kessler, M., Dieterich, W., and Majhofer, A. (2003a). „Monte Carlo study of ordering and domain growth in a class of fcc-alloy models“. *Physica A* 330.1, pp. 25–30. ISSN: 0378-4371. DOI: 10.1016/j.physa.2003.08.021.
- (Apr. 2003b). „Ordering kinetics in an fcc A₃B binary alloy model: Monte Carlo studies“. *Phys. Rev. B* 67 (13), p. 134201. DOI: 10.1103/PhysRevB.67.134201.

- Kostorz, G. (Oct. 1991). „Small-angle scattering studies of phase separation and defects in inorganic materials“. *J. Appl. Crystallogr.* 24.5, pp. 444–456. DOI: 10.1107/S0021889891002467.
- Kreissl, M., Neumann, K., Stephens, T., and Ziebeck, K. (May 2003). „The influence of atomic order on the magnetic and structural properties of the ferromagnetic shape memory compound Ni₂MnGa“. *J. Phys.: Condens. Matter* 15.22, pp. 3831–3839. DOI: 10.1088/0953-8984/15/22/317.
- Kwiatkowski, A., Wasik, D., Kamińska, M., Bożek, R., Szczytko, J., Twardowski, A., Borysiuk, J., Sadowski, J., and Gosk, J. (2007). „Structure and magnetism of MnAs nanocrystals embedded in GaAs as a function of post-growth annealing temperature“. *J. Appl. Phys.* 101.11, p. 113912. DOI: 10.1063/1.2739215.
- Langford, J. and Wilson, A. (1978). „Scherrer after sixty years: A survey and some new results in the determination of crystallite size“. *J. Appl. Crystallogr.* 11.2, pp. 102–113. DOI: 10.1107/S0021889878012844.
- Larson, A. and Von Dreele, R. (1994). „Gsas“. *Report LAUR*, pp. 86–748.
- Leoni, M. and Scardi, P. (Aug. 2004). „Nanocrystalline domain size distributions from powder diffraction data“. *J. Appl. Crystallogr.* 37.4, pp. 629–634. DOI: 10.1107/S0021889804013366.
- Ležaić, M., Mavropoulos, P., Bihlmayer, G., and Blügel, S. (Oct. 2013). „Exchange interactions and local-moment fluctuation corrections in ferromagnets at finite temperatures based on noncollinear density-functional calculations“. *Phys. Rev. B* 88 (13), p. 134403. DOI: 10.1103/PhysRevB.88.134403.
- Liu, F. and Mazenko, G. (Nov. 1991). „Nonequilibrium autocorrelations in phase-ordering dynamics“. *Phys. Rev. B* 44 (17), pp. 9185–9191. DOI: 10.1103/PhysRevB.44.9185.
- Mazenko, G. (Sept. 1990). „Theory of unstable growth“. *Phys. Rev. B* 42 (7), pp. 4487–4505. DOI: 10.1103/PhysRevB.42.4487.
- Metropolis, N., Rosenbluth, A., Rosenbluth, M., Teller, A., and Teller, E. (1953). „Equation of State Calculations by Fast Computing Machines“. *J. Chem. Phys.* 21.6, pp. 1087–1092. DOI: 10.1063/1.1699114.
- Miura, Y., Nagao, K., and Shirai, M. (Apr. 2004). „Atomic disorder effects on half-metallicity of the full-Heusler alloys Co₂(Cr_{1-x}Fe_x)Al : A first-principles study“. *Phys. Rev. B* 69 (14), p. 144413. DOI: 10.1103/PhysRevB.69.144413.
- Morris, D., Besag, F., and Smallman, R. (1974). „Ordering and disordering in Cu₃Au“. *Phil. Mag. A* 29.1, pp. 43–57. DOI: 10.1080/14786437408213552.

- Morris, D., Brown, G., Piller, R., and Smallman, R. (1976). „Ordering and domain growth in Ni₃Fe“. *Acta Metall.* 24.1, pp. 21–28. ISSN: 0001-6160. DOI: 10.1016/0001-6160(76)90142-5.
- Mühlbauer, S., Heinemann, A., Wilhelm, A., Karge, L., Ostermann, A., Defendi, I., Schreyer, A., Petry, W., and Gilles, R. (June 2016). „Magnetic small-angle neutron scattering“. *Nuclear Instruments and Methods in Physics Research A* 832, p. 297. DOI: 10.17815/jlsrf-1-32.
- Mühlbauer, S., Honecker, D., Périgo, É., Bergner, F., Disch, S., Heinemann, A., Erokhin, S., Berkov, D., Leighton, C., Eskildsen, M., and Michels, A. (Mar. 2019). „Magnetic small-angle neutron scattering“. *Rev. Mod. Phys.* 91 (1), p. 015004. DOI: 10.1103/RevModPhys.91.015004.
- Murakami, Y., Shindo, D., Kobayashi, K., Oikawa, K., Kainuma, R., and Ishida, K. (2006). „TEM studies of crystallographic and magnetic microstructures in Ni-based ferromagnetic shape memory alloys“. *Mat. Sci. Eng. A* 438-440, pp. 1050–1053. DOI: 10.1016/j.msea.2006.05.016.
- Murakami, Y., Yano, T., Umetsu, R.Y., Kainuma, R., and Shindo, D. (2011). „Suppression of ferromagnetism within antiphase boundaries in Ni₅₀Mn₂₅Al_{12.5}Ga_{12.5} alloy“. *Scripta Mater.* 65.10, pp. 895–898. ISSN: 1359-6462. DOI: 10.1016/j.scriptamat.2011.08.003.
- Murray, S., Marioni, M., Allen, S., O’Handley, R., and Lograsso, T. (2000). „6% magnetic-field-induced strain by twin-boundary motion in ferromagnetic Ni–Mn–Ga“. *Appl. Phys. Lett.* 77.6, pp. 886–888. DOI: 10.1063/1.1306635.
- Nagler, S., Shannon, R., Harkless, C., Singh, M., and Nicklow, R. (Aug. 1988). „Time-Resolved X-Ray Scattering Study of Ordering and Coarsening in Cu₃Au“. *Phys. Rev. Lett.* 61 (6), pp. 718–721. DOI: 10.1103/PhysRevLett.61.718.
- Neel, Louis (Nov. 1952). „Antiferromagnetism and Ferrimagnetism“. *Proceedings of the Physical Society. Section A* 65.11, pp. 869–885. DOI: 10.1088/0370-1298/65/11/301.
- Neibecker, P. (2017). „Atomic order and its influence on functional properties of NiMn-based Heusler systems“. PhD thesis. Technical University of Munich.
- Neibecker, P., Gruner, M., Xu, X., Kainuma, R., Petry, W., Pentcheva, R., and Leitner, M. (Oct. 2017). „Ordering tendencies and electronic properties in quaternary Heusler derivatives“. *Phys. Rev. B* 96 (16), p. 165131. DOI: 10.1103/PhysRevB.96.165131.
- Neibecker, P., Leitner, M., Benka, G., and Petry, W. (2014). „Increasing the achievable state of order in Ni-based Heusler alloys via quenched-in vacancies“. *Appl. Phys. Lett.* 105.26, p. 261904. DOI: 10.1063/1.4905223.

- Ohta, T., Jasnow, D., and Kawasaki, K. (Oct. 1982). „Universal Scaling in the Motion of Random Interfaces“. *Phys. Rev. Lett.* 49 (17), pp. 1223–1226. DOI: 10.1103/PhysRevLett.49.1223.
- O'Neill, M. (Sept. 2014). *PCG: A Family of Simple Fast Space-Efficient Statistically Good Algorithms for Random Number Generation*. Tech. rep. HMC-CS-2014-0905. Claremont, CA: Harvey Mudd College.
- Overholser, R., Wuttig, M., and Neumann, D. (1999). „Chemical ordering in Ni-Mn-Ga Heusler alloys“. *Scripta Mater.* 40.10, pp. 1095–1102. ISSN: 1359-6462. DOI: 10.1016/S1359-6462(99)00080-9.
- Patterson, A. (Nov. 1939). „The Scherrer Formula for X-Ray Particle Size Determination“. *Phys. Rev.* 56 (10), pp. 978–982. DOI: 10.1103/PhysRev.56.978.
- Pawley, G. (June 1981). „Unit-cell refinement from powder diffraction scans“. *J. Appl. Crystallogr.* 14.2, pp. 357–361. DOI: 10.1107/S0021889881009618.
- Pecharsky, V. and Gschneidner Jr., K. (June 1997). „Giant Magnetocaloric Effect in $\text{Gd}_5(\text{Si}_2\text{Ge}_2)$ “. *Phys. Rev. Lett.* 78 (23), pp. 4494–4497. DOI: 10.1103/PhysRevLett.78.4494.
- Phani, M., Lebowitz, J., Kalos, M., and Penrose, O. (Aug. 1980). „Kinetics of an Order-Disorder Transition“. *Phys. Rev. Lett.* 45 (5), pp. 366–369. DOI: 10.1103/PhysRevLett.45.366.
- Pierre, J., Skolozdra, R., Tobola, J., Kaprzyk, S., Hordequin, C., Kouacou, M., Karla, I., Currat, R., and Lelièvre-Berna, E. (1997). „Properties on request in semi-Heusler phases“. *J. Alloys Comp.* 262-263. Proceedings of the Twelfth International Conference on Solid Compounds of Transition Elements, pp. 101–107. ISSN: 0925-8388. DOI: 10.1016/S0925-8388(97)00337-X.
- Planes, A., Mañosa, L., and Acet, M. (May 2009). „Magnetocaloric effect and its relation to shape-memory properties in ferromagnetic Heusler alloys“. *J. Phys.: Condens. Matter* 21.23, p. 233201. DOI: 10.1088/0953-8984/21/23/233201.
- Pochet, P., Tominez, E., Chaffron, L., and Martin, G. (Aug. 1995). „Order-disorder transformation in Fe-Al under ball milling“. *Phys. Rev. B* 52 (6), pp. 4006–4016. DOI: 10.1103/PhysRevB.52.4006.
- Pollock, T. and Tin, S. (2006). „Nickel-Based Superalloys for Advanced Turbine Engines: Chemistry, Microstructure and Properties“. *J. Propul. Power* 22.2, pp. 361–374. DOI: 10.2514/1.18239.
- Potts, R. (1952). „Some generalized order-disorder transformations“. *Proc. Camb. Philos. Soc.* 48.1, pp. 106–109. DOI: 10.1017/S0305004100027419.
- Press, W., Teukolsky, S., Vetterling, W., and Flannery, B. (1992). *Numerical Recipes in Fortran 77*. Cambridge University Press, pp. 214–214. ISBN: 978-0521430647.

- Rodríguez-Carvajal, J. (2001). „FullProf“. *CEA/Saclay, France*.
- Rogers, J., Flower, H., and Rawlings, R. (1975). „The Electron Metallography of Antiphase Domain Growth in FeCo–2%V“. *Metall. Sci.* 9.1, pp. 32–35. DOI: 10.1179/030634575790445062.
- Rutenberg, A. and Bray, A. (June 1995). „Energy-scaling approach to phase-ordering growth laws“. *Phys. Rev. E* 51 (6), pp. 5499–5514. DOI: 10.1103/PhysRevE.51.5499.
- Sakai, M. and Mikkola, D. (1971). „The growth of antiphase domains in Cu₃Au as studied by transmission electron microscopy“. *Metall. Trans.* 2.6, pp. 1635–1641.
- Sakurada, S. and Shutoh, N. (2005). „Effect of Ti substitution on the thermoelectric properties of (Zr,Hf)NiSn half-Heusler compounds“. *Appl. Phys. Lett.* 86.8, p. 082105. DOI: 10.1063/1.1868063.
- Sauthoff, G. (1973). „Growth kinetics and size distribution of ordered domains in Cu₃Au“. *Acta Metall.* 21.3, pp. 273–279. ISSN: 0001-6160. DOI: 10.1016/0001-6160(73)90014-X.
- Scardi, P. and Leoni, M. (Mar. 2002). „Whole powder pattern modelling“. *Acta Cryst.* 58.2, pp. 190–200. DOI: 10.1107/S0108767301021298.
- (2005). „Diffraction whole-pattern modelling study of anti-phase domains in Cu₃Au“. *Acta Mater.* 53.19, pp. 5229–5239. ISSN: 1359-6454. DOI: 10.1016/j.actamat.2005.08.002.
- Scherrer, P. (1918). „Bestimmung der Größe und der inneren Struktur von Kolloidteilchen mittels Röntgenstrahlen“. *Nachr. Ges. Wiss. Göttingen* 1918, pp. 98–100.
- Simak, S., Ruban, A., Abrikosov, I., Skriver, H., and Johansson, B. (July 1998). „Ordered Phases in Cu₂NiZn: A First-Principles Monte Carlo Study“. *Phys. Rev. Lett.* 81 (1), pp. 188–191. DOI: 10.1103/PhysRevLett.81.188.
- Simon, E., Vida, J., Khmelevskiy, S., and Szunyogh, L. (Aug. 2015). „Magnetism of ordered and disordered Ni₂MnAl full Heusler compounds“. *Phys. Rev. B* 92 (5), p. 054438. DOI: 10.1103/PhysRevB.92.054438.
- Smith, C. and Guttman, L. (1953). „Measurement of Internal Boundaries in Three-Dimensional Structures By Random Sectioning“. *J. Met.* 5 (1), pp. 81–87. DOI: 10.1007/BF03397456.
- Sołtys, J. (1981). „X-ray diffraction research of the order–disorder transitions in the ternary heusler alloys B₂MnAl (B = Cu, Ni, Co, Pd, Pt)“. *phys. stat. sol. (a)* 66.2, pp. 485–491. DOI: 10.1002/pssa.2210660210.
- Squires, G. (2012). *Introduction to the Theory of Thermal Neutron Scattering*. Cambridge University Press, pp. 25–152. ISBN: 978-1-107-64406-9.
- Stoloff, N. (1984). „Ordered alloys – physical metallurgy and structural applications“. *Int. Metals Rev.* 29.1, pp. 123–135. DOI: 10.1179/imtr.1984.29.1.123.

- Stoloff, N. and Davies, R. (1968). „The mechanical properties of ordered alloys“. *Prog. Mater. Sci.* 13, pp. 1–84. ISSN: 0079-6425. DOI: 10.1016/0079-6425(68)90018-2.
- Suzuki, A., Takeyama, M., and Matsuo, T. (2002). „Transmission electron microscopy on the phase equilibria among β , α and α_2 phases in Ti-Al binary system“. *Intermetallics* 10.9, pp. 915–924. ISSN: 0966-9795. DOI: 10.1016/S0966-9795(02)00113-9.
- Thompson, P., Cox, D., and Hastings, J. (Apr. 1987). „Rietveld refinement of Debye-Scherrer synchrotron X-ray data from Al₂O₃“. *J. Appl. Crystallogr.* 20 (2), pp. 79–83. DOI: 10.1107/S0021889887087090.
- Toyoki, H. (Feb. 1992). „Structure factors of vector-order-parameter systems containing random topological defects“. *Phys. Rev. B* 45 (5), pp. 1965–1970. DOI: 10.1103/PhysRevB.45.1965.
- Ullakko, K., Huang, J., Kantner, C., O’Handley, R., and Kokorin, V. (1996). „Large magnetic-field-induced strains in Ni₂MnGa single crystals“. *Appl. Phys. Lett.* 69.13, pp. 1966–1968. DOI: 10.1063/1.117637.
- Umetsu, R., Ishikawa, H., Kobayashi, K., Fujita, A., Ishida, K., and Kainuma, R. (2011). „Effects of the antiferromagnetic anti-phase domain boundary on the magnetization processes in Ni₂Mn(Ga_{0.5}Al_{0.5}) Heusler alloy“. *Scripta Mater.* 65.1, pp. 41–44. ISSN: 1359-6462. DOI: 10.1016/j.scriptamat.2011.03.014.
- Umetsu, R., Xu, X., and Kainuma, R. (2016). „NiMn-based metamagnetic shape memory alloys“. *Scripta Materialia* 116, pp. 1–6. ISSN: 1359-6462. DOI: 10.1016/j.scriptamat.2016.01.006.
- Venkateswaran, S., Nuhfer, N., and De Graef, M. (2007). „Anti-phase boundaries and magnetic domain structures in Ni₂MnGa-type Heusler alloys“. *Acta Mater.* 55.8, pp. 2621–2636. ISSN: 1359-6454. DOI: 10.1016/j.actamat.2006.12.003.
- Vetter, R. and Baal, C. van (1990). „A simple model describing correlation functions and domain structure of the simulated ordering of AB alloys“. *Phil. Mag. B* 61.2, pp. 189–199. DOI: 10.1080/13642819008205520.
- Vidoz, A., Lazarević, D., and Cahn, R. (1963). „Strain-ageing of ordering alloys, with special reference to the nickel-iron system“. *Acta Metall.* 11.1, pp. 17–33. ISSN: 0001-6160. DOI: 10.1016/0001-6160(63)90121-4.
- Vives, E. and Planes, A. (Feb. 1992). „Kinetics of a vacancy-driven order-disorder transition in a two-dimensional binary alloy“. *Phys. Rev. Lett.* 68 (6), pp. 812–815. DOI: 10.1103/PhysRevLett.68.812.
- Von Dreele, R., Jorgensen, J., and Windsor, C. (Dec. 1982). „Rietveld refinement with spallation neutron powder diffraction data“. *J. Appl. Crystallogr.* 15.6, pp. 581–589. DOI: 10.1107/S0021889882012722.

- Wagner, W., Wiedenmann, A., Petry, W., Geibel, A., and Gleiter, H. (1991). „Magnetic microstructure of nanostructured Fe, studied by small angle neutron scattering“. *Journal of Materials Research* 6.11, 2305–2311. DOI: 10.1557/JMR.1991.2305.
- Webster, P., Ziebeck, K., Town, S., and Peak, M. (1984). „Magnetic order and phase transformation in Ni₂MnGa“. *Phil. Mag. B* 49.3, pp. 295–310. DOI: 10.1080/13642817408246515.
- Weinkamer, R., Fratzl, P., Sepiol, B., and Vogl, G. (Aug. 1998). „Monte Carlo simulation of diffusion in a B2-ordered model alloy“. *Phys. Rev. B* 58 (6), pp. 3082–3088. DOI: 10.1103/PhysRevB.58.3082.
- Wernick, J., Hull, G., Geballe, T., Bernardini, J., and Waszczak, J. (1983). „Superconductivity in ternary Heusler intermetallic compounds“. *Materials Letters* 2.2, pp. 90–92. ISSN: 0167-577X. DOI: 10.1016/0167-577X(83)90043-5.
- Willis, B. and Carlile, C. (2009). *Experimental Neutron Scattering*. Oxford University Press, pp. 15–34. ISBN: 978-0-19-851970-6.
- Wu, F. (Jan. 1982). „The Potts model“. *Rev. Mod. Phys.* 54 (1), pp. 235–268. DOI: 10.1103/RevModPhys.54.235.
- Yano, T., Murakami, Y., Kainuma, R., and Shindo, D. (2007). „Interaction between Magnetic Domain Walls and Antiphase Boundaries in Ni₂Mn(Al,Ga) Studied by Electron Holography and Lorentz Microscopy“. *Mat. Trans. JIM* 48.10, pp. 2636–2641. DOI: 10.2320/matertrans.MD200783.
- Young, R. and Wiles, D. (Aug. 1982). „Profile Shape Functions in Rietveld Refinements“. *J. Appl. Crystallogr.* 15 (4), pp. 430–438. DOI: 10.1107/S002188988201231X.
- Ziebeck, K. and Webster, P. (Sept. 1975). „Helical magnetic order in Ni₂MnAl“. *J. Phys. F: Met. Phys.* 5.9, pp. 1756–1766. DOI: 10.1088/0305-4608/5/9/015.
- Zweck, U. and Leitner, M. (Sept. 2021). „Antiphase domain growth: Correlation functions and structure factors in the scaling regime“. *Phys. Rev. B* 104 (9), p. 094101. DOI: 10.1103/PhysRevB.104.094101.
- Zweck, U., Neibecker, P., Mühlbauer, S., Zhang, Q., Chiu, P., and Leitner, M. (n.d.). *Magnetization reversal induced by anti-phase domain boundaries in Ni₂MnZ Heusler compounds*.